STEREO Observations of Solar Wind Transients in the Inner Heliosphere

Thomas Michael Conlon

Radio and Space Plasma Physics Group
Department of Physics and Astronomy
University of Leicester

A thesis submitted to the University of Leicester
for the degree of Doctor of Philosophy

December 2014

Abstract: STEREO observations of solar wind transients in the inner heliosphere, Thomas Michael Conlon

This thesis investigates the implications of relaxing assumptions inherent in techniques that analyse solar wind transients observed by NASA's Solar TErrestrial RElations Observatory (STEREO). In the first research chapter, I relaxed the assumption that the STEREO spacecraft are stationary while observing a transient. For much of the parameter space investigated, this effect was minimal, however in some cases it resulted in differences in derived radial speeds of hundreds of km s^{-1}, leading to large errors. Using real data examples, the difference this effect makes was shown.

The second research chapter applies the previous analysis to Corotating Interactions Region (CIR) observations. CIR events were identified in STEREO HI J-maps, analysed, and their predicted arrival times calculated at each of the STEREO and Advanced Composition Explorer (ACE) spacecraft. A superposed epoch analysis was conducted using the predicted arrival times as the zero epoch time. It was found that when the fixed STEREO spacecraft assumption was relaxed, the CIR related transients that I observed had their estimated propagation speed increase such that they were propagating at (or close to) the slow solar wind speed, a physically realistic change. Changes in the structure of a stream interface over 1–2 days were seen, calling into question some of the underlying assumptions, which assume constant propagation characteristics over longer time-scales.

Finally, I consider acceleration of solar wind transients close to the Sun. I use the analysis from previous chapters to perform fits to transient trajectories close to the Sun and infers the size of the acceleration region required to achieve convincing fits at low elongation values. It was found that the behaviour of the transients is consistent with an acceleration region within which the transient accelerates and then adopts a constant propagation speed. The acceleration region does not appear to occur at a fixed radial distance, but rather is different for each event analysed.

Acknowledgements

Thanks should go to many people, without whom the last few years would have been a much poorer experience. Some of these people are mentioned below.

Firstly, I would like to thank STFC for making the funding available to allow me to conduct this PhD.

Thanks are due to all my friends and colleagues at the University of Leicester, in the Physics department and the games society. You have all made the last seven years some of the most memorable of my life and never once made me regret joining the University of Leicester as a bright-eyed undergraduate. In particular I would like to thank John for many things, not least of all lunchtime amusement. Colin and Rob I would also like to make a special mention of for their assistance with formatting this thesis.

My PhD experience would not have been the same without visits to schools or amateur astronomy societies trying to enthuse others about, so thanks should go to Tracey and especially Gabby for making that possible.

Thanks to Jackie and especially Steve for their advice and guidance. For their unprecedented capacity for re-reading my writing and beating it into shape. For not taking things too seriously, and providing a bottomless pit of sarcasm. You were both invaluable.

A massive thank you is due to my family. To my parents for their constant support and for regularly listening to me, even if I wasn't always as cheery as I might have been and to Rebecca, for keeping me sane, especially when things weren't going as well, and for never losing faith in me. Thanks don't even come close, but they shall have to suffice.

Thanks should also go to those people, friends, family, colleagues, whom I have not specifically mentioned here, but who have shaped my life and its progress up to this point regardless. You have all helped make me who I am.

Contents

List of Tables

List of Figures

Abbreviations

3-D 3-Dimension(s)

ACE Advanced Composition Explorer

C1/2/3 The three coronagraphs of the LASCO experiment

CCD Charge-Coupled Device

CIR/SIR Corotating Interaction Region/Stream Interface Region

CME Coronal Mass Ejection

COR1/2 Inner/outer CORonagraphs on board STEREO

EUVI Extreme UntraViolet Imager on board STEREO

FP(F) Fixed-Phi (Fitting)

HEE Heliocentric Earth Ecliptic (coordinate system)

HI-1/2/A/B Inner/outer Heliospheric Imager on board each of the STEREO-A/B spacecraft

HM(F) Harmonic Mean (Fitting)

IMF Interplanetary Magnetic Field

IMPACT In-situ Measurements of PArticles and CME Transients

JAXA Japan Aerospace eXploration Agency

LASCO Large Angle and Spectrometric Coronagraph Experiment

LISM Local InterStellar Medium

MAG MAGnetometer on board STEREO

MHD MagnetoHydroDynamic(s)

NASA National Aeronautics and Space Administration

PLASTIC PLAsma and SupraThermal Ion Composition

PP Point-P

PPARC Particle Physics and Astronomy Research Council, predecessor to STFC

SC SpaceCraft

SDO Solar Dynamics Observatory

SECCHI Sun-Earth ConneCtion and Heliospheric Investigation STEREO instrument package

SOHO SOlar and Heliospheric Observatory

SSE(F) Self-Similar Expansion (Fitting)

STEREO-A/B Solar TErrestrial RElations Observatory -Ahead/Behind

STFC Science and Technology Facilities Council

SWAVES STEREO/WAVES STEREO instrument package

SWEPAM Solar Wind Electron, Proton and Alpha Monitor on board STEREO

TS Thomson Surface

Chapter 1

Introduction

1.1 Motivation

Throughout history, human civilisation has been fascinated by the Sun and its effects here on Earth. This fascination has worked its way into mythology, with many cultures having a god dedicated to the Sun or a myth to explain the apparent movement of the Sun across the sky that induced day and night. Even at this early stage, there was an acknowledgment that the Sun exerted a great influence on the climate and conditions on our planet, with people often praying to a god of the Sun for a bountiful harvest and short winter. Even phenomena that were not known at the time to be influenced by the behaviour of the Sun were attached great religious importance, with for example, the aurorae deriving their name from the Roman goddess of the dawn. It was not for many years however that our understanding of the Sun and the many processes it controls started to move away from images drawn from people's imaginings and towards a more sophisticated picture based upon observations.

There have been recorded observations of sunspots for hundreds of years (Russell, 1995), however it was not until 1859 that the first links between solar activity and geomagnetic conditions were made, with the occurrence of a powerful geomagnetic storm. Multiple solar flares were observed on the solar disk, followed by a much

brighter flare which was observed across the globe. Eighteen hours later ground based magnetometers observed the largest geomagnetic storm on record. The event, known as the 'Carrington event' after one of the astronomers who observed its associated solar flares, stimulated further study which developed into the modern field of solar-terrestrial relations (Russell, 1995).

For most of the history of solar terrestrial relations studies, the instruments available have been situated on the Earth and taken measurements in-situ, such as magnetometers. In 1930, Bernard Lyot invented the coronagraph, allowing remote observations of the Sun's corona to be made throughout the year. Previously the corona could only be seen when the Sun was naturally occulted during an eclipse. These instruments were still ground based however, and so viewing limitations due to the Earth's atmosphere were an issue.

With the dawn of the space age during the mid twentieth century came the opportunity to mount instruments on spacecraft, therefore giving the opportunity for coronagraphs to view the Sun from beyond the Earth's atmosphere. The first attempt to put a coronagraph beyond the Earth's atmosphere came in 1965 with the launch of the Solar Observatory 2 mission (Koomen *et al.*, 1975). This spacecraft was part of a NASA attempt to view a complete solar cycle in both ultraviolet and x-rays. The mission was successful in observing multiple features, such as coronal holes, sunspots and solar flares. In the intervening time, many spacecraft have been launched with coronagraphs to make observations of the solar corona and our understanding of the solar corona has steadily improved; however it is only in more recent times that we have been able to make observations of the Sun far from the Sun-Earth line.

In 2006 NASA launched the STEREO mission (Kaiser *et al.*, 2007). STEREO comprises two spacecraft in Earth-like heliocentric orbits, but with each separating from the Sun-Earth line over time, allowing observations of coronal material as it moves towards the Earth from vantage points off the Sun-Earth line. The period of time during which the STEREO mission was launched coincided with a pronounced solar minimum, allowing observations of the quiet-time solar wind and solar activity

(Williams *et al.*, 2011). The main aim of this thesis is to take advantage of the timing of the STEREO mission to investigate quiet time solar wind features.

In the remainder of this chapter, we consider the theoretical context of this thesis, concentrating on electromagnetic theory and space plasma physics.

1.2 Electromagnetic theory and plasma physics

The solar wind is a magnetised, tenuous, ionised gas known as a plasma. To this end we shall discuss electromagnetic theory and plasma physics in this section.

1.2.1 Maxwell's equations, single particle motion and the first and second adiabatic invariants

As the cornerstone of modern electromagnetic theory, we shall discuss Maxwell's equations here. In Eq. 1.1 – 1.4 can be seen Maxwell's equations (Gauss' law, no monopoles, Faraday's law and the Ampère-Maxwell relation respectively),

$$\nabla.\mathbf{E} = \frac{\rho_q}{\varepsilon_0} \tag{1.1}$$

$$\nabla.\mathbf{B} = 0 \tag{1.2}$$

$$\nabla \times \mathbf{E} = -\frac{\partial \mathbf{B}}{\partial t} \tag{1.3}$$

$$\nabla \times \mathbf{B} = \mu_0 \mathbf{j} + \mu_0 \varepsilon_0 \frac{\partial \mathbf{E}}{\partial t} \tag{1.4}$$

where $\mathbf{E}$ is the electric field, ρ_{q} is the charge density, ε_0 is the permittivity of free space, $\mathbf{B}$ is the magnetic field, μ_0 is the permeability of free space and $\mathbf{j}$ is the current density. For solar wind applications, $\partial\mathbf{E}/\partial t \cong 0$ so we can ignore the displacement current in Eq. 1.4, reducing it to Ampére's Law.

If one introduces a moving charged particle into a region with an existing electric

or magnetic field, then these fields will exert a force on the particle. The net force upon the particle will be the resultant force exerted by the electric and magnetic fields. In this instance, with all other forces assumed negligible, one can write Newton's second law for the particle as,

$$m\frac{d\mathbf{v}}{dt} = q(\mathbf{E} + \mathbf{v} \times \mathbf{B}) \tag{1.5}$$

with m the mass of the particle, $\mathbf{v}$ its velocity, q its charge, $\mathbf{E}$ the electric field and $\mathbf{B}$ the magnetic field. By letting either $\mathbf{E}$ or $\mathbf{B}$ be 0, we can investigate the individual effects of each of the electric and magnetic fields on the charged particle.

Letting $\mathbf{E} = 0$, we can see that the force exerted on the particle (now due only to the Lorentz force) is applied in a direction perpendicular to its direction of motion, and has no effect if the particle's motion is parallel to the magnetic field direction. Thus, the force can change the direction of the particle, but not its total energy. Considering a particle with $v_\perp \neq 0$, the motion due to the Lorentz force will make the particle's motion follow a circle. The frequency of this motion is called the cyclotron frequency (ω_c) and is given by

$$\omega_\mathrm{c} = \frac{|q|B}{m} \tag{1.6}$$

with m the mass of the particle. The radius of the orbit of the particle is called the Larmour radius (r_L) and is given by

$$r_\mathrm{L} = \frac{mv_\perp}{|q|B}. \tag{1.7}$$

As the particle's speed is conserved, $v^2 = v_\perp^2 + v_\parallel^2$. This leads to Eq. 1.8,

$$\frac{v_\perp^2}{B} = const = \frac{v_{\perp 0}^2}{B_0} \tag{1.8}$$

where B is the magnitude of the magnetic field strength and $v_{\perp 0}^2$ and B_0 are measured at some specified initial point. The quantity $v_\perp^2/B$ is known as the first adiabatic

invariant (Chen, 2006). For a converging magnetic field, the Lorentz force will point in a direction perpendicular to **B** and so for a particle moving towards a region of increasing field strength, there will be a component of this force in the opposite direction of $v_{\parallel}$ and so, there will be a point at which $v_{\parallel} = 0$ and the particle is 'mirrored'. If we denote the magnetic field strength at this 'mirror' point as B_{m}, then

$$v^2 = v_{\perp 0}^2 \left(\frac{B_{\mathrm{m}}}{B_0} \right) \tag{1.9}$$

or

$$B_{\mathrm{m}} = B_0 \left(\frac{v}{v_{\perp 0}} \right)^2 . \tag{1.10}$$

Another way of representing particle motion is to define the pitch angle α such that

$$\tan \alpha = \frac{v_{\perp}}{v_{\parallel}}. \tag{1.11}$$

Using this notation, the first adiabatic invariant then becomes

$$\frac{\sin^2 \alpha}{B} = const, \tag{1.12}$$

so, the particle will mirror when $\alpha_{\mathrm{m}} = 90°$. If we consider a particle trapped between two magnetic mirrors (sometimes called a magnetic bottle), there will be a periodic motion between these two, with this motion having a bounce frequency. There will then be a "longitudinal invariant" (J) associated with this motion, denoted by

$$J = \int_a^b v_{\parallel} ds = const \tag{1.13}$$

with ds the element of length along the field line and a and b correspond to the two mirror points of the particle. This is the second adiabatic invariant and if J is to be conserved, then this means that a particle will experience changes in magnetic field strength only on time scales that are long compared with the bounce period.

If one now takes the electric and magnetic fields to be non-zero and perpendicular to one another, then a charged particle will experience a drifting motion perpendicular to each of the fields, with the velocity of this drift given by

$$\mathbf{V} = \frac{\mathbf{E} \times \mathbf{B}}{B^2} + V_{\parallel}\hat{\mathbf{B}}. \tag{1.14}$$

If one has $\nabla B \perp \mathbf{B}$, then this will lead to the particle drifting, with the drifting velocity given by

$$\mathbf{V}_{\nabla \mathbf{B}} = \pm\frac{1}{2}v_{\perp}r_{\mathrm{L}}\frac{\mathbf{B} \times \nabla B}{B^2}, \tag{1.15}$$

with the $\pm$ accounting for the particle's charge, so an electron and an ion will drift in opposite directions.

Considering now a curved magnetic field, this curvature shall also make the particle drift. The velocity of this drift is described by

$$\mathbf{V}_{\mathrm{R}} = \frac{mv_{\parallel}^2}{qB^2}\frac{\mathbf{R}_{\mathrm{c}} \times \mathbf{B}}{R_{\mathrm{c}}^2} \tag{1.16}$$

where R_{c} is the radius of curvature of the field lines.

We now consider magnetic and electric fields $\mathbf{B}(\mathbf{r}, t)$ and $\mathbf{E}(\mathbf{r}, t)$ which vary slowly in time and space (relative to gyroradii and gyroperiods) and that are perpendicular to each other. Assuming also that Faraday's law holds and that the first adiabatic invariant is preserved, then we find an effect known as Alfvén's theorem. This says that if a charged particle has its gyromotion centred on a particular field line, then it will remain on that field line for all time. This is also known as the 'frozen in flux' approximation and is discussed in more detail in secton 1.2.3. If the particle moves, then the field line is carried along with it and if the magnetic field changes, then the particle also moves. This is also known as the 'frozen in flux' approximation as the charged particles are frozen in to the magnetic field and vice versa. Whether we consider the particles frozen-in to the plasma or the plasma frozen-in to the particles

depends on the ratio of energies between the two. If the magnetic field energy is larger it moves the particles and if the energy of the particles dominates, it will drag the magnetic field with it. How well the frozen-in approximation holds depends on the ratio of the magnitudes of the $\mathbf{E} \times \mathbf{B}$ drift (Eq. 1.14) to the magnitudes of the gradient (Eq. 1.15) and curvature (Eq. 1.16) drifts. These last two are energy dependent and for higher energies, the frozen-in condition will no longer hold. For very strong gradients, then the frozen-in condition may not also hold at lower energies. For more discussion regarding the implications of the frozen-in flux condition, see section 1.2.3.

1.2.2 Definition of a plasma

One definition of a plasma is a "quasineutral gas of charged and neutral particles which exhibits collective behaviour" (Chen, 2006). In this section we shall define what we mean by "quasineutral" and "collective behaviour", consider the second adiabatic invariant and give a more rigourous definition of a plasma.

If we introduce charged probes into a collection of charged particles, then the charged particles will move in response to the electric field imposed by the probes, i.e. positive ions will move toward the cathode and electrons toward the anode. The particles will move in such a way as to cancel out the electric field imposed by the probes. There shall therefore be a spherical volume around each electrode beyond which the effect of the electric field it is imposing is not felt. The radius of this sphere is called the Debye length and it is defined as

$$\lambda_{\mathrm{D}} = \left(\frac{\epsilon_0 k_{\mathrm{B}} T_{\mathrm{e}}}{n e^2} \right)^{\frac{1}{2}} \tag{1.17}$$

where ϵ_0 the permittivity of free space, k_{B} the Boltzman constant, T_{e} the electron temperature, n the number density of charged particles and e the fundamental unit of charge. The number of particles in this volume (N_{D}) is then

$$N_{\mathrm{D}} = \frac{4\pi\lambda_{\mathrm{D}}^3 n_{\mathrm{e}}}{3}. \tag{1.18}$$

In order to have quasi-neutrality, we need the collection of particles to be neutral when taken as a whole, i.e. no net charge. This is preserved over larger spatial scales in a plasma but not smaller, so in order to have charge neutrality, one requires that

$$\lambda_{\mathrm{D}} \ll L \tag{1.19}$$

where L is the spatial scale of the plasma. In order to maintain "collective behaviour", we require that

$$N_{\mathrm{D}} \gg 1. \tag{1.20}$$

In addition to these two conditions, we also need to have few collisions between particles and so to this end we require that

$$\omega\tau > 1 \tag{1.21}$$

where ω is the frequency of typical plasma oscillations, and τ is the typical time between collisions. These three conditions provide a more rigourous definition of a space plasma.

1.2.3 A plasma as a fluid

We can describe a plasma as a fluid, providing that we use its bulk parameters, such as density, bulk velocity and pressure. For simplicity, we assume a two species plasma, containing electrons and singly charged positive ions. If we have a volume $d\tau$ containing N_{e} electrons and N_{i} ions then the plasma is quasineutral if $N_{\mathrm{e}} = N_{\mathrm{i}}$. We denote the velocities of the j^{th} element of each species as $\mathbf{v}_{\mathrm{ej}}$ and $\mathbf{v}_{\mathrm{ij}}$. It is then possible to write the mass densities of the individual species as

$$\rho_{\mathrm{e}} = \frac{m_{\mathrm{e}} N_{\mathrm{e}}}{d\tau} \tag{1.22}$$

and

$$\rho_{\mathrm{i}} = \frac{m_{\mathrm{i}} N_{\mathrm{i}}}{d\tau} \tag{1.23}$$

and hence the overall mass density as

$$\rho = \rho_{\mathrm{e}} + \rho_{\mathrm{i}} = \frac{m_{\mathrm{e}} N_{\mathrm{e}} + m_{\mathrm{i}} N_{\mathrm{i}}}{d\tau}. \tag{1.24}$$

The bulk electron and ion velocities can then be written as

$$\mathbf{V}_{\mathrm{e}} = \frac{1}{N_{\mathrm{e}}} \sum_{j=1}^{N_{\mathrm{e}}} \mathbf{v}_{\mathrm{ej}} \tag{1.25}$$

and

$$\mathbf{V}_{\mathrm{i}} = \frac{1}{N_{\mathrm{i}}} \sum_{j=1}^{N_{\mathrm{i}}} \mathbf{v}_{\mathrm{ij}}. \tag{1.26}$$

If we are concerned with the bulk quantities, then we wish to consider the motion of the centre of mass, whose position will be denoted by $\mathbf{R}$. In order to calculate this, we need the position vectors of each of the individual particles, $\mathbf{r}_{\mathrm{ej}}$ for electrons and $\mathbf{r}_{\mathrm{ij}}$ for ions. The centre of mass is then

$$\mathbf{R} = \frac{\sum_{j=1}^{N_{\mathrm{e}}} m_{\mathrm{e}} \mathbf{r}_{\mathrm{ej}} + \sum_{j=1}^{N_{\mathrm{e}}} m_{\mathrm{i}} \mathbf{r}_{\mathrm{ij}}}{\sum_{j=1}^{N_{\mathrm{e}}} m_{\mathrm{e}} + \sum_{j=1}^{N_{\mathrm{e}}} m_{\mathrm{i}}}, \tag{1.27}$$

where the denominator is the total mass of the plasma element, and we could replace it with $\rho d\tau$. The velocity of the centre of mass can then be found by differentiating Eq. 1.27 with respect to time as shown in Eq. 1.28

$$\rho d\tau \mathbf{V} = m_{\mathrm{e}} \sum_{j=1}^{N_{\mathrm{e}}} \mathbf{v}_{\mathrm{ej}} + m_{\mathrm{i}} \sum_{j=1}^{N_{\mathrm{i}}} \mathbf{v}_{\mathrm{ij}}. \tag{1.28}$$

From here it is possible to show that

$$\rho d\tau \mathbf{V} = m_{\mathrm{e}} N_{\mathrm{e}} \mathbf{V}_{\mathrm{e}} + m_{\mathrm{i}} N_{\mathrm{i}} \mathbf{V}_{\mathrm{i}}. \tag{1.29}$$

Incorporating Eq. 1.25 and 1.26 we can establish that

$$\rho \mathbf{V} = \rho_{\mathrm{i}} \mathbf{V}_{\mathrm{i}} + \rho_{\mathrm{e}} \mathbf{V}_{\mathrm{e}}. \tag{1.30}$$

The plasma temperature and kinetic pressure are also of interest. If we take the average velocity of the particle (as in Eq. 1.25 and 1.26) and add in a random perturbation $\mathbf{u}_{\mathrm{ej}}$ and $\mathbf{u}_{\mathrm{ij}}$, then by definition, the average of these random perturbations must be 0, but the square of these values will be non-zero, so $\mathbf{v}_{\mathrm{ij}}$ is the velocity of a particular ion, $\mathbf{V}_{\mathrm{i}}$ is the ion bulk motion and the difference between these two, the motion of the ion relative to the bulk motion, is $\mathbf{u}_{ij}$. These random perturbations about the mean represent the thermal energy of ions and electrons, which it is possible to represent as ion and electron temperatures. As with an ideal gas, the average kinetic energy of the particles is $\frac{3}{2} k_{\mathrm{B}} T$. This is written out in full for both electrons and ions in Eq. 1.31 and 1.32. It is possible to write out the partial pressures as in Eq. 1.33 and 1.34 and of course the total pressure is then $P = P_{\mathrm{e}} + P_{\mathrm{i}}$.

$$\frac{3}{2} k_{\mathrm{B}} T_{\mathrm{e}} = \frac{1}{N_{\mathrm{e}}} \sum_{j=1}^{N_{\mathrm{e}}} \frac{1}{2} m_{\mathrm{e}} \mathbf{u}_{\mathrm{ej}}^2 \tag{1.31}$$

$$\frac{3}{2} k_{\mathrm{B}} T_{\mathrm{i}} = \frac{1}{N_{\mathrm{i}}} \sum_{j=1}^{N_{\mathrm{i}}} \frac{1}{2} m_{\mathrm{i}} \mathbf{u}_{\mathrm{ij}}^2 \tag{1.32}$$

$$P_{\mathrm{e}} = n_{\mathrm{e}} k_{\mathrm{B}} T_{\mathrm{e}} \tag{1.33}$$

$$P_{\mathrm{i}} = n_{\mathrm{i}} k_{\mathrm{B}} T_{\mathrm{i}} \tag{1.34}$$

Looking at a moving parcel of fluid, there are a number of continuity equations

of relevance. If we assume that no mass is added to or taken away from our initial fluid parcel, then we have to conserve mass. The total mass continuity equation is shown in Eq. 1.35 below. In tandem with this, we of course have conservation of momentum. This is given by Eq. 1.36. In this expression, the RHS represents the force per unit volume and the LHS the density times the acceleration. More specifically, $\mathbf{V}$ is the bulk speed of the plasma and τ is the volume of the plasma.

$$\frac{\partial \rho}{\partial t} + \nabla.(\rho \mathbf{V}) = 0 \tag{1.35}$$

$$\rho \frac{d\mathbf{V}}{dt} = \frac{1}{d\tau} \sum_j \mathbf{F}_\mathrm{j} \tag{1.36}$$

The forces acting on the particle ($\mathbf{F}_\mathrm{j}$) are a combination of internal and external forces, however the internal forces will cancel leading to only the external forces requiring consideration. It is possible to then write out the full equation of motion for a parcel of plasma, as can be seen in Eq. 1.37, where $\rho\mathbf{g}$ is the force due to gravity, ∇P is due to pressure and $\rho_\mathrm{q}\mathbf{E} + \mathbf{j} \times \mathbf{B}$ is due to electromagnetic forces.

$$\rho \frac{d\mathbf{V}}{dt} = \rho\mathbf{g} - \nabla P + \rho_\mathrm{q}\mathbf{E} + \mathbf{j} \times \mathbf{B} \tag{1.37}$$

It is possible to simplify Eq. 1.37 if it can be shown that one or more of the terms are negligible when compared with the others. By way of example, it can be shown that in non-relativistic situations, the electric force is negligible when compared with the magnetic force.

Neglecting the displacement current (applicable to low frequency situations), the Ampére-Maxwell relation reduces to Ampére's law (Eq. 1.38).

$$\mathbf{j} = \frac{1}{\mu_0} \nabla \times \mathbf{B} \tag{1.38}$$

Crossing both sides with $\mathbf{B}$, one arrives at Eq. 1.39.

$$\mathbf{j} \times \mathbf{B} = \frac{1}{\mu_0}(\mathbf{B}.\nabla)\mathbf{B} - \nabla\left(\frac{B^2}{2\mu_0}\right) \tag{1.39}$$

The similarity between the second term of Eq. 1.39 and the $-\nabla P$ term of Eq. 1.37 suggests that the magnetic field exerts an effective pressure given by Eq. 1.40. This pressure might counterbalance the gas pressure or ram pressure in specific situations.

$$P_{\mathrm{mag}} = \frac{B^2}{2\mu_0} \tag{1.40}$$

The magnetic field exerts a tension force $(\mathbf{B}.\nabla)\mathbf{B}/\mu_0$. Using this along with the previous discussion, allows Eq. 1.37 to be re-written, as seen in Eq. 1.41.

$$\rho\frac{d\mathbf{V}}{dt} = \rho\mathbf{g} - \nabla\left(P + \frac{B^2}{2\mu_0}\right) + \frac{1}{\mu_0}(\mathbf{B}.\nabla)\mathbf{B} \tag{1.41}$$

The energy equation describes the conservation of energy and is generally extremely complicated. For simplification, we can replace it with assumptions concerning the temperature of the gas. A couple of examples include an isothermal gas where T is a constant and pressure is proportional to n or ρ and an adiabatic gas, which means that $P\rho^{-\gamma}$ is a constant.

We can combine this fluid picture of a plasma with Maxwell's equations into a single set of equations referred to as magnetohydronamics (MHD). From here it is possible to establish the induction equation, Eq. 1.42

$$\frac{\partial\mathbf{B}}{\partial t} = \nabla \times (\mathbf{V} \times \mathbf{B}) + \eta\nabla^2\mathbf{B} \tag{1.42}$$

where $\eta = 1/(\mu_0\sigma)$ is the magnetic diffusivity and σ is the electrical conductivity. Taking the ratio of the two terms on the right hand side of Eq. 1.42 leads one to the magnetic Reynold's number,

$$R_{\mathrm{m}} = \mu_0\sigma V L, \tag{1.43}$$

with L once again the length scale of the plasma. Over large length scales, R_{m} is large (> 1) and the frozen-in approximation holds true. On small enough length scales, such that R_{m} is small (< 1) then the frozen-in condition breaks down. This occurs at the thin boundaries between different plasma populations. In these regions there are very thin current sheets and over these small scales, *magnetic reconnection* takes place and Alfvén's theorem ceases to apply. This process involves the reconfiguration of the magnetic fields so that the previously separate and distinct plasma populations become connected and different separate populations are formed. This process is responsible for allowing solar wind plasma into the Earth's magnetosphere for example.

1.3 The Sun

We shall consider the Sun in this section, both its interior and the outer layers, which form the solar atmosphere and directly influence conditions in the solar wind. The Sun itself is a typical middle-aged main sequence star, currently about 4.5 billion years old.

1.3.1 Structure

Fig. 1.1, taken from Priest (1995), shows the structure of the Sun. It shows the approximate size of each region, with the distance of the boundary layers from the centre of the Sun shown as a fraction of a solar radius (1 $\mathrm{R}_{\odot}$ is 1 solar radius) and the temperature at that boundary layer in Kelvin. For the atmosphere, the distance of each layer from the solar surface is given in megametres, along with their corresponding temperatures and densities.

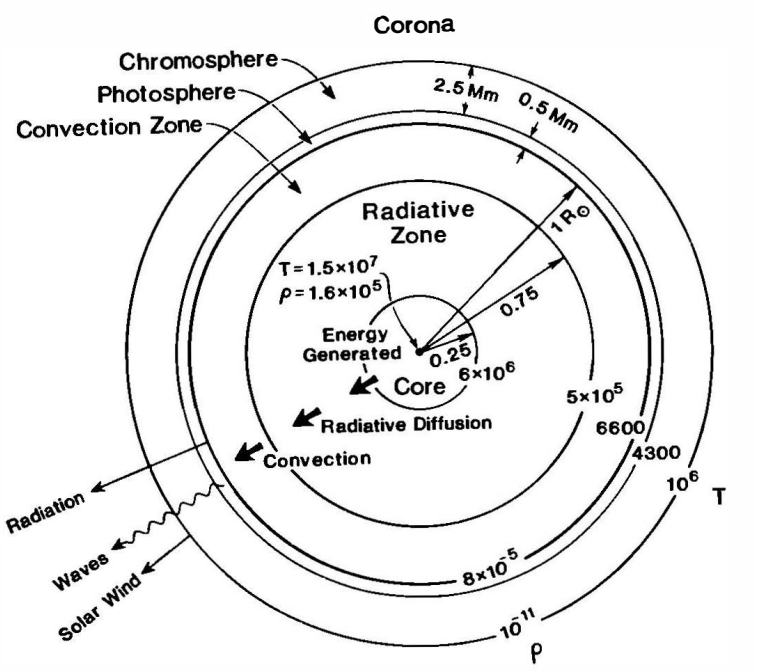

Figure 1.1: The structure of the Sun, showing both its internal structure and that of the atmosphere. The heights of the atmospheric layers above the solar surface are shown in megametres, the radial distances of the internal layers from the centre of the Sun are shows in fractions of a solar radius along with corresponding temperatures (K).

1.3.1.1 Internal structure

At the centre of the Sun lies the core, where most of the nuclear fusion that fuels the star takes place. The majority of this fusion involves the conversion of hydrogen to helium via the proton-proton (p-p) chain. This process generates ≈ 98.8 % of the Sun's energy. Heavier elements also undergo fusion and the CNO cycle, involving the fusion of carbon, nitrogen and oxygen, generates the remaining 1.2 % of the solar energy budget. In both of these cycles, helium is the end product and ≈ 26 MeV of energy is generated per particle of helium.

Energy is radiated out from the core in the form of gamma rays. After the gamma rays leave the core, they are quickly scattered or absorbed and re-emitted, often as x-rays. The re-radiated radiation can be sent in any direction, including back to the core of the Sun and as a result, this layer of the Sun has a high optical thickness and energy takes millions of years to radiate through this region, called the radiative zone, though there is a net motion of energy out from the core of the Sun to the surface. As the radiation progresses further from the core, the temperature of the

material (T) decreases and as a result, the wavelength (λ) of the radiation increases. In the radiative zone, as a parcel of material rises it cools quickly, fast reaching the temperature of the surrounding material. Convection is thus suppressed and hence radiation is the primary mechanism of energy transport. The radiative zone extends out to about 0.7 $R_{\odot}$ (Lang, 2001).

Beyond the radiative zone, the primary method of energy transport is convection. Solar material further from the core has lower density and temperature, meaning that hotter material will rise through this region of the Sun, known as the convection zone. The cause of this density and temperature profile is the pressure balance closer to the solar surface (between thermal energy and gravity), which cannot support heavier particles. This creates a larger temperature gradient across the convective zone, leading to convection dominating. Energy transport is much faster in this region than the radiative zone. It is convective motion of material close to the surface that causes much of the structure observed on the solar surface.

1.3.2 Photosphere

At the top of the convective zone lies the photosphere. This is the layer of the Sun that is visible and is what we normally think of as the solar surface. If one assumes the photosphere is in thermal equilibrium, then it has a black body temperature of about 5800 K. As seen from the Earth, without any further magnification the photosphere appears as a uniform coloured disk, however if one looks closer, structure and substructure can be seen.

Across the photosphere can be seen 'granules'. These are features approximately 1 Mm across and show the convection of the underlying convective zone (see Fig. 1.2). These granules appear to consist of hotter, brighter material that rises in the centre of the region, cools and falls back down at the edges, thus demonstrating the underlying convection. On a larger scale, it is also possible to observe a larger convection pattern known as supergranulation. These features have size scales of about 10 - 30 Mm and are also generally accepted to be caused by convection (Lang,

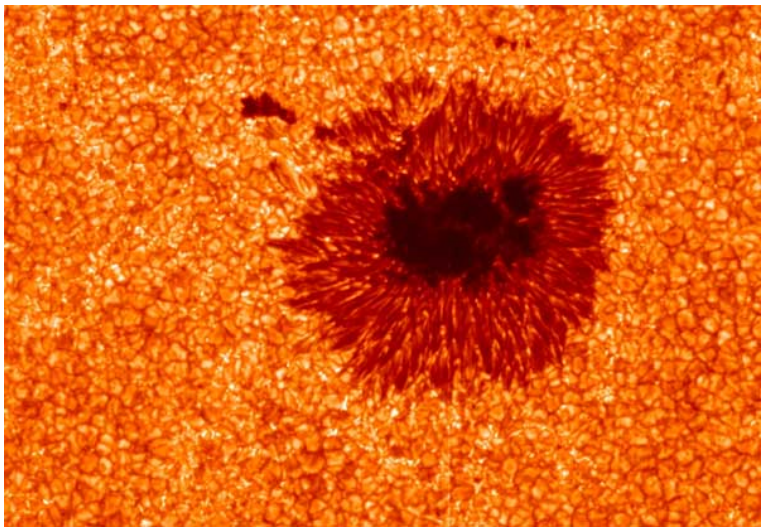

Figure 1.2: This image shows an image of the photosphere, including both granulation and sunspots (credit: NASA/JAXA/PPARC Hinode).

2001).

Perhaps the most obvious features present on the photosphere are sunspots. These can be seen on the solar disk during times of greater solar activity (mainly during solar maximum) as dark spots, though with the advent of modern optics, it is possible to discern greater detail. As can be seen in Fig. 1.2, sunspots consist of a dark region called the umbra, which is about 2000 K cooler than the photosphere, surrounded by a region of approximately radial striations known as the penumbra, which is at about the same temperature as the photosphere. Strong magnetic fields are associated with sunspots, which are thought to suppress convection below the sunspot and thus there is less flow of energy to the surface and hence a lower umbral temperature. The link between sunspots and solar/magnetic activity will be discussed in greater detail later. Sunspots themselves form in pairs, with each spot of a different inward/outward magnetic field polarity. Of the two, there will be one leading spot and one trailing, with the leading spot having the same polarity for all sunspot pairs in a given hemisphere; this polarity swaps in adjacent solar cycles. In the opposite hemisphere, the polarity of the sunspots will be reversed. One of the important implications of sunspot observations has been the knowledge gained about the solar cycle, which will be mentioned in greater detail in section 1.3.5.

1.3.3 Chromosphere

The chromosphere is a relatively thin layer extending a few megametres above the photosphere. The chromosphere is characterised by upward jets of material, the largest being prominences and spicules.

Prominences involve material being held above the solar surface by the magnetic field and can form very large looped structures, extending for tens of megametres above the solar surface. It is also possible to see material falling from the loop of the prominence back to the solar surface. As the material of the loop is held in place by the magnetic field, the structure can remain for hours or even days at a time.

Spicules are smaller scale features, looking like ≈ 5 Mm jets with a typical lifetime of a few minutes. They appear all over the chromosphere and have a temperature of a few thousand K. The speed of the outflow appears to be about 25 km s^{-1}.

1.3.4 Corona

The outermost layer of the solar atmosphere is referred to as the corona. Above the chromosphere lies a thin transition region, beyond which is the corona itself. It is in this transition region that the temperature of the gas rises by two orders of magnitude. The exact height at which this occurs is not a constant but rather depends on local conditions. Once the temperature has reached something of the order of a million degrees we move into the corona. The exact reason for the unexpectedly high temperature of the corona is still an area of research (Lang, 2001), with several theories being tested, including the influences of chromospheric features such as spicules. Each theory thus far postulated has its problems, leaving the very high temperature of the corona as a currently unanswered question.

The corona itself is divided into two regions, the K and F-coronas. Of the two, the K-corona is closer to the Sun and instead of discrete absorption lines, the high temperature causes thermal broadening, resulting in the absorption lines appearing as broad dips rather than sharp lines. The light itself is Thomson scattered and as

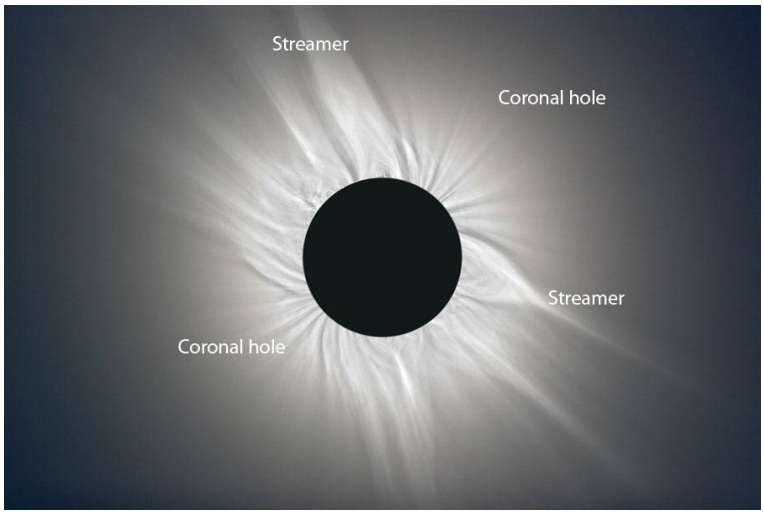

Figure 1.3: The image this figure is modified from (credit: Koen van Gorp) shows the corona as seen during a solar eclipse on 26th July 2009. Regions of closed (streamers) and open (holes) magnetic field can be clearly seen.

a result is very highly polarised. Thomson scattering is important for this thesis, and so it will be the subject of a more in-depth discussion in chapter 3.

The K-corona dominates for radial distances up to 1.5 $R_\odot$ but beyond that the F-corona is the most prominent. The light seen from this region is only weakly polarised as it has been scattered from dust particles. For this reason, the F-corona is sometimes also known as the dust corona. The other very noticeable difference between the K and F coronas is that in the F-corona one does see discrete Fraunhofer lines, i.e. thermal broadening is observed.

In more recent years coronagraphs have been used to artificially occult the solar disc, allowing observations of the corona. These observations reveal a lot of structure within the corona, much of which is as a result of the solar magnetic field. The corona is also the most tenuous of the atmospheric layers, having a density of 10^9 cm^{-3} at the base of the corona compared with 10^{17} cm^{-3} in the photosphere. The phenomena observed are a result of magnetic flux emerging through the photosphere and the plasma being frozen onto the field lines.

Perhaps the two most obvious coronal features are streamers and coronal holes. As can be seen in Fig. 1.3 coronal streamers are seen as elongated arcades of closed magnetic field lines and coronal holes are seen as darker regions, dominated by open

field lines (by open, it is meant that they connect out to the solar wind). During solar quiet times, the streamers tend to be restricted to equatorial regions and the holes to polar regions, however as the Sun approaches solar maximum, this structure becomes more confused with the coronal holes extending/moving to lower latitudes. The open field lines present in coronal holes allow coronal plasma to escape the Sun into the heliosphere and the corona expands into the heliosphere, at which point it is called the solar wind. Coronal holes themselves are sources of faster solar wind and are thought to be behind the formation of corotating interaction regions (CIRs).

1.3.5 The solar cycle

The Sun's magnetic field is frozen into the plasma that makes up the star, which experiences differential rotation. Initially, the magnetic field of the Sun can be thought of as dipolar, but over time, the differential rotation of the Sun causes the magnetic field to wrap around the Sun. This wrapping causes the magnetic tension of the field to increase, and flux eventually starts to poke through the photosphere, causing observable magnetic loops and sunspots (among other features). To release this tension, the field eventually reconnects, leading to high levels of solar activity and returning the field to its dipolar structure, though with the polarity reversed. The number of sunspots observed on the surface of the Sun can thus be used as a proxy for solar activity. As mentioned previously, sunspots appear in pairs, with one of the pair leading the other. These two have opposite polarities. The polarities of each sunspot pair tend to be the same in each solar cycle. For a pair of sunspots in the opposite hemisphere, the order of the polarities of the pair of sunspots will be reversed, i.e. the leading sunspot of the pair will have the opposite polarity to the leading sunspot in the other hemisphere and the same for the trailing sunspot. The sunspots themselves have lifetimes of the order of 100 days. Over the course of a solar cycle, sunspots start off at higher solar latitudes ($\approx 30^{\circ}$) and over time move closer to the equator, also increasing in number. This evolution can be seen in Maunder's butterfly diagram (Fig. 1.4, Priest (1995)). In this diagram, time in years is shown on the x-axis and solar latitude in degrees on the y-axis, with each point representing a single sunspot. The period of time covers two 11 year

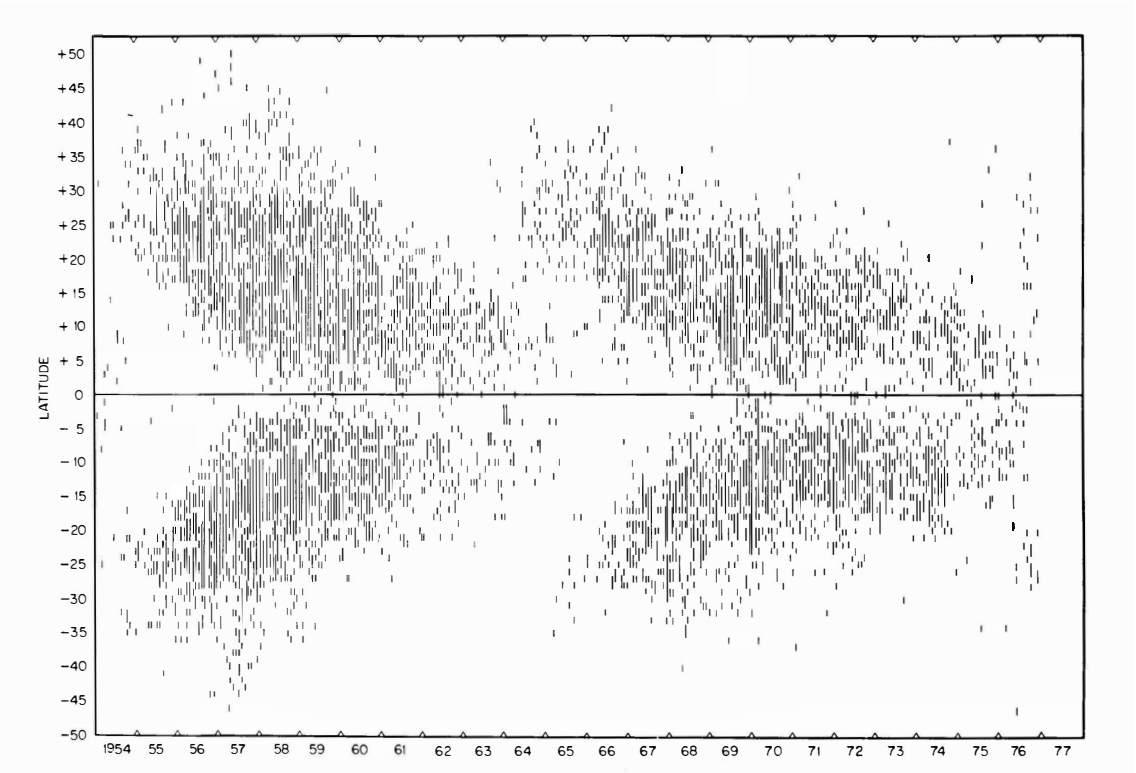

Figure 1.4: An example butterfly diagram showing the movement of sunspots towards the solar equator as a solar cycle progresses. The plot covers the period of time 1954–1977 (x-axis) and shows the solar latitude on the y-axis, with each point corresponding to a sunspot. Two 11 year solar cycles are covered here.

solar cycles and the distinctive 'butterfly'-like plot can be easily seen, showing the movement of sunspots towards the solar equator as the cycle progresses. Once the sunspots have increased in number and are appearing at lower latitudes, they will disappear and others will start reappearing closer to the poles. Their motion follows the solar cycle. Each time the Sun goes from solar maximum back to minimum, the polarity of the magnetic field reverses. It takes about 22 years for the Sun to complete one cycle, i.e. back to the same polarity, but sometimes this is referred to as a pair of 11 year cycles. The solar cycle itself is driven by the solar dynamo, which is thought to be driven from the base of the convection zone.

1.4 The solar wind and interplanetary magnetic field (IMF)

Historically, the existence of the solar wind was inferred from observations of cometary tails, though here we shall start by briefly demonstrating the reasons for its existence. Assuming that the atmosphere of the Sun is exactly neutral (i.e. that $n_{\rm e} = n_{\rm i} = n$) and that the ions and electrons flow together (i.e. that $\mathbf{V}_{\rm e} = \mathbf{V}_{\rm i} = \mathbf{V}$) then Eq. 1.36 becomes

$$\rho \frac{d\mathbf{V}}{dt} = \rho \mathbf{g} - \nabla P, \tag{1.44}$$

with the acceleration due to gravity

$$\mathbf{g} = -\frac{GM_{\odot}}{r^2}\hat{\mathbf{r}}. \tag{1.45}$$

We also need the mass continuity equation (Eq. 1.35) and energy equation, for which we shall assume an isothermal approximation, which when combined with Eq. 1.33 and Eq. 1.34 results in

$$P = 2nk_{\rm B}T, \tag{1.46}$$

which is dependent on the plasma particle number density alone. If we re-write this in terms of mass density then we arrive at Eq. 1.47, where $\langle m \rangle$ is the mean particle mass, $\langle m \rangle = \frac{m_{\rm e}+m_{\rm i}}{2}$.

$$P = \frac{\rho k_{\rm B} T}{\langle m \rangle} \tag{1.47}$$

We shall assume for now that the Sun's atmosphere exists in static equilibrium, i.e. the force of gravity acting on a parcel of material within the solar atmosphere is exactly counterbalanced by the upward force exerted by the pressure. For the pressure gradient to be in the correct direction to satisfy this, the pressure must

decrease with altitude and because of Eq. 1.46 and 1.47 so must both n and ρ. If the atmosphere is in static equilibrium, then $\partial/\partial t = 0$ and $\mathbf{V} = 0$, meaning that the continuity equation (Eq. 1.35) is automatically fulfilled and the momentum equation (Eq. 1.44) reduces to

$$\nabla \mathbf{P} = \rho \mathbf{g}. \tag{1.48}$$

By assuming spherical symmetry of the system (i.e. $P = P(r)$) and Eq. 1.47 we can arrive at Eq. 1.49 below.

$$\frac{dP}{dr} = -\frac{\langle m \rangle g}{k_{\mathrm{B}} T} P. \tag{1.49}$$

In order to simplify Eq. 1.49, a couple of assumptions could be made, most commonly that of either a thin or a thick atmosphere. A thin atmosphere would describe one such as that on the Earth well, however for the Sun the thick atmosphere approximation is more appropriate. For a thin atmosphere, $\mathbf{g}$ could be considered constant throughout the atmosphere, but for a thick atmosphere, $\mathbf{g}$ must be allowed to change with distance from the body in question, in this instance the Sun. As r increases, the pressure then falls to some finite (non-zero) value. Substituting Eq. 1.45 into Eq. 1.49 and solving for P, we find that

$$P(r) = P_0 \exp\left(-\frac{G M_\odot \langle m \rangle}{k_{\mathrm{B}} T}\left(\frac{1}{R_\odot} - \frac{1}{r}\right)\right). \tag{1.50}$$

It is now possible to find the finite value that the pressure must fall to as $r \to \infty$. This turns out to be

$$P_\infty = P_0 \exp\left(-\frac{G M_\odot \langle m \rangle}{k_{\mathrm{B}} T R_\odot}\right) \approx 1.7 \times 10^{-5} \mathrm{N\ m^{-2}}. \tag{1.51}$$

The question is therefore whether the pressure from the local interstellar medium (LISM) is capable of balancing this pressure exerted by the Sun. Estimates of P_{LISM} put it at about 10^{-13} N m^{-2}, which is clearly not sufficient to balance the pressure of the solar atmosphere. Thus, the Sun's atmosphere is not in equilibrium and so

there must be a constant outflow from the Sun, which we call the solar wind.

1.4.0.1 Parker's solar wind solution

Having established that the solar wind forms because the solar atmosphere is not in hydrostatic equilibrium, it remains to be seen what form this expansion takes. What follows is a brief discussion of the solution to this problem as formulated by Parker (1958).

We assume that the velocity of this outflow has the form $\mathbf{V} = V(r)\hat{\mathbf{r}}$, which implies that the continuity equation (Eq. 1.35) now becomes

$$\nabla.\rho\mathbf{V} = 0. \tag{1.52}$$

In spherical polar coordinates, for any $\mathbf{A}$ which only has a radial component,

$$\nabla.\mathbf{A} = \frac{1}{r^2}\frac{\partial}{\partial r}(r^2 A) \tag{1.53}$$

making Eq. 1.52

$$r^2\rho V = constant. \tag{1.54}$$

This expression implies that as one goes to greater and greater distances from the Sun, the mass flux (ρV) must decrease, suggesting that at least one of ρ or V must vary as a function of distance. We once again also need the momentum equation, though this time with a non-zero velocity:

$$\rho\frac{dV}{dt} = -\frac{GM_\odot\rho}{r^2} - \frac{dP}{dr}. \tag{1.55}$$

From these two expressions, it is possible to arrive at Eq. 1.56 which describes how the solar wind velocity changes as a function of distance from the Sun,

$$\frac{dV}{dr} = \frac{V}{r}\frac{\frac{2k_{\rm B}T}{\langle m\rangle} - \frac{GM_\odot}{r}}{V^2 - \frac{k_{\rm B}T}{\langle m\rangle}}. \tag{1.56}$$

There are a whole variety of different solutions to Eq. 1.56, but only one of them will be relevant to the solar wind.

Considering Eq. 1.56 it can be seen that there will be a value of r at which the numerator on its right hand side disappears. This 'critical' value is given by

$$r_{\rm c} = \frac{GM_\odot\langle m\rangle}{2k_{\rm B}T}. \tag{1.57}$$

When $r < r_{\rm c}$, the gravitational term in the numerator dominates over the temperature term, indicating that the corona is gravitationally bound. If $R > R_{\rm c}$ however, gravity can not contain the hot plasma anymore.

Just as there is a critical radius, there is also a critical velocity. When the denominator of Eq. 1.56 goes to 0, one reaches a critical value of V, which also turns out to be the speed of sound in an isothermal gas, given by

$$V_{\rm c} = C_{\rm s} = \sqrt{\frac{k_{\rm B}T}{\langle m\rangle}} = \sqrt{\frac{P}{\rho}}. \tag{1.58}$$

It is possible to analytically solve Eq. 1.56 and if one does, one arrives at the *isothermal solar wind solution* given by Eq. 1.59 below.

$$\frac{V^2}{C_{\rm s}^2} - 2\ln\frac{V}{C_{\rm s}} = 4\ln\frac{r}{r_{\rm c}} + 4\frac{r_{\rm c}}{r} - 3 \tag{1.59}$$

This solution is dependent on T through $r_{\rm c}$ and $C_{\rm s}$ and so as it is an isothermal solution, we can plot different solutions for different (though constant) temperatures, as seen in Fig. 1.5 (Priest, 1995).

At larger distances from the Sun (i.e. $r >> r_{\rm c}$), Eq. 1.59 can be approximated by

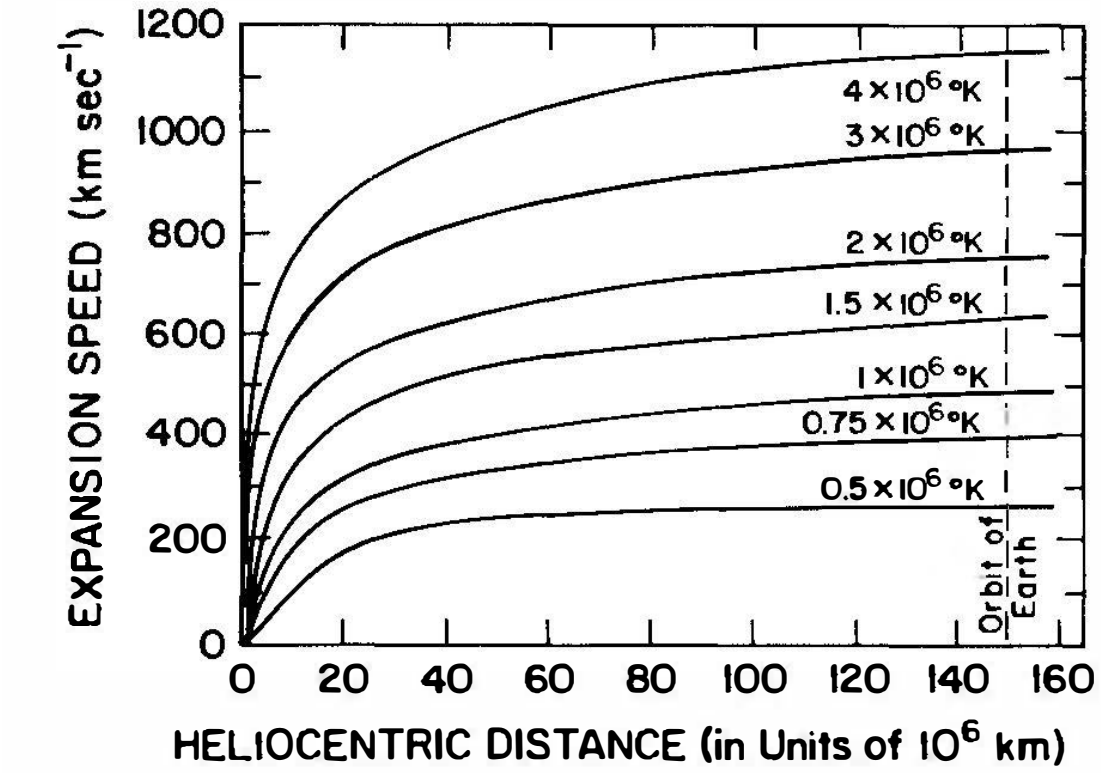

Figure 1.5: A variety of isothermal solutions to Eq. 1.59, with the orbit of Earth shown by a vertical dashed line.

$$V \approx 2C_{\rm s}\sqrt{\ln \frac{r}{r_{\rm c}}}. \tag{1.60}$$

This expression shows only a weak increase of V with r, which is a feature apparent in Fig. 1.5, where the solutions all start to plateau beyond $\approx$ 40–80 million km. If one models the solar wind and allows it to cool as it progresses through the solar system, then one finds that V becomes approximately constant beyond $\approx 10\ {\rm R}_\odot$. Solar wind velocity measurements taken near the Earth show that the velocity generally lies in the range 300–700 km s^{-1}, which is in line with the measured solutions presented in Fig. 1.5 for the temperatures typically measured.

One point worth noting is that the continuity equation states that the product $r^2\rho V$ must be a constant, thus ρV must fall with increasing r. As the material moves away from the Sun, ρ will fall and hence V mus increase further from the Sun.

The solar wind itself is composed predominantly of ionised hydrogen, with

smaller amounts ($\approx$ 8 % by number) of helium and trace quantities of heavier elements. This bias towards lighter elements is very different from ionospheric plasmas, which tend to consist predominately of heavier atmospheric ions.

1.4.1 Interplanetary magnetic field (IMF)

As mentioned earlier, the Sun has its own dynamo which generates a magnetic field. The exact generation process is still an area of active research and we shall not discuss it here. Disregarding all other factors, this magnetic field would appear as a dipole centred on the Sun. A dipole field on its own however would have B increase with latitude such that the field over the pole is twice that at the equator (for a radius, r) and at a given latitude, $B \propto r^{-3}$.

Alfvén's theorem states that, to a good approximation, a magnetic field will be frozen-in to a plasma. Thus, as the plasma moves the field within deforms and the deformed magnetic field can in turn exert a force on the plasma. As the solar wind continually outflowing from the Sun is a magnetised plasma, it drags out the magnetic field lines from the Sun with it, distorting the otherwise dipolar field. After some time, each field line will then point radially outwards (or inwards, depending on the sense of the field at the surface). As Ampére's law states that gradients in **B** must have associated currents, there will be a current sheet running around the equator separating the two oppositely directed hemispheres. The field strength will then vary as

$$B_{\mathrm{r}} \approx \frac{1}{r^2} = B_0 \left(\frac{R_\odot}{r} \right)^2 \tag{1.61}$$

where B_0 is the surface field strength.

In addition to solar wind outflows, relative to the Earth, the Equator of the Sun rotates with a period of about 26 days. The solar wind outflow from the Sun is purely radial and the magnetic field lines are frozen into this flow, but they are also frozen to the surface of the Sun (which is also a plasma), which is rotating. As a

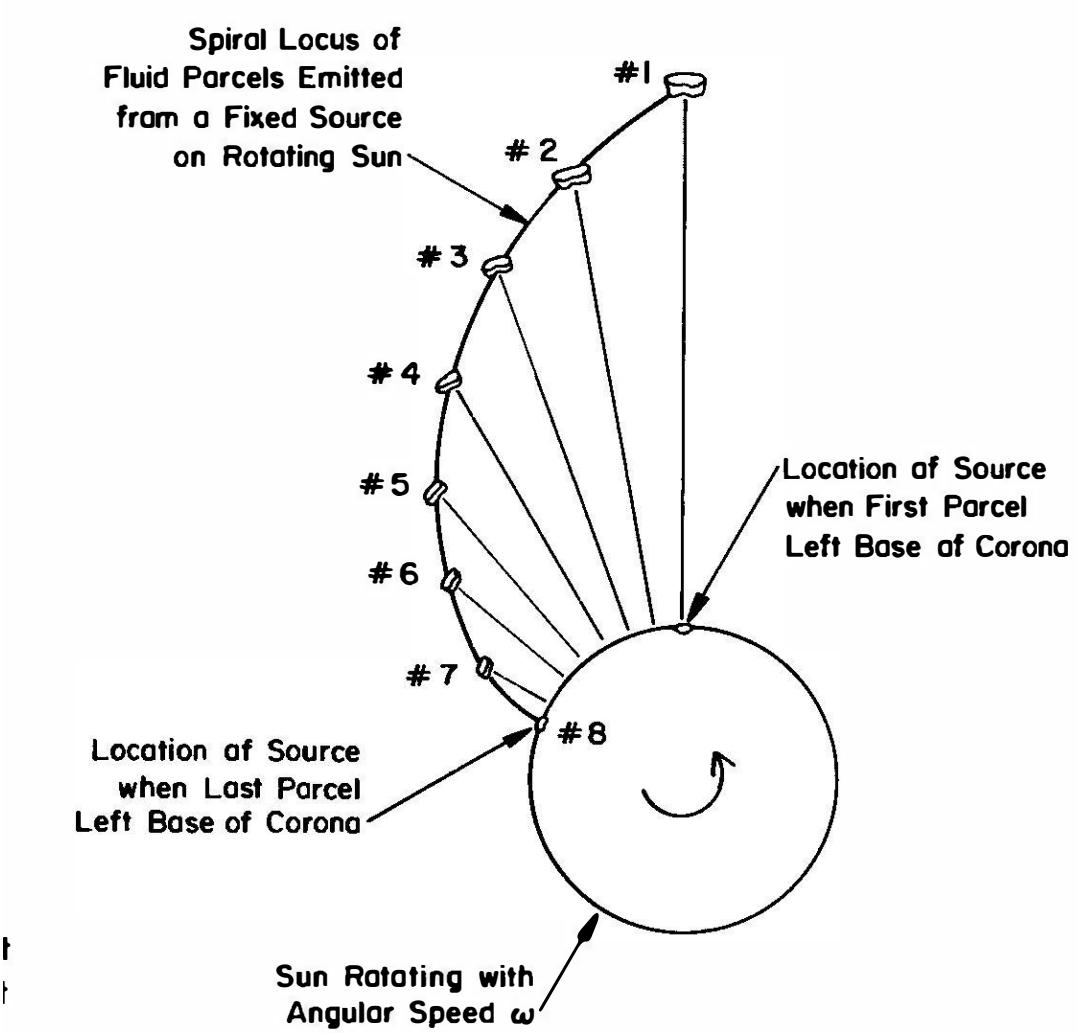

Figure 1.6: Loci of a series of plasma elements emitted at a constant speed from a single source region that corotates with the Sun (Hundhausen, 1995).

result of this, field lines are bent into a spiral located along all the loci of plasma elements emitted from the solar surface (as illustrated in Fig. 1.6 (Hundhausen, 1995)). The spiral pattern that can be seen here is known as the *Parker Spiral*. Near the equatorial plane, the Parker spiral lies in the plane itself, however far above (or below) the equatorial plane, the field lines are on conical surfaces as in Fig. 1.4.1 (Milan, 2011).

It is possible by including all these factors together to arrive at expressions for the Sun's magnetic field as it moves through the solar system, known at this point as the interplanetary magnetic field (IMF, also known as the Heliospheric Magnetic Field, or HMF). Here we shall simply quote the results without going into the details

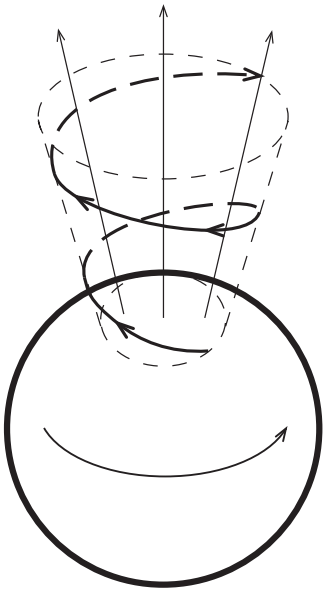

Figure 1.7: The form that IMF lines take far from the equatorial plane.

of the solution methods. As the magnetic field is wound into cones, it has a radial and an azimuthal component ($B_{\rm r}$ and B_ϕ respectively) but no colatitude component ($B_\theta = 0$). These turn out to be

$$B_{\rm r} = B_{\rm r0}\left(\frac{R_\odot}{r}\right)^2 \tag{1.62}$$

and

$$B_\phi = -\frac{\omega_\odot R_\odot}{V}\sin\theta\left(\frac{R_\odot}{r}\right)B_{\rm r0} \tag{1.63}$$

with $\omega_\odot$ the rotation speed of the Sun.

As it is of importance to this thesis, we'll consider one complication to the picture presented above. In the discussion so far we have assumed that the plasma energy density is greater than the magnetic energy density (this is necessary in order to have the plasma pull the magnetic field with it rather than vice versa). The conditions closer to the Sun however are quite different. Here, the magnetic energy dominates over the plasma energy, and so instead of the plasma flowing out and pulling the field with it, the magnetic field confines the plasma, restricting it to moving along the closed magnetic field lines on which it sits. As a result of this, there are closed arcades of magnetic field close to the equator, which contain trapped, hot, high density coronal plasma. Nearer to the poles the field lines are more radial and so

the material is able to escape more easily, resulting in higher latitude outflow being more tenuous and cooler than that at lower latitudes. These high latitude regions are known as coronal holes and are a dominant source region of solar wind outflow. The region close to the Sun where magnetic energy dominates over that of the plasma is very close to the Sun as $E_{\text{mag}} \propto r^{-6}$ and so as one moves further from the Sun, the plasma energy quickly dominates over the magnetic energy. Fig. 1.3 shows that the magnetic field lines clearly traced out by the coronal material being observed, showing the dominance of the magnetic field over plasma pressure close to the Sun.

1.4.2 The solar wind and local interstellar medium (LISM)

After some time, the solar wind ram pressure will fall to the static pressure of the LISM. The flow of both the solar wind and LISM are supersonic and so a shock forms between the two of them, with a bow shock in the LISM and a terminating shock in the solar wind. The interface between the two is the heliopause and the region inside the heliopause, dominated by the solar wind, is the heliosphere. This description has been created based largely upon observations of planetary magnetospheres and their interactions with the solar wind. There are few data regarding the interaction between the LISM and solar wind however and the only spacecraft to have reached this region is Voyager 1 in 2013 and work is still ongoing to better understand how this interaction works.

1.5 Solar wind transients

The flow of the solar wind from the Sun out into the heliosphere is not one of continuous uniform emission. Solar activity dictates conditions in the solar wind, resulting in various different density features that propagate out and have implications for planetary magnetospheres, including our own. These are known as solar wind transients. The main two types of transient are coronal mass ejections (CMEs) and corotating interaction regions (CIRs). What follows is a brief description of each

including their implications for planetary magnetospheres. A more full discussion can be found in Chapter 3.

1.5.1 Coronal mass ejections (CMEs)

Thought to be the result of magnetic reconnection on the solar surface, a coronal mass ejection is often preceded by a solar flare and consists of a large quantity of coronal material being ejected into the heliosphere. This material tends to be faster than the slow solar wind, though it can have a wide range of speeds (typically 400–2000 km s^{-1}). As it potentially contains very fast and very dense material, there are implications for planetary magnetospheres. The speed means short transit times to the planet in question (transit times to 1 AU of $\approx$ 1 day are possible). The CME typically has shocks that both preceed it and follow it. When the CME material encounters a planetary magnetosphere, such as that at Earth, it can inject larger amounts of material into the magnetosphere through magnetic reconnection and can cause geomagnetic storms. CMEs that travel faster than the surrounding solar wind are accompanied by a shock that compresses the front of a magnetosphere that it encounters.

1.5.2 Corotating interaction regions (CIRs) and stream interface regions (SIRs)

The second type of solar wind transient discussed here, CIRs, are caused by two solar wind populations with different velocities interacting. If one considers two source regions on the solar surface, one ejecting solar wind material at a higher speed than the other, then, assuming radial outflow, the faster material will catch up with the slower material in front of it as the Sun rotates. As each population of plasma is frozen onto its magnetic field lines, then the faster material cannot pass through and move ahead of the slower. This results in a density build up. So, one sees ambient solar wind, followed by a compression region, then a rarefied region and then a return to the ambient solar wind conditions. As the source regions corotate with

the Sun, the compression region forms a Archimedean spiral that propagates into the heliosphere and is known as an SIR. If the feature persists for at least a complete solar rotation, it is referred to as a CIR. I will use the two terms interchangeably.

As a CIR requires the existence of solar wind source regions of differing natures (ejecting material at differing speeds), from our previous discussion of the Sun one might wonder whether it is possible to observe them in the ecliptic plane at all. Previously we had stated that coronal holes (sources of faster solar wind material) tended to occur around the poles. Despite this, smaller coronal holes do occur in other regions of the corona, allowing CIRs to form closer to the ecliptic plane. This is especially true approaching solar maximum when the polar holes can distend in shape and expand so that part of them does indeed reach towards the solar equator.

Unlike a CME, a CIR will not necessarily have an accompanying shock. Especially in the inner solar system (when encountering the rocky planets) a shock will not have formed, but there will instead simply be an observed density enhancement. The further out into the heliosphere the CIR travels, the more likely it is that a shock will form. Again, in contrast to a CME, which is a single explosive event, the solar wind source regions that give rise to a CIR can persist for multiple solar rotation. They also cause enhanced magnetic field strength that can persist for many hours.

1.6 Summary

The Sun is the star of our solar system and has plasma flow from the surface into interplanetary space. Differential rotation causes the Sun's initially dipolar magnetic field to become wrapped around the star, resulting in complex active regions and high levels of activity. Impulsive eruptions of material (CMEs and CIRs) caused by this activity have an impact on planetary bodies (including the Earth) that they encounter.

Chapter 2

Literature review

In this section, I discuss two of the main types of solar wind transient, the CME and CIR in more detail. I also discuss Thomson scattering, as that is the scattering mechanism by which transients are observed in coronagraphs and heliospheric imagers, and fitting techniques, designed to extract propagation information about transients as seen in heliospheric imagers.

2.1 Coronal Mass Ejections

CMEs are eruptive events that launch large amounts ($\approx 10^{12}$ kg) of coronal plasma into the heliosphere. The initiation mechanism behind CMEs is not fully understood, though we do have some knowledge of how CMEs are released into the solar wind. Initially it was thought that CMEs were caused by solar flares (Chapman, 1950), and while there is a correlation between solar flares and some CMEs, more recent observations indicate that CMEs are caused by large scale magnetic flux features emerging through the solar surface, with different types of CME being associated with different shapes and orientations of field structure (Bravo *et al.*, 1998). I shall next describe some of the ideas and models used and tested to explain CMEs.

Most theories of CME initiation start with an existing magnetic field configura-

tion (often a prominence). The footpoints of these magnetic field lines are linked to active regions in the photosphere. The movement of these active regions causes shearing and stressing of the field lines and an increase in magnetic energy density leading eventually to an abrupt eruption. Forbes (2000) showed that in order for an eruption to take place, the current associated with the magnetic shearing must be either force-free (the magnetic field strength is assumed to dominate over the plasma pressure) or confined to the current sheets, as the magnetic energy density must be greater than the thermal and gravitational energy densities. Theories of energy storage density are thus divided into two categories, those that focus on force-free currents and those that focus on current sheets. In the same way, there are multiple proposed models of energy release, each of which will be discussed in some more detail below:

1. Ideal MHD
2. Resistive MHD
3. Hybrid
4. Non-force-free

The first three model groups are all different types of force-free models. For a model to be force-free, it assumes that the dominant force is that exerted by the magnetic field lines, i.e. that forces due to gravity and plasma pressure are negligible by comparison. In the first instance, researchers have attempted to initiate a CME using only ideal MHD. In such models, dissipative process, such as magnetic reconnection are assumed to play no role in the eruption of magnetic flux. One example of such a model was created by Wolfson (1993), however he was unable to establish if the transition from closed to open states were actually possible without reconnection and hence it if were possible using only a loss in MHD stability.

Resistive MHD models no longer use pure ideal MHD. The idea is to incorporate dissipative processes (such as magnetic reconnection). In Fig. 2.1 can be seen the time evolution of a particular model of Mikic and Linker (1994). Looking first at

2.1 a), from time $t = 0$ to $t = 524\ \tau_A$ (τ_A is the Alfvén time, i.e. how long it takes a wave travelling at the Alfvén velocity ($v_\mathrm{A} = B/\mu_0\rho$) to cross the plasma in question) the magnetic arcade is sheared with a resistivity as close to 0 as possible. If the resistivity then does not change, the configuration quasi-statically opens, with no eruptive event. In order to get an eruption therefore, at $t = 540\ \tau_A$, the resistivity is suddenly increased such that the magnetic Reynold's number $R_m \sim 10^4$. This results in magnetic reconnection and the formation of a flux rope that is expelled away from the Sun. In order for this model to work however, a sudden change in reconnection rate is required such that it is slow enough before the eruption to allow energy to be stored in coronal currents and fast enough following the eruption to release the stored energy rapidly. How this sudden change in reconnection rate would come about is unclear, though Mikic and Linker (1994) suggested some kind of microinstability. In panel b) can be seen a plot of the ratio of total energy to potential energy against time. Once energy has been stored up, it is only released in the case for which the resistivity is suddenly changed as can be seen. If the resistivity is still 0, then the energy remains stored in the magnetic field.

The third type of model is a hybrid between the two others outlined above. The idea is to use a resistive MHD model and hence use reconnection, but then use an ideal MHD process to introduce a sudden current sheet and thus get a rapid change in reconnection rate instead of invoking a microinstability. An example of such a model by Lin *et al.* (1998) is shown in Fig. 2.2. In this figure, panel (a) shows the magnetic configuration before the eruption and (b) that after the eruption. In this example, the strength of the photospheric field (taken to be a simple dipole centred on the Sun) is reduced by making the field line footprints in each hemisphere migrate equatorward and then reconnect, transferring energy to the coronal currents via the poynting flux ($\mathbf{S} = \mathbf{E} \times \mathbf{B}/\mu_0$). There is then a flux rope that is suspended in the corona by balancing magnetic tension, compression and curvature forces. If the photospheric field is then decreased (in the manner described previously) then this balance is broken and the flux rope moves to a new equilibrium position at a greater distance from the Sun and a fraction of the stored energy ($< 10\%$) is released. Reconnection at the current sheet then allows the flux rope to escape into interplanetary space.

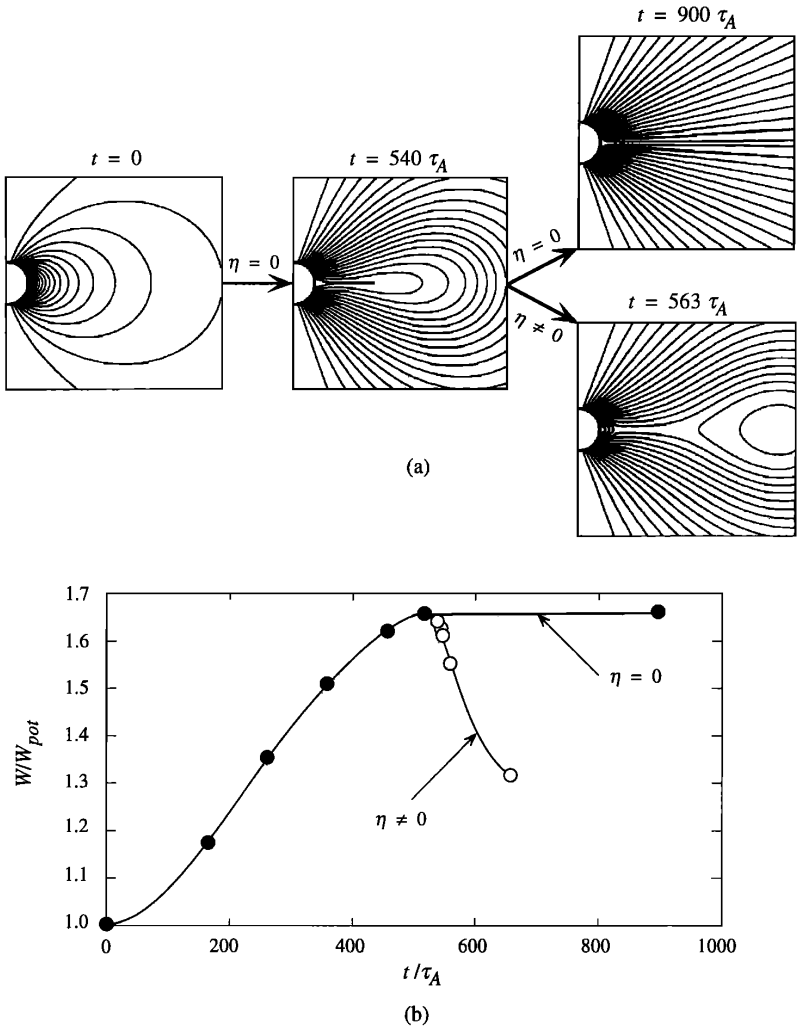

Figure 2.1: Showing the time evolution of a resistive MHD model of CME formation including a sudden increase in resistivity ($\eta \neq 0$) and no change in resistivity ($\eta = 0$ in panel a). Panel b) shows the corresponding time evolution of total energy divided by potential energy.

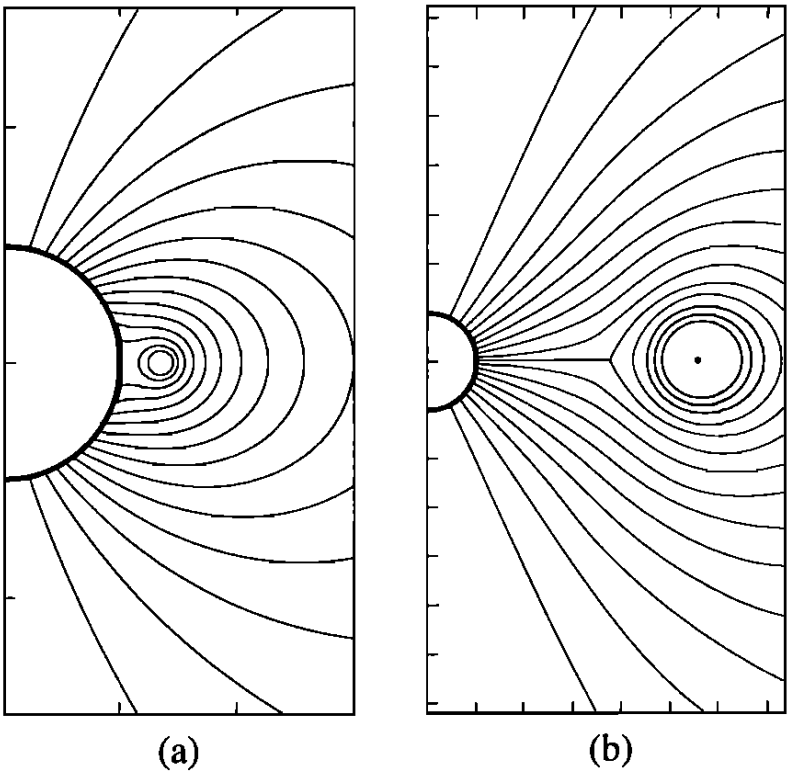

Figure 2.2: An axially symmetric flux rope model showing the ideal MHD transition from (a) a high energy equilibrium state before eruption to (b) a lower energy equilibrium state after eruption.

The final category of model discussed here is that which is not force-free. It is clear that magnetic forces dominate in the corona, however non-force-free models consider the effects of the smaller contributions from gravity and plasma pressure and investigate whether this can induce CMEs. It has been seen for example that prominence material can fall back to the Sun, and so gravitational forces clearly have a role to play. One idea has been that the prominence acts as a "lid" over a part of the magnetic field, allowing the magnetic energy to built up to a greater extent than would otherwise be the case. When some of this material falls back to the Sun, the weight of the prominence is no longer enough to contain the magnetic flux, allowing it to at least form a current sheet (Low, 1999). One problem with this idea is that there have been CMEs observed that contain no prominence plasma, so even assuming that the mechanism works, it cannot explain all observed CMEs. There are also potential effects from plasma pressure. The pressure reduces the magnetic energy that can be stored in the corona, but (unlike gravity) it can propel material outward, away from the Sun. Investigations considering the effects of pressure have struggled

to find thermal energy densities of sufficient magnitude in the lower corona to make effects from plasma pressure significant. A variety of authors have considered the effects of both gravity and pressure, so for more information on these efforts see Low and Smith (1993), Wolfson and Dlamini (1997) and Wolfson and Saran (1998).

In-situ observations of CMEs are limited by the fact that there is no single in-situ feature that can be used to identify a CME. There are however a variety of features that when seen together make it very likely that a CME is being observed (Neugebauer and Goldstein, 1997).

Many observations of CMEs have been made using remote-sensing instruments, primarily coronagraphs, mounted both on spacecraft and on the ground. From coronagraph observations, CMEs can be split into two categories, regular CMEs and halo CMEs. More recent observations away from the Sun-Earth line have confirmed that these two categories of event have no physically meaningful difference apart from the direction of propagation relative to the observer. A CME is limited in spatial extent both in latitude and longitude (Hundhausen, 1993) and if observed propagating away from the Sun-Earth line is seen (from the Earth) as a regular CME and if it is directed along the Sun-Earth line, then it is seen as a halo CME. If a halo CME is observed, then without observations away from the Sun-Earth line, the only way of determining if the event is directed towards or away from the Earth is to either have an upstream detector, or measure the event if/when it arrives at Earth.

Depending on whether they are associated with solar flares (Cremades and Bothmer, 2004) or prominences (Savani *et al.*, 2009), CMEs have different expansion rates, speeds and rates of acceleration (Andrews and Howard, 2001). The speeds themselves can vary widely, ranging from very slow events (≈ 200 km s^{-1}) to faster events with speeds of more than 1000 km s^{-1}. If a CME is associated with a prominence, then it accelerates from an initial comparatively low speed up to that of the background solar wind (Andrews and Howard, 2001), while those associated with flares accelerate much faster close to the Sun, reaching higher speeds and giving the appearance through a coronagraph field of view of constant flow speed. As extracted

from coronagraph observations, the occurrence rate of CMEs has been estimated as varying between 0.8 per day (low solar activity (Howard *et al.*, 1997)) and 3.5 per day (high solar activity (Gosling, 1997)).

Comparing CMEs and CIRs, CMEs tend to have the larger effect on planetary magnetospheres as they lead to more extended durations of southward IMF, and hence a lot of coupling between the solar wind and magnetosphere, and the presence of shocks.

2.2 Corotating Interaction Regions

CIRs consist of high density regions in the solar wind that corotate with the Sun. They are persistent features, potentially remaining for multiple solar rotations. Their impact on planetary magnetospheres is less extreme than those of CMEs, but can be recurrent a solar rotation later, leading to a 27-day periodicity in geomagnetic activity (Richardson, 2006). As can be seen in Fig. 2.3, a CIR is formed by adjacent regions of fast and slow solar wind, such that the fast solar wind source region ejects material which catches up with slower material ahead of it as the Sun rotates. As a result of Alfvén's theorem, the two plasma populations cannot mix and hence there is a pileup of material. This causes a denser and higher pressure region of material thought to propagate at an intermediate speed, with a faster, rarefied region following it (Parker, 1963). As the source region of the fast solar wind corotates with the Sun, so too does the CIR. The fast solar wind will have its source in a coronal hole (Hundhausen, 1972), with the open field lines allowing material to escape the Sun at a higher speed than from regions of closed magnetic field. Although coronal holes are generally found at the solar poles, they can sometimes extend down to lower latitudes, allowing CIRs to form at the equator. In general a CIR does not have accompanying shocks, however at larger radial distances, the fast stream will continue to impinge on the slower stream and a pair of shocks, one in each stream can form (Lee, 2000). The shocks are not normally seen at Earth, and will generally form at distances greater than 3–5 AU.

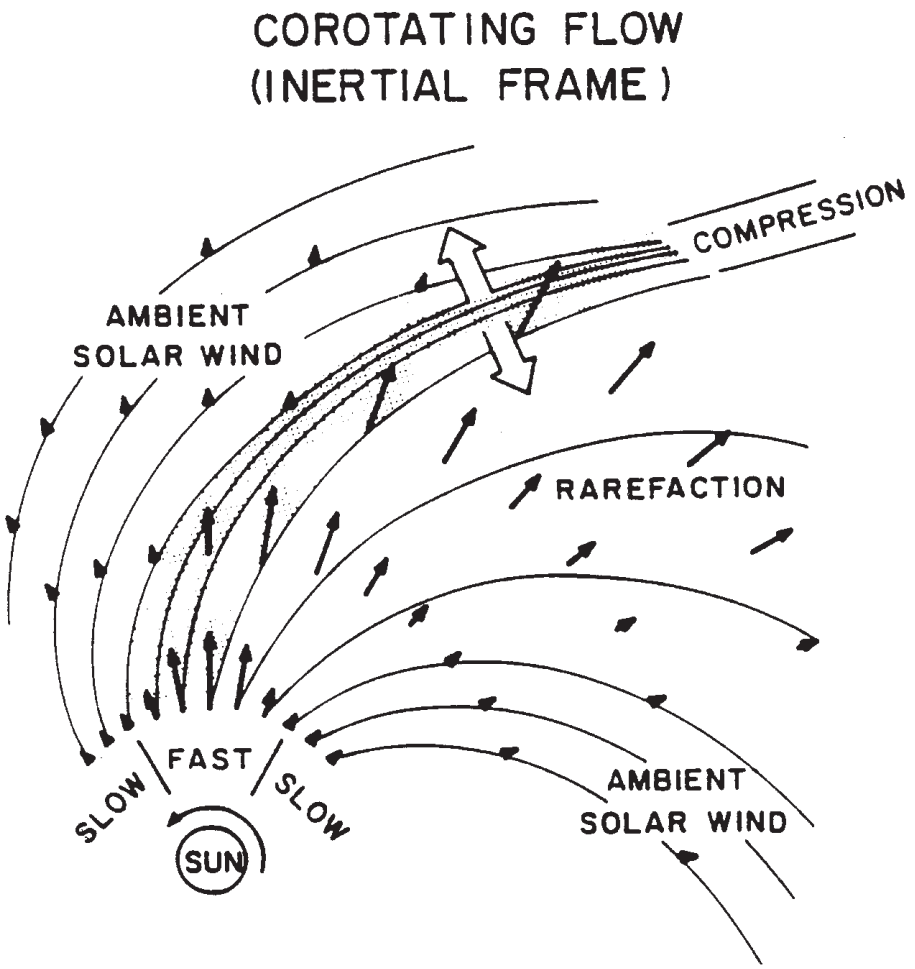

Figure 2.3: Showing the structure of a CIR. This structure corotates with the Sun.

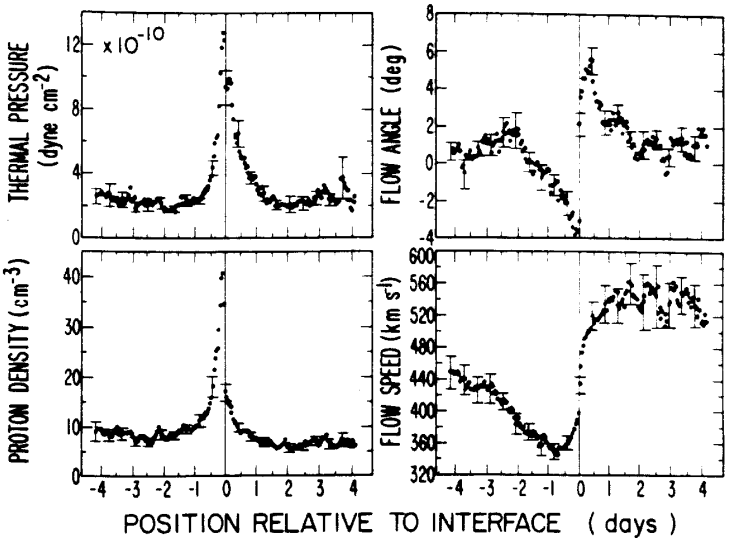

Figure 2.4: A superposed epoch analysis of 23 CIR events showing the behaviour of the thermal pressure, flow angle, proton density and flow speed and showing some typical CIR characteristics.

In Fig. 2.4 can be seen a superposed epoch analysis of 23 CIR events taken from Gosling *et al.* (1978). Preceding the CIR is a region of low pressure, density and flow speed, which is to be expected from the background solar wind. As the interface approaches, the flow angle turns negative and the flow speed drops (the flow stream at the interface is deflected westward, i.e. in the direction of the planetary motion, by the interface). In addition to this we see the pressure and density rise at the same time. At the interface itself the flow angle turns positive, indicating the presence of a fast stream at the rear of the interface being deflected eastward by the interface (Gosling and Pizzo, 1999).

Throughout the late 1990s and early 2000s there have been a plethora of in-situ observations made. Mason *et al.* (2009) took in-situ measurements of CIRs from the STEREO, Wind and ACE spacecraft during the 2007–2008 solar minimum. At this time the STEREO spacecraft were separated by $\sim 80^{\circ}$, allowing observations to be made away from the Sun-Earth line. They found that there was significant variation in CIR properties as measured at the different spacecraft used, indicating variations as the Sun rotates of the order of days to weeks. They then compared the data from this epoch with that from the previous solar minimum, 1997–1998, finding the more recently solar minimum to be much richer in CIRs. Williams *et al.* (2011) also use multiple spacecraft in-situ measurements to track CIRs from the Sun out to the orbit of Mars. To do this they used data from the ACE, Mars EXpress (MEX), Venus EXpress (VEX) and STEREO spacecraft. CIRs were identified at ACE and then their arrival times predicted at each of the spacecraft. They found that the arrival of CIRs could be reliably predicted in this way.

Early remote observations of CIRs were made by coronagraphs (for example Large Angle and Spectrometric COronagraph, LASCO, on SOlar and Heliospheric Observatory, SOHO) and as such limited to small elongation angles. More recent missions such as Coriolis and STEREO have allowed remote observations out to 1 AU with heliospheric imagers. Sheeley *et al.* (2008) used observations made by STEREO-B HI together with in-situ measurements to identify CIR features in the heliospheric imagers. They compared wave fronts seen in HI sweeping past the Earth with in-situ plasma and magnetic field measurements taken by near-Earth

spacecraft (including Wind) and found almost all of the strong CIRs identified in situ to be coincident with a large white light wave as seen in HI. As the Sun was dominated by "long-lived and recurrent solar wind streams" at this time, they state that the HI observations correspond to CIRs.

A CIR contains a magnetic field stronger than that of the background solar wind and it is this enhanced field that can lead to significant effects on planetary magnetospheres. This magnetic field can couple with the planetary magnetic field, allowing the CIR to trigger magnetospheric storms. The magnetic field associated with a CIR is less intense than that associated with a CME, and as the rising phase of a storm is associated with IMF B_z (the component of the IMF nrmal to the ecliptic plane), this leads to CIR-driven storms being less intense than those associated with CMEs (Richardson, 2006). It was noted as early as Greaves and Newton (1928) that recurrence was a property of smaller geomagnetic storms, but not larger. There is about an equal number of CIRs dominated by southward and northward B_z, and as a result of this, about half of CIRs don't have associated storms at all (Tsurutani *et al.*, 2006a), and those that do, generate small/moderate storms (Tsurutani *et al.*, 2006b).

2.3 Thomson Scattering

Thomson scattering is the mechanism by which sunlight is scattered from coronal material and observed by coronographs and heliospheric imagers. It is the low energy limit of Compton scattering and as such is the elastic scattering of electromagnetic radiation by a free charged particle, where the kinetic energy of the particle and frequency of the photon are the same before and after scattering, which will be the case as long as the mass energy of the particle is much greater than the energy of the photon.

The scattering strength for a particular electron depends on the angle, χ, between the line of sight and the solar radial through the electron. The geometry of the problem can be seen in Fig. 2.5 (Howard and DeForest, 2012). In this diagram,

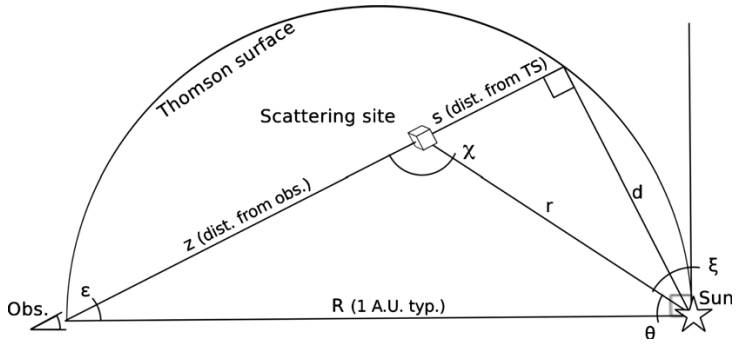

Figure 2.5: Shows the geometry associated with Thomson scattering.

R is the Sun-observer distance, r the heliocentric distance of the scattering centre, d the impact radius (explained shortly), θ the 'direction of propagation', (defined later in this work as ϕ and also labelled in some literature as β) and ϵ the elongation angle (in some literature labelled α). The scattered emission has a maximum when the line of sight is at the closest approach to the Sun, i.e. when the line of sight is perpendicular to the radius through the scattering angle, when $\chi = 90°$, as this will be where the plasma is at its densest. This radius is the *impact radius*. Tracing out the loci of the points where χ is 90° therefore shows the surface at which the scattering is at a maximum and this surface corresponds to that of a sphere, known as the Thomson surface (TS). This sphere has a diameter that passes through both the Sun and the observer and can be seen in Fig. 2.5. What follows is a brief description of some of the theory as outlined by Howard and DeForest (2012).

The differential scattering cross-section can be written as

$$\frac{d\sigma}{d\omega} = \sigma_t(1 + \cos^2\chi), \tag{2.1}$$

i.e. light incident on a particular small cross-sectional area ($d\sigma$) in the vicinity of an electron will be scattered into a small solid angle ($d\omega$) and this expression describes how this cross-section varies with scattering angle. Here, $\sigma_t = r_e^2/2$. At a large distance from the Sun ($r >> r_\odot$), a single electron will encounter a certain known intensity of sunlight and so will scatter a certain amount of power into each differential solid angle, given by

$$\frac{dP}{d\omega} = \sigma_t(1 + \cos^2\chi)\left(\frac{\pi r_\odot^2}{r^2}B_\odot\right), \tag{2.2}$$

where $B_\odot$ is the solar radiance, a known constant. In practice however, a single electron is not detected by a heliospheric imager, instead using a density of electrons (n_e) is more appropriate and then the power radiating from some small volume can be considered ($dV = dAds$, with s a length and A an area perpendicular to it). We then have the radiance, dB of Thomson scattering from a smaller volume dV located at a large distance from the observer,

$$dB \equiv \frac{dP}{d\omega dA} = \sigma_t(1 + \cos^2\chi)\left(\frac{\pi r_\odot^2}{r^2}B_\odot\right) n_e ds. \tag{2.3}$$

By choosing s to be along a line of sight, this expression can be integrated to give the surface brightness at an instrument observing heliospheric features

$$B(\epsilon, \alpha) = B_\odot \sigma_t \pi r_\odot^2 \int r^{-2}(1 + \cos^2\chi) n_e(s, \epsilon, \alpha) ds \tag{2.4}$$

with α an azimuthal angular coordinate. This expression can be simplified by applying the sine rule to the triangle (ϵ, χ, θ) to arrive at an expression for the contribution to the radiance made by each small packet of electrons along the line of sight

$$dB(s, \epsilon, \alpha) = \{(B_\odot \sigma_t \pi r_\odot^2)(R\sin\epsilon)^{-2}\}\left[\sin^2\chi(1 + \cos^2\chi)\right] n_e(s, \epsilon, \alpha) ds. \tag{2.5}$$

This expression consists of a non-geometric component (i.e. not dependent on χ) in curly brackets and a geometric component (dependent on χ) in square brackets. Considering the geometric component of this expression, it will indeed be at a maximum when $\chi = 90°$, but because $\sin^2\chi$ term maximises when the $1 + \cos^2\chi$ minimises, the peak of this function is actually quite broad. Relabelling this term as G and simplifying, $G = 1 - \cos^4\chi$. Fig. 2.6 (Howard and DeForest, 2012) shows G (which they call the sensitivity factor) plotted as a function of scattering angle. It can be seen that the 'peak' of the function is very broad (in fact Howard and De-

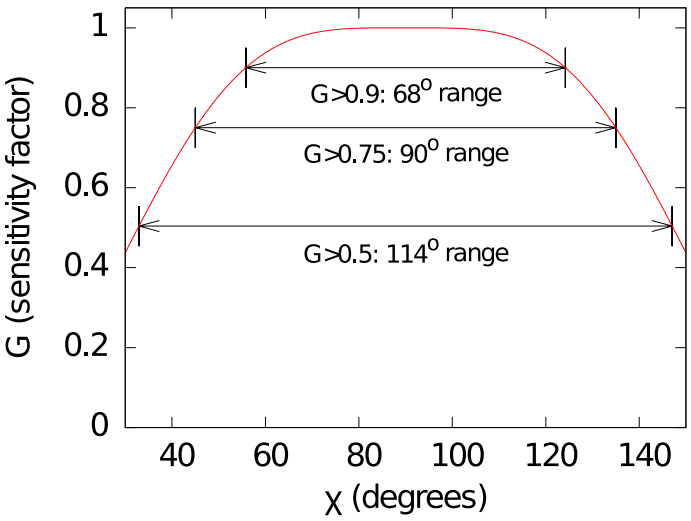

Figure 2.6: Showing the sensitivity factor as a function of scattering angle, with the Thomson plateau clear to see. This assumes that the electrons follow a Maxwellian distribution.

Forest (2012) call this the "Thomson plateau"), covering a wide range of scattering angles. As a result of this, it is possible to see some features very clearly that are not on the Thomson surface. It actually occurs that at a fixed distance from the Sun, HI is actually more sensitive to material further from the Thomson surface.

It was Vourlidas and Howard (2006) who demonstrated that the Thomson scattering signal per unit electron density in the heliosphere is maximised on the Thomson sphere, however it is important to note that:

1. Objects along a particular line of sight grow faint far from the Thomson sphere
2. Objects at a particular distance from the Sun grow brighter far from the Thomson sphere

so, it is not accurrate to say that only objects on or near the Thomson sphere are visible.

For a more detailed discussion of Thomson scattering see Vourlidas and Howard (2006), Howard and Tappin (2009) and Howard and DeForest (2012).

2.4 J-maps

The raw images taken from the STEREO HI need to undergo some significant post-processing before they are suitable for scientific use. The background will need to be subtracted from the images. In this way it should be possible to remove the (roughly constant) F corona. Running differenced images from either COR or HI observations should then be taken to emphasise the motion of relatively faint material in the corona (Sheeley *et al.*, 1997). In Fig. 2.7 (Harrison *et al.*, 2012) can be seen a series of panels showing HI images. These images are in two groups. The top 6 panels show the time evolution of the corona with background subtracted. In the bottom 6 panels one can see identical images, however this time a running differencing technique has been used to emphasise the motion of material. In the top left panel of each group can be seen contours of elongation angle and in the running difference images some CMEs have been labelled with letters. It is much easier to identify moving coronal features in the bottom panels. One can then take a single strip (or strip of fixed angular width) along a particular direction of interest, and then by rotating these strips such that they are vertical and stacking them horizontally, one creates a plot of intensity as a function of elongation and time, known as a J-map. Fig. 2.8a (Davies *et al.*, 2009) shows the field of view of the two HI on STEREO-A. The Sun is off to the right hand side (at an elongation of 0°) and the Earth to the left. A time series of images of the rectangular area highlighted in Fig. 2.8a) can be seen in Fig. 2.8b). In this sequence of images a region of denser plasma can be seen moving across the instrument field of view, to increasing in elongation. By taking the strip of pixels along the propagation direction of this density enhancement at subsequent time steps, a J-map can be formed, an example of which can be seen in Fig. 2.9. The top panel (Williams *et al.*, 2009) shows a number of anti-sunward flows, with a particularly bright example being typical of a CME, with prominent near-horizontal planetary traces. In the lower panel is an example showing families of traces, more typical of CIRs. In both of these examples the slices used to form a J-map are taken along the Sun-Earth line, however in principle there is no requirement for this to be the case. Having constructed a J-map, it is then possible by using one of the techniques outlined in the next section to estimate propagation

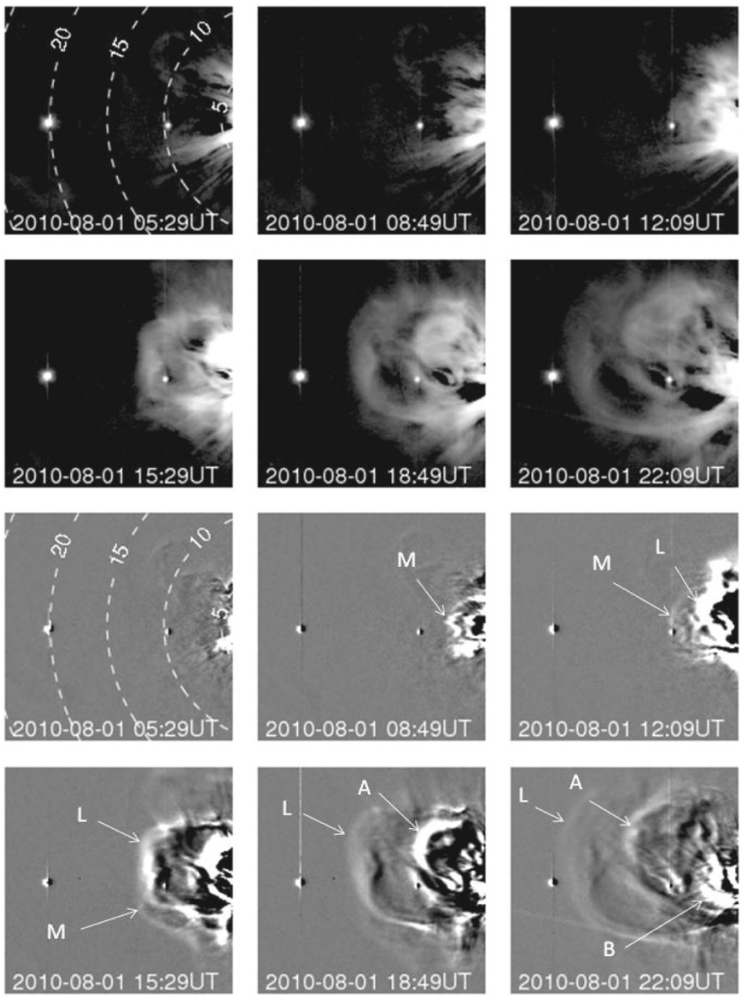

Figure 2.7: Taken from Harrison *et al.* (2012), this shows the difference between background subtracted images (top 6 panels) and running differenced images (bottom 6 panels). In the bottom panels, some CMEs have been labelled with letters.

information related to an observed solar wind transient.

2.5 Fitting Techniques

As first proposed by Sheeley *et al.* (1999), the variation of elongation with time of a transient can be extracted from a J-map and used to estimate its speed and direction of travel (Wood *et al.*, 2010; Liu *et al.*, 2013). In this section, I review the techniques available to achieve this, and how they have been applied in the past to observations made from the viewpoint of a single spacecraft. The techniques discussed below are normally applied in the ecliptic plane, although they can also be applied out of the ecliptic. There are versions of each technique that apply to

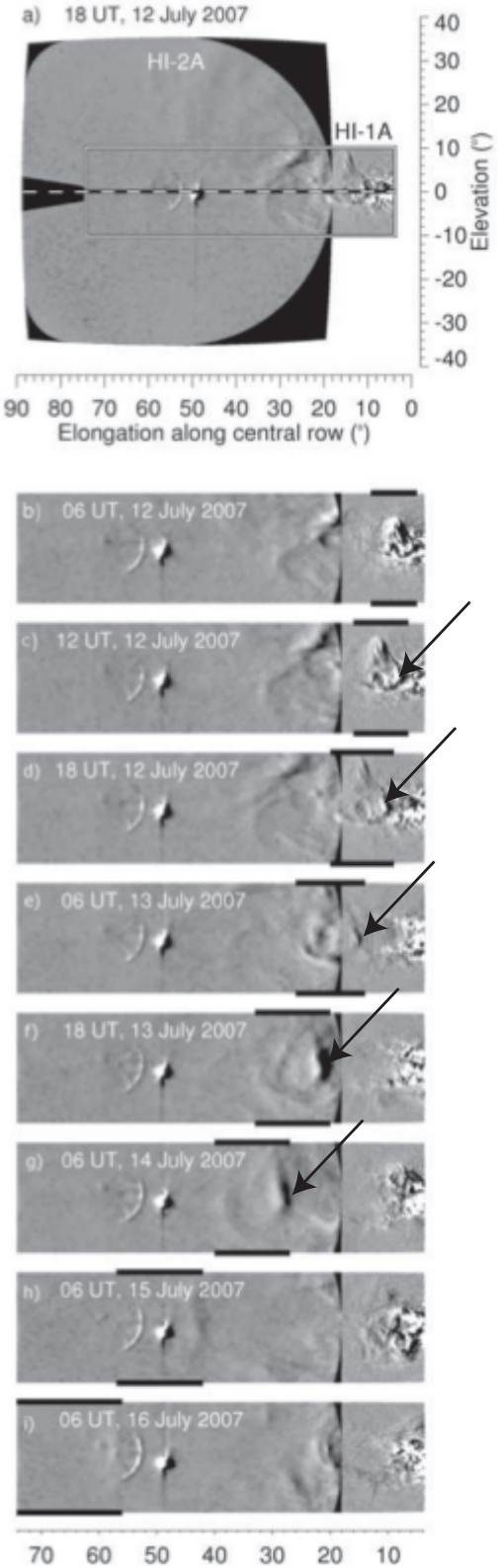

Figure 2.8: Modified from Davies *et al.* (2009), showing a) the fields of view of the HI on STEREO-A and b) a time series highlighting a moving density enhancement in the solar wind. Venus can be seen in each panel at an elongation of about 50°. The Sun is off to the right at an elongation of 0 and the Earth is to the left, beyond 70°. The enhancement is clearly visible in 5 of the panels, and has been pointed out with a black arrow.

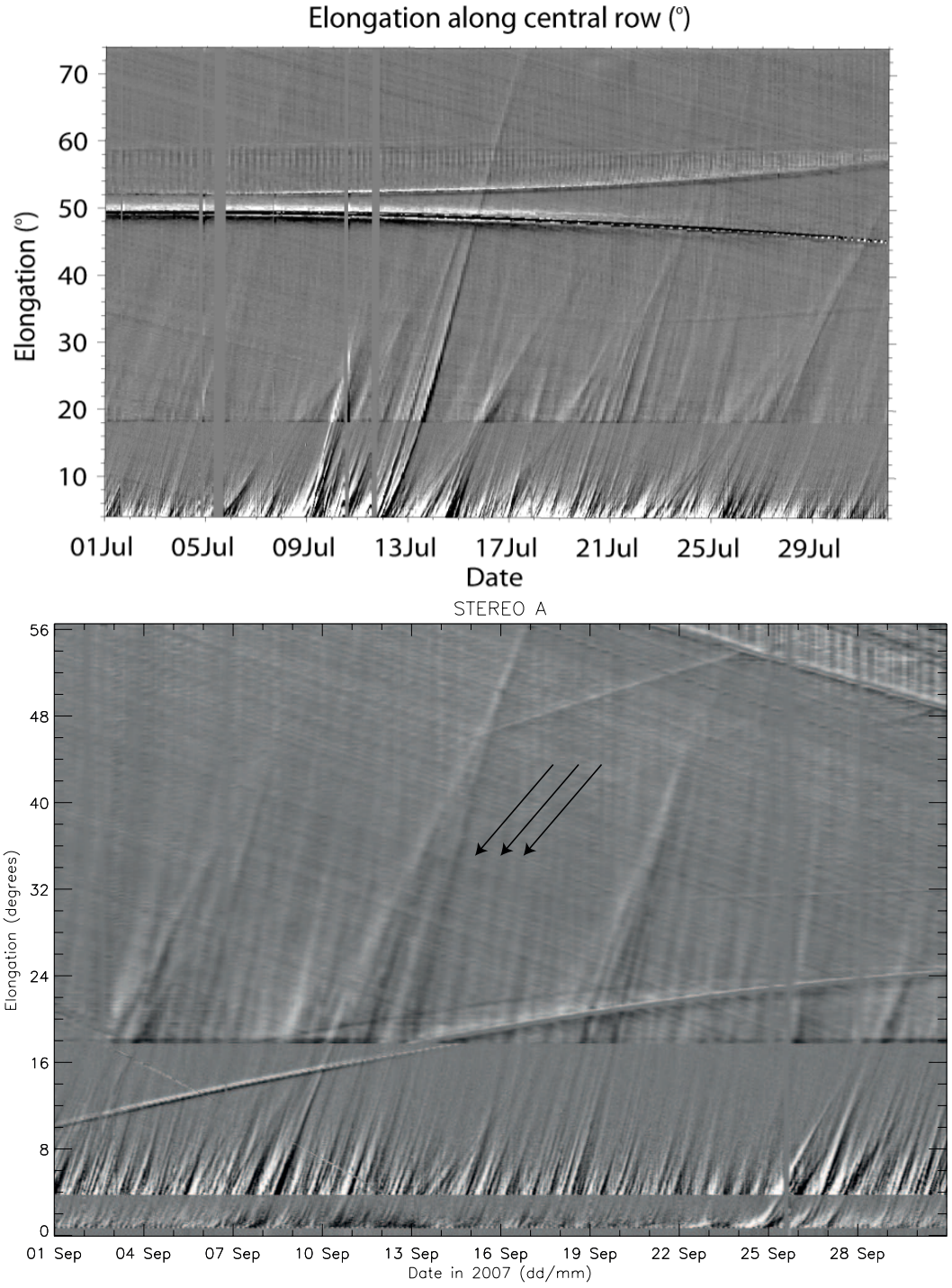

Figure 2.9: A pair of example J-maps. The top panel from Williams *et al.* (2009), shows an example in which can be seen planetary traces moving almost horizontally across the plot at an elongation of about 50°. A variety of traces can be seen moving anti-sunward across the plot, with one particular example initiated on about 12 July. These single bright traces are typical of CMEs. In the bottom panel can be seen an example in which there are some distinct families of traces, three in particular. These families are more indicative of CIRs. Three of the individual transients that comprise the middle family have been indicated with arrows.

stereoscopic spacecraft measurements (Liu *et al.*, 2010; Lugaz, 2010), however as reliable observations from each spacecraft are not always possible, I discuss their application to single-spacecraft observations solely. The different techniques assume that they are observing features with different underlying geometries and behaviours and so not all are equally applicable to all solar wind transients.

2.5.1 Point P technique (PP)

Originally designed to track transients seen by the Solar Mass Ejection Imager (SMEI) instrument aboard the Coriolis spacecraft, the Point P approximation is the simplest of the techniques discussed here. The geometry to be considered is shown in Fig. 2.10 (Kahler and Webb, 2007), observations are assumed to be made at the Earth and P is the point on the transient at which the spacecraft measurements are made. We assume that the material observed is that which has the greatest column density along a sun-centred spherical front or shell, i.e. when the scattering angle will be 90°. From this,

$$r(P) = \sin \varepsilon. \tag{2.6}$$

This is the point-P approximation and allows for a simplified, convenient conversion from elongation angle (ε) to distance of the transient from the Sun.

This technique will work reasonably well for a wide ($\geq 100°$) CME, but will fail for a more narrow feature as the column density will be low. If the observed feature is more compact, then if it is observed at point A or B, the method will attribute it a smaller radial distance from the Sun (still assuming it lies on the same curved surface as P) than it actually has. Thus, this technique is an oversimplification and the point P approximation can be regarded as a lower limit estimate of the distance of the transient from the Sun (Howard *et al.*, 2006). The main advantage of this technique over the others presented here is its simplicity, though it has now generally fallen out of favour and the other techniques are more commonly used.

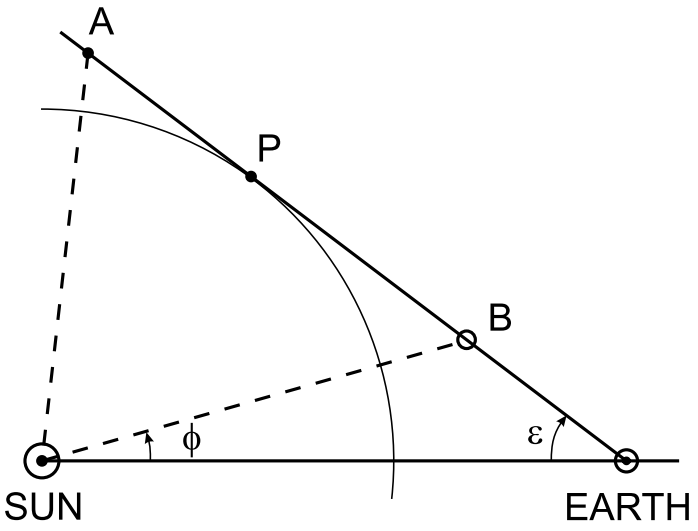

Figure 2.10: Taken from Kahler and Webb (2007), this figure shows the geometry assumed when using the point P approximation. The location of the observer in this diagram is assumed to be the Earth and P is the point on the transient at which the spacecraft measurements are made.

2.5.2 Fixed-ϕ fitting (FPF)

Designed as a technique to deal with single point-like elements of plasma ("blobs") moving away from the Sun (Rouillard *et al.*, 2008), we can see in Fig. 2.11 (Conlon *et al.*, 2014) the geometry for fixed-ϕ fitting as applied to the STEREO mission. For a given plasma element (P) moving out from the Sun (S) at a constant radial speed V_{r}, then the sine rule can be applied to either of the triangles SAP or SBP, in general yielding Eq. 2.7

$$\epsilon(t) = \arctan\left(\frac{V_{\mathrm{r}} t \sin\phi}{r_{SC}(t) - V_{\mathrm{r}} t \cos\phi}\right), \tag{2.7}$$

where r_{SC} is the orbital distance of the observing spacecraft from the Sun, and although written here as a time dependent variable, this value is usually close to constant for a given spacecraft.

The fixed-ϕ assumption then states that the angle ϕ is a constant over the travel time of the solar wind transient plasma element. Observations indicate that whereas a CME front is often expanded across a large area, the observed CIR structure appears to be formed of many small features, each of which is approximately point-

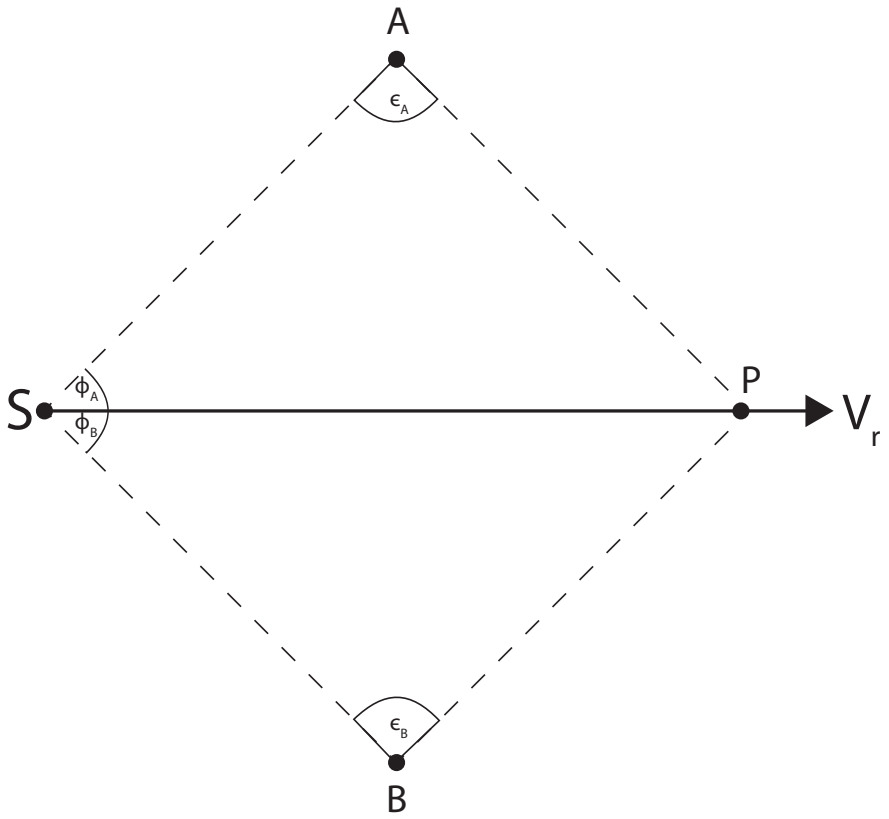

Figure 2.11: From Conlon *et al.* (2014), showing the viewing geometry for the fixed-ϕ fitting technique. ϕ_{A} and ϕ_{B} are the angles between the Sun-plamsa line and STEREO-A and B respectively and ϵ_{A} and ϵ_{B} the elongation angles for STEREO-A and B respectively.

like, that then in turn propagate out from the Sun. As this technique assumes that P is point-like, it is more suitable for CIRs than for CMEs.

2.5.3 Harmonic mean fitting (HMF)

A development of the fixed-ϕ technique, harmonic mean fitting assumes that the feature is more extended in cross section, indeed that it forms an expanding circle fixed on the sun-centre. Fig. 2.12a) (Davies *et al.*, 2012) illustrates the viewing geometries of both the fixed-ϕ and harmonic mean fitting techniques. It is assumed that the leading edge of the feature observed in a J-map is the tangent to the circle. When the line-of-sight is projected onto the direction of motion (Sun-P line), it leads to a misrepresentation of the actual position of the feature along the Sun-P line (hollow points). The harmonic mean technique compensates for this misrepresentation by finding the intersection of the circle with the Sun-P line (filled points). Then, we find that $\epsilon(t)$ can be expressed in the form

$$\epsilon(t) = \arccos\left(\frac{-b + a\sqrt{a^2 + b^2 - 1}}{a^2 + b^2}\right) \tag{2.8}$$

with a and b defined as

$$a = 2\mathrm{r_{sc}(t)}V_{\mathrm{r}}t - \cos\phi \tag{2.9}$$

and

$$b = \sin\phi \tag{2.10}$$

which were first written down in the form presented here by Möstl *et al.* (2011) after Lugaz *et al.* (2009). These expressions represent the harmonic mean of the point P technique and fixed-ϕ techniques, hence the name and like its predecessors, still assumes that the velocity of the observed transient is constant and radial to make the problem tractable.

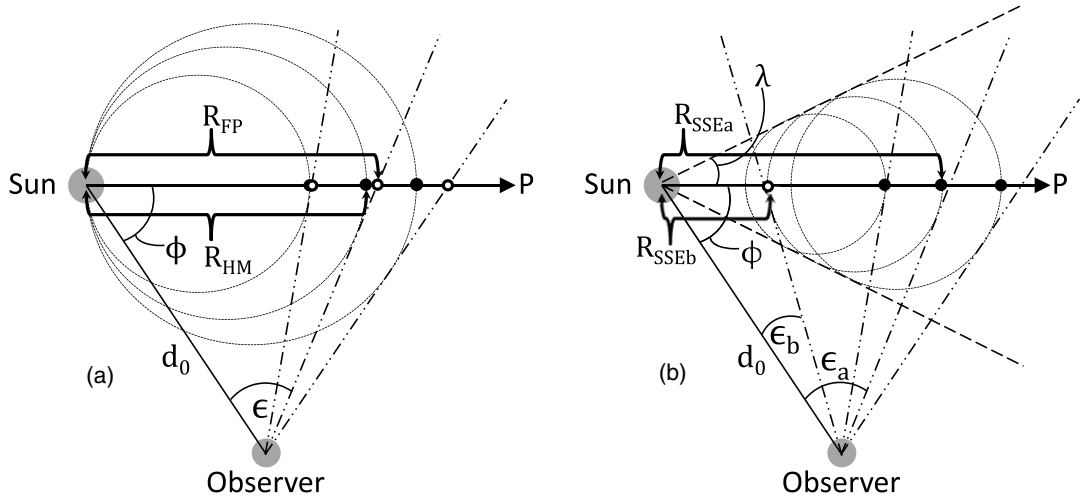

Figure 2.12: Showing a) the geometry of the fixed-ϕ and harmonic mean techniques, and b) The self-similar expansion technique.

2.5.4 Self-similar expansion fitting (SSEF)

Davies *et al.* (2012) found that the fixed-ϕ and harmonic mean techniques are two extremes of a common geometry. They use a more generalised HMF-like analysis in which the circular front is not fixed to the Sun, that they call Self Similar Expansion (SSE) and in common with other techniques, this has been applied to stereoscopic observations (Davies *et al.*, 2013). Fig. 2.12b) shows the viewing geometry for SSE. From this, the relevant expressions are then

$$\epsilon(t) = \arccos\left(\frac{-bc + a\sqrt{a^2 + b^2 - c^2}}{a^2 + b^2}\right) \tag{2.11}$$

with a and b given by

$$a = \frac{2d_0(1+c)}{Vt} - b = \sin\phi \tag{2.12}$$

$$b = \sin\phi \tag{2.13}$$

and

$$c = \pm\sin\lambda. \tag{2.14}$$

The term λ corresponds to the angular half-width of the transient in the plane, or can also be thought of as a parameter relating to the curvature of the transient's front. When λ is set to 0, FPF is regained and when λ is set to 90°(or $\pi/2$ radians), then HMF is recovered. This technique of course adds in additional uncertainty in

the form of an extra variable that one must fit. Looking at Fig. 2.13, taken from Davies *et al.* (2012), we can see that the top panel compares FP with HM traces for the same ϕ value (assumed constant). In the bottom panel, are the corresponding SSE traces, plotted for a variety of different λ values, showing that FPF and HMF form the limiting cases of SSEF.

Of the techniques discussed here, each has its own place in the analysis of solar wind transients observed using white light coronagraphs/heliospheric imagers. The point P technique is the simplest of those discussed and although it has been surpassed in many ways by the other techniques, it does still have a use. If one is confident that an event can be reliably fitted with the technique (i.e. $\geq 100^{\circ}$ wide) then as it is the simplest of the techniques it might be able to provide more reliable results. Because this technique provides a direct, analytical relationship between distance and elongation, it is not necessary to perform fitting to the data. Instead, elongation values can just be extracted directly and propagation characteristics analytically calculated. At the other extreme, self-similar expansion is the most general of the techniques discussed here and so also the most powerful, making the fewest assumptions regarding the observed solar wind transient, however the cost of this is the addition of another parameter to be fitted, leading to potential uncertainties. If the likely structure of the observed transient (point-like or more expanded) is known then either FPF or HMF can be used, but for a general transient, self-similar expansion provides a better solution. It might be that with more time, SSE is increasingly used and the other techniques are found to offer little besides, but for now these last three techniques are all used.

2.6 CME propagation speed

The Parker (1958) solution to the solar wind showed that its propagation speed will vary as a function of time. Despite the assumptions made by the techniques previously discussed, solar wind transients will also not have a constant propagation speed and there have been some studies that consider this.

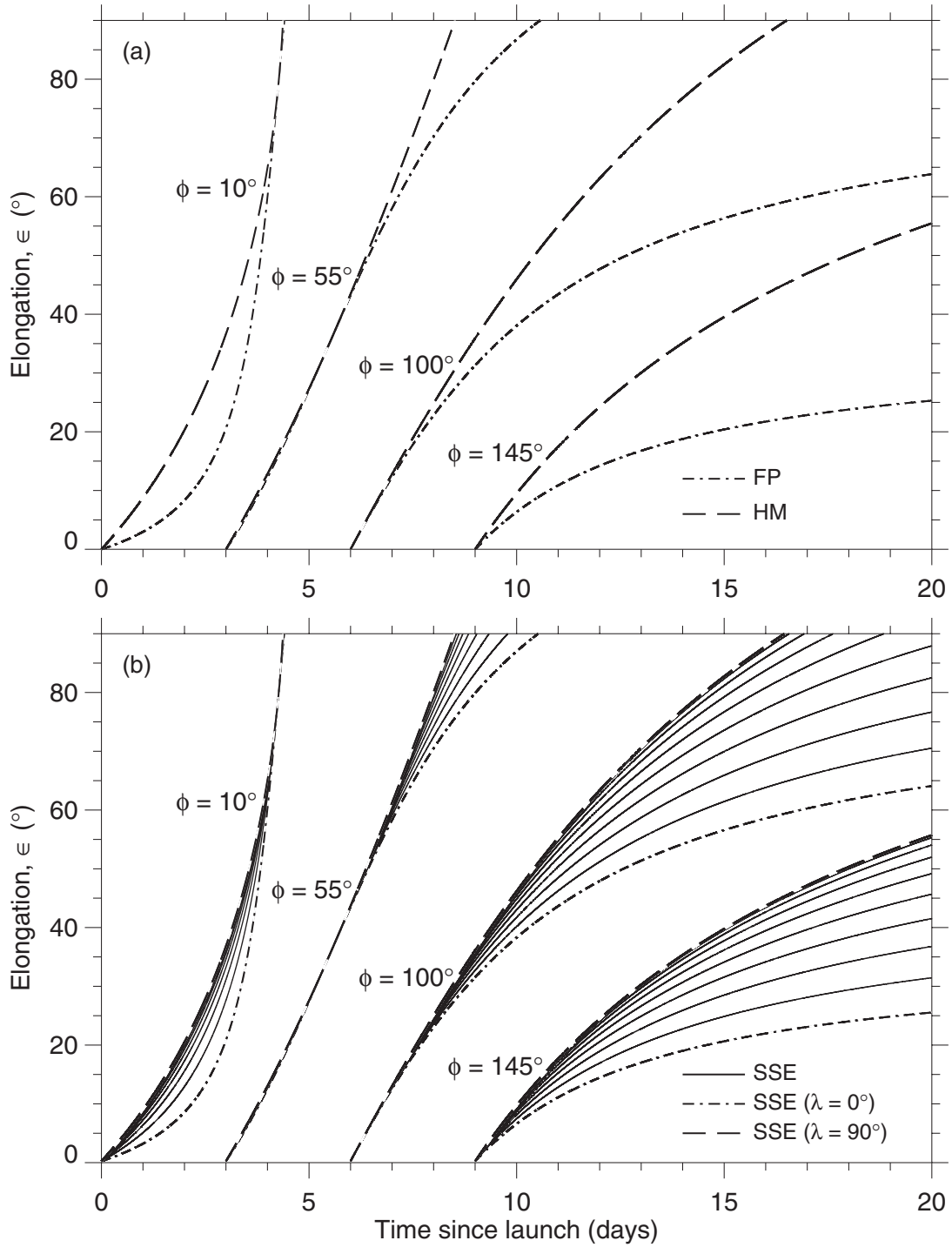

Figure 2.13: The top panel shows FP and HM traces as plotted for a variety of differing ϕ values. The bottom panel shows the corresponding SSE traces, demonstrating that FPF and HMF are the limiting cases of SSEF.

Joshi and Srivastava (2011) use a three-dimensional (3D) reconstruction technique on images from the STEREO COR1, COR2 and EUV instruments to identify and analyse the motion of CMEs close to the Sun. Using a 3D reconstruction allowed them to extract accurate measures of the velocity and acceleration of the observed features. Of the 6 CMEs they observed, all save one had experienced all significant acceleration within 4 $R_{\odot}$, indicating that CMEs generally only accelerate for a short period time close to the Sun. This of course does not consider any acceleration from sources other than the initial acceleration close to the Sun, such as drag between the CME and ambient solar wind, which is discussed below.

Lugaz and Kintner (2013) considered the effect of drag on CMEs as they propagate through the heliosphere. As a CME propagates, then it will be travelling faster than the ambient solar wind through which it passes and so there is the potential that drag exerted on the CME by the solar wind will significantly slow it down. They used a simple drag model to analytically construct time-elongation profiles which were then fitted using both the FP and HM techniques outlined above. They found that as the CME propagates, its speed approaches that of the ambient solar wind, which was to be expected, but they found that the errors introduced to estimated propagation parameters derived from fitting assuming constant propagation speed can be large indeed, potentially reaching angular (ϕ) errors of 10–20° and speed errors of hundreds or perhaps even thousands of km s^{-1}. These values are assuming propagation out to 1 AU and clearly the errors could be even larger further out into the heliosphere. They also found that contrary to expectations, the FP technique actually produces more reliable results for a wide and decelerating feature as the neglect of two different sources of error (the width of the CME and its deceleration) cancel each other to some degree.

This short discussion shows that the assumption made by the above techniques of constant propagation speed out to 1 AU is demonstrably wrong by a significant amount when considering CMEs. It is possible therefore that it might also be flawed when considering solar wind transients associated with CIRs.

2.7 Conclusion

In this section I have looked at two particular types of solar wind transient, CMEs and CIRs and discussed their formation mechanisms and impacts on planetary magnetospheres. As it underpins all of the white light observations of solar wind transients, I have briefly outlined some of the theory relating to Thomson scattering in the context of heliospheric imaging and tried to highlight some of the aspects of that process that are sometimes overlooked but that impact on the visibility of density features in the solar wind. I have talked about various fitting techniques and methods of extracting propagation information from coronagraphs and heliospheric imagers from point P and harmonic mean (both more relevant to CMEs) to fixed-ϕ (more relevant to CIRs) and SSEF (the most powerful of all of them and capable of providing information about any type of transient at the cost of an additional fitting parameter). The observable variation in CME propagation speed as a function of distance from the Sun has also been considered and it has been highlighted that this opens up a similar discussion with respect to solar wind transients associated with CIRs. This description of the current literature on the subject of white light observations of solar wind transients will be referred back to in the coming chapters.

Chapter 3

Instrumentation

3.1 Introduction

In this section I detail both the Solar TErestrial RElations Observatory (STEREO) and Advanced Composition Explorer (ACE) and the instruments onboard each spacecraft. As they are the main instruments used throughout this thesis, I shall pay particular attention to the Heliospheric Imagers (HI) aboard the STEREO spacecraft.

3.2 STEREO

Launched in 2006, NASA's STEREO mission has a series of broad aims set out by Kaiser *et al.* (2007):

1. Understand the causes and mechanisms of CME initiation
2. Characterise the propagation of CMEs through the heliosphere
3. Discover the mechanisms and sites of solar energetic particle acceleration in the low corona and interplanetary medium

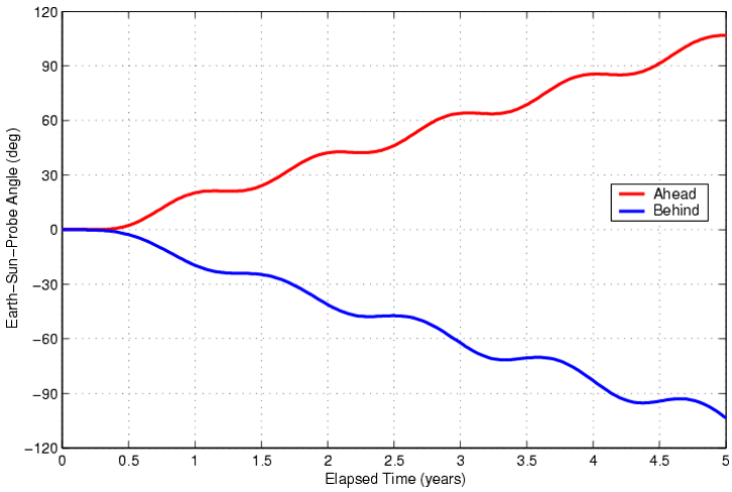

Figure 3.1: Showing how the angle between the Sun-spacecraft line and Sun-Earth line changes over time for the two STEREO spacecraft.

4. Develop a 3-D time-dependent model of the magnetic topology and temperature, density and velocity structure of the ambient solar wind.

It consists of two spacecraft, each in Earth-like heliocentric orbits lying roughly in the ecliptic plane. One spacecraft orbits ahead of the Earth (STEREO Ahead, or STEREO-A) and the other behind the Earth (STEREO Behind, or STEREO-B). Each spacecraft separates from the Sun-Earth line by approximately 22.5° per year, though the angular acceleration does not increase linearly due to the eccentricity of Earth and the spacecraft orbits, which can be seen in Fig. 3.1 (Driesman *et al.*, 2007). In order for the two spacecraft to occupy orbits that gradually separate from the Sun-Earth line, they must be at different orbital distances from the Sun. During the course of the science mission, the STEREO-A orbital distance varies between 0.95–0.97 AU. For STEREO-B, the range of orbital distances is larger, being 1.00–1.09 AU. For more details of the spacecraft orbits see Driesman *et al.* (2007).

3.2.1 Scientific packages

The STEREO spacecraft each carry four instrument packages comprising a total of 18 instruments per spacecraft. The Sun Earth Connection and Heliospheric Investigation (SECCHI) provides the mission's remote sensing capabilities,

Table 3.1: The STEREO instrument packages.

Instrument	Acronym	Purpose
SECCHI	COR1	Coronagraph 1.4–4.0 $R_\odot$
	COR2	Coronagraph 2–15 $R_\odot$
	EUV1	Extreme ultraviolet imager
	HI-1/2	Heliospheric imager 12–215 $R_\odot$
IMPACT	SWEA	Solar wind electrons to 3 keV
	STE	Suprathermal electrons 2–100 keV
	SEPT	Electrons 20–400 keV; protons 60–7000 keV
	SIT	Composition HE–FE 300–2000 keV/nucleon
	LET	Protons, He, heavy ions to 40 MeV/nucleon
	HET	Protons, He to 100 MeV; electrons to 8 MeV
	MAG	Vector magnetic field to 65536 nT
PLASTIC	SWS	Protons, alpha distribution functions to 100keV Heavy ions to 100 keV
	WAP	Wide angle heavy ions to 100 keV
S/WAVES	HFR	Electric field 125 kHz–16 MHz
	LFR	Electric field 2.5–160 kHz
	FFR	Fixed frequency 32 or 34 MHz
	TDS	Time domain to 250 k samples/sec

STEREO/WAVES (SWAVES) tracks interplanetary radio bursts, In-situ Measurements of Particles and CME Transients (IMPACT) provides plasma characteristics of solar energetic particles and PLAsma and SupraThermal Ion Composition (PLASTIC) provides plasma characteristics of protons, alpha particles and heavy ions and provides key diagnostic information to characterise CMEs from ambient coronal plasma. Table 3.1 from Kaiser *et al.* (2007) gives a summary of each of the instrument packages.

Although the STEREO spacecraft has four instrument packages, only three of them are used in this thesis, SECCHI, IMPACT and PLASTIC. The aspects of each of these that are relevant to this work will now be discussed in more detail.

3.2.2 SECCHI

SECCHI provides STEREO's primary remote sensing capabilities. Consisting of 5 instruments (COR1, COR2, EUVI, HI1, HI2) SECCHI observes the solar disc corona and solar wind.

Table 3.2: COR2 performance requirements

Parameter	Units	Ahead	Behind
Field of view (half-angle)	Degrees	4	4
Inner limit of field of view	$R_\odot$	2.5	2.5
Pixel size, full resolution	arcsec	14.7	14.7
RMS spot size (design)	arcsec	15	15
Planned exposure time	sec	<4	<4
Polariser attenuation	-	10^{-4}	10^{-4}
Photometric response	$B_\odot$/DN	1.35×10^{-12}	1.25×10^{-12}
Time to complete pB sequency	sec	11	11
Image sequence cadence	min	15	15

3.2.2.1 COR2

The outer of each STEREO spacecraft's two coronographs, this instrument observes weak coronal light in the visible spectrum. It is an externally occulted Lyot coronograph with a heritage dating back to LASCO C2 and C3 on the SOHO spacecraft (Brueckner *et al.*, 1995). The light observed is white sunlight that has been Thomson scattered from material in the corona. The field of view is larger than C1 (C2 has a field of view of $\approx 16_\odot$) and this is achieved by having a lower stray light level than COR1. The performance requirements of the instrument are set out in Table 3.2.

3.2.2.2 Heliospheric imagers (HI)

Onboard each of the STEREO spacecraft are a pair of heliospheric imagers (HI), labelled HI-1 and HI-2. Much like the coronographs, these observe white sunlight that has been Thomson scattered from coronal material. Both of these cameras are aligned with the ecliptic plane, off-pointed from the Sun by 14°and 53.7° respectively. The two cameras, HI-1 and HI-2 have differing fields of view, with HI-2's being the wider (they are 20° and 70° respectively). There is an Earth-occulter to protect the cameras during the early mission, when it was possible that the Earth could appear within the field of view and a protective door to shield each instrument during the launch phase. The performance specifications of the instruments can be seen in Table 3.3 (Eyles *et al.*, 2008).

Table 3.3: Monimal HI performance specifications. [a]Are measured in the plane of the sky relative to the viewing location. [b]These are actual values optimised during mission operations rather than original specifications.

	HI-1	HI-2
Direction of centre of field of view from Sun Centre	14.0°	53.7°
Angular field of view	20°	70°
Angular range	4°–24°	18.7°–88.7°
	(15 $R_\odot$–90 $R_\odot$)[a]	(70 $R_\odot$ – 330 $R_\odot$)[b]
CCD pixel size	33 arcsec	2 arcmin
Image array (2 × 2 binning)	1024 × 1024	1024 × 1024
Image bin size	70 arcsec	4 arcmin
Spectral bandpass	630–730 nm	400–1000 nm
Exposure time[b]	40 seconds	50 seconds
Exposures per summed image sequence	30	99
Summed image cadence[b]	40 minutes	2 hours
Brightness sensitivity ($B_\odot$ = solar disc)	3×10^{-15} $B_\odot$	3×10^{-16} $B_\odot$
Stray light rejection (outer edge of field)	3×10^{-13} $B_\odot$	10^{-14} $B_\odot$

The HI detectors themselves are CCDs with 2048 × 2048 pixels, which is normally binned as 1024 × 1024 image arrays. It can be seen in Fig. 3.2 that the anticipated intensity of the corona is orders of magnitude greater than that of a CME. To obtain a sufficient statistical accuracy, a long exposure time is needed, however if this were done then cosmic rays would become a problem and would saturate the image. Instead, a selection of shorter exposure images are taken, which are then individually scrubbed for cosmic rays and summed to form a single, longer exposure image. For HI-1, 30 separate exposures are used to form a single image with an exposure time of 40 minutes, and for HI-2, 99 exposures are used for an exposure time of 2 hours. The field of view of each of the instruments are shown in Fig 3.3 (Eyles *et al.*, 2008). In this figure, STEREO A is at a distance of 0.96 AU from the Sun and STEREO B at 1.09 AU from the Sun.

Before the HI images are ready for serious scientific use, they go through significant image processing to:

- Remove the cosmic ray scrubbing values
- Identify saturated columns and missing data blocks
- Apply the correction for shutterless readout to the image

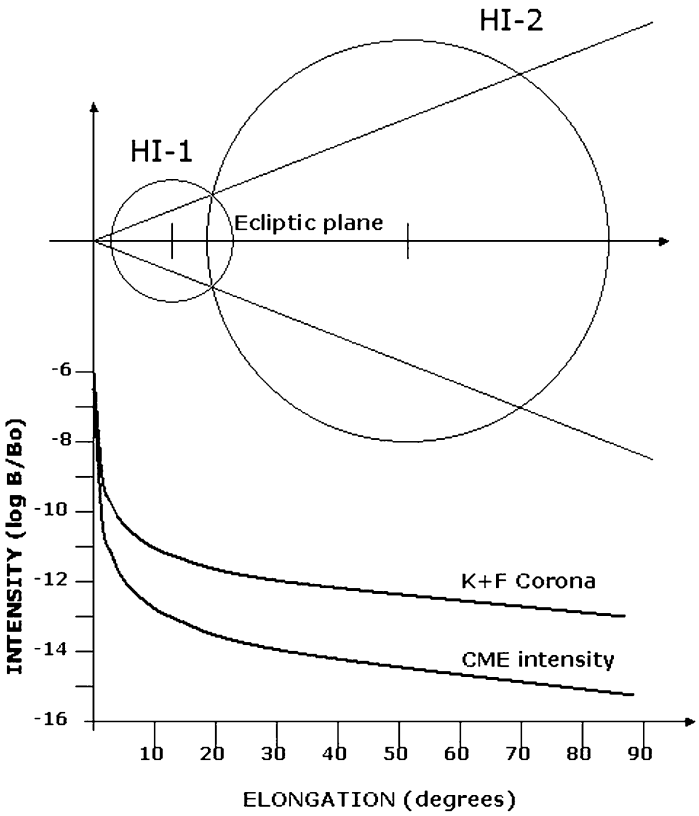

Figure 3.2: Taken from Eyles *et al.* (2008), this diagram is adapted from Socker *et al.* (2000) and based on calculations by Koutchmy and Lamy (1985), showing the fields of view of the two HI instruments, along with the expected intensities of the corona and CMEs. This illustrated that the corona will have an intensity orders of magnitude greater than a CME and so in order to observe the latter long exposure times are required.

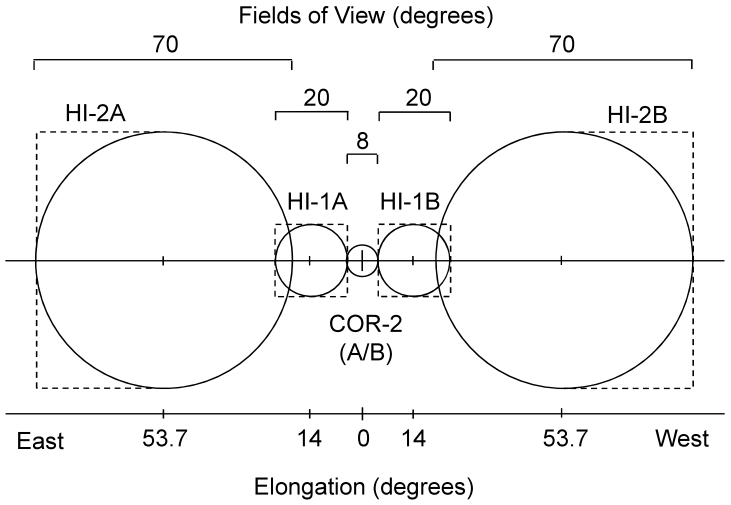

(a)

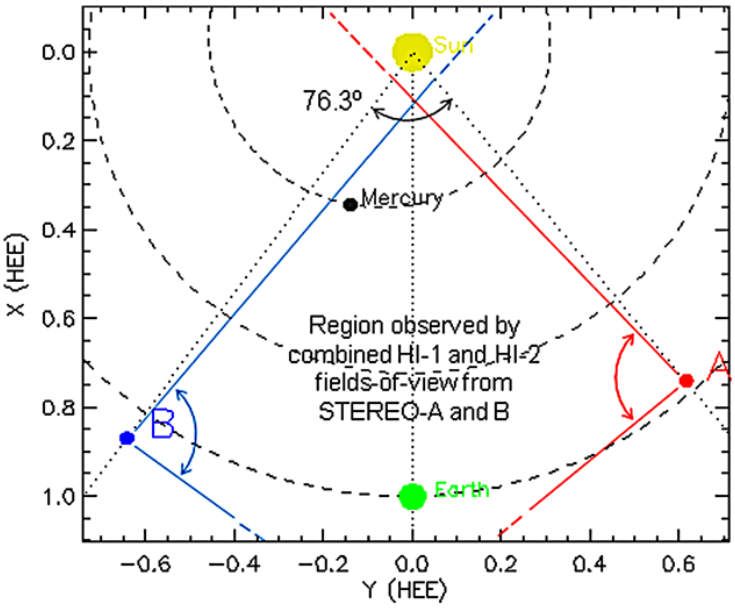

(b)

Figure 3.3: Taken from Eyles *et al.* (2008), a) shows the fields of view of the COR2 and HI instruments. The dotted lines correspond to the square format of the CCDs, although due to optical vignetting, the response in the corners of the square is somewhat limited. The Sun-centred coronagraphs view all latitudes, however the HI fields of view are limited to ±35° perpendicular to the ecliptic. b) shows a projection onto the ecliptic plane of the HI fields of view as of 01/10/2008 in heliocentric Earth ecliptic coordinates (HEE), also showing the positions of each of the inner solar system planets, though Venus does not lie within the plot space.

- Apply a flat-field correction to the image
- Correct the pointing and optics parameter values in the headers.

each of which is described in more detail below.

Each of the shorter exposure images used to form the long exposure images used by HI has to be scrubbed for cosmic rays. In order to scrub an image of cosmic rays, each image is compared with the previous image on a pixel by pixel basis. If the intensity in a given pixel exceeds a given threshold, then that intensity value for that pixel is removed and replaced with the corresponding value from the previous image. In this way, anomalous values that would be associated with cosmic rays are removed.

When the signal from a bright object (for example a planet) exceeds the full well capacity of a pixel, excess charge bleeds into adjacent pixels in the same columns, in turn leading to vertical columns of saturated pixels. Generally speaking, charge bleed in the horizontal direction is inhibited, although it can occur in extreme circumstances. The shutterless correction cannot be applied if there is saturation anywhere in the column and as such if there is pixel bleeding anywhere in a column then the entire column has to be considered invalid data and replaced. Adjacent pixel values are used as the replacement.

The HI cameras do not have shutters, meaning that the CCDs remain exposed to the sky during the image readout process and clear process prior to each subsequent image. As the readout time is not insignificant compared with the typical exposure time, image smearing during readout can occur, hence the shutterless correction to account for this.

There are a number of reasons why the actual response from the sensors might deviate from the uniform response one might expect and hence that there might be another correction required. There can be variations in the efficiency of the optics across the field of view due to changes in transmission of the optical elements and coatings, geometrical aperture effects and vignetting (reduction of image brightness

at the edge of the image compared with that at the centre). Each of these effects normally cause large scale variations which were accounted for to a certain extent before the spacecraft were launched. The condensing of volatile materials on the CCD can cause additional large scale effects. There are also smaller scale variations. CCDs often show pixel-to-pixel variations in response, of the order of a few percent. These contribute to small scale effects. These factors all lead to a need for a correction to account for them.

Following these steps, there is background subtraction to remove the brighter F-corona .This is done by taking running-differences of the images, or alternativey by subtracting the intensity of the lowest intensity pixel from the image. This is only possible provided that the background is fairly constant for a few days, which is normally the case. After this, there is still the stellar background. There are algorithms to remove the stellar field which do have some success, though traces of the stellar background are still visible in the processed images.

The attitude determination for the SECCHI instruments are ascertained from the stellar background on an image by image basis for all cameras. This has been done since 2008 and has improved the attitude determination of the cameras.

3.2.3 IMPACT magnetometer experiment

Designed to produce multi-point measurements of solar wind and suprathermal electrons, this package consists of 7 in-situ sensors and a magnetometer on a boom designed to meet the STEREO mission goal of understanding CME 3-D structure. It is the magnetometer (MAG) that is of interest to the work here. This uses a conventional three-axis flux gate design, used on many missions (Acuña *et al.*, 2008) and has a sampling rate of 32 samples s^{-1} and an active range of $\pm$ 65536 nT. This wide range means that the instrument can be operated during all phases of the mission. The instrument itself is kept 3m away from the body of the spacecraft on a 4m boom that also houses other instruments. This ensures that any interference from the spacecraft are minimised.

Data from this instrument are used in chapter 6.

3.2.4 PLASTIC

Designed to study the in-situ bulk properties of solar wind protons and the composition and properties of solar wind minor ions, the PLASTIC package (Galvin *et al.*, 2008) consists of two instruments. Composition information of the solar wind can form a 'DNA sample' of its origins which survives even when solar wind kinetic properties have been significantly altered (by a CIR for example). When combined with STEREO's other instrument packages, it is possible to relate variations in solar wind properties, including composition, with their relevant temporal variations observed in the chromosphere and corona. The mission also allows for remote sensing of CMEs and then in-situ measurements of the same feature's properties. It is finally worth noting that the STEREO mission (via IMPACT and PLASTIC) provides a test of the ability to use in-situ experiments at solar longitudes different from that of the Earth to issue real-time space weather warnings.

3.3 ACE

Launched in 1997, the Advanced Composition Explorer (ACE) spacecraft sits in an orbit around the L1 point, allowing it to measure the solar wind shortly (typically 30–60 minutes) before it reaches the Earth. The spacecraft itself is spin stabilised, rotating at 5 rpm, with its spin axis generally aligned with the spacecraft-Sun line. It was designed to take advantage of advances in space instrumentation to determine the elemental, isotopic and ionic charge-state composition of samples of matter with far greater precision than had previously been possible and hence make comparative studies of the origin and evolution of the different types of matter it encounters. As particle acceleration is ubiquitous throughout the solar system and beyond, ACE was tasked with measuring these accelerating particles to further our understanding of particle populations that come from both within our solar system and outside of

it. The overall science aims of the mission were to investigate:

1. Accurate and comprehensive determination of the elemental and isotopic composition of matter collected
2. Origin of the elements and subsequent evolutionary processing
3. Formation of the solar corona and acceleration of the solar wind
4. Particle acceleration and transport in nature.

In keeping with NASA's thoughts at the time, ACE was designed to be cheap and reliable, and as such the spacecraft system heritage was derived from 6 previous missions and the failure of any one of the scientific payloads would not critically impact upon the spacecraft's ability to perform its role.

3.3.1 Instruments

The different particle populations that ACE is intended to measure cover a very wide energy range and as such there is a variety of instruments to give coverage. The use of multiple, previously tested, instruments with overlapping energy ranges also introduced redundancy. Data from two of the instruments were used in this work.

The Solar Wind Electron, Proton and Alpha Monitor (SWEPAM) measures the three-dimensional characteristics of solar wind and suprathermal electrons in the range 1–900 eV and ions in the range 0.260–35 KeV. It consists of modified versions of the spare solar wind electron and ion sensors from Ulysses. MAG is a twin triaxial flux-gate MAGnetometer that measures the vector magnetic field. It is the flight spare from the magnetometer flown on WIND.

For more information about the ACE mission, see Stone *et al.* (1998) and Chiu *et al.* (1998) and references therein.

3.4 Conclusion

In this section we have discussed the variety of instruments that can measure solar wind transients as they propagate out from the Sun into the heliosphere, both in situ and remotely. Data from HI are used in all chapters barring the first one, and data from PLASTIC, IMPACT and ACE in chapter 6.

Chapter 4

Assessing the effect of spacecraft motion on single-spacecraft solar wind tracking techniques

Excluding section 4.3, the work presented in this chapter has been published in Conlon *et al.* (2014). Section 4.3 along with chapter 5 have been submitted for publication, currently being towards the end of the peer review process.

4.1 Introduction

There are observations of solar wind transients that suggest the techniques used for estimating their propagation characteristics (outlined in chapter 3) are not always reliable. Rouillard *et al.* (2008) for example analyses a pair of CIR-related features and estimates their propagation speeds to be lower than that of the slow solar wind at the time as measured at the ACE spacecraft. There are a number of assumptions that are used when analysing solar wind transients in this manner that could be causing this discrepancy and this chapter considers the Fixed-ϕ Fitting (FPF) and Harmonic Mean Fitting (HMF) techniques and relaxes the assumption that the observing spacecraft remains stationary for the duration of observation of

the solar wind transient. The inaccuracy introduced by this assumption for the two STEREO spacecraft is found to be significant, and can lead to an overestimation of the transient speed as seen from STEREO-A and an underestimation as seen by STEREO-B. This has implications for the prediction of the arrival of solar wind transients at 1 AU and hence is important for the study of space weather.

The FPF, HMF and Self-Similar Expansion Fitting (SSEF) single-spacecraft fitting techniques based on the geometries discussed in the previous chapter permit $V_{\rm r}$ and ϕ to be retrieved from an observed time-elongation profile of a solar wind transient. These techniques assume ϕ and $V_{\rm r}$ are constant over the duration of the feature observed. They also assume that the transient's propagation path is fixed with respect to the sun – spacecraft line during the time for which it is observed, however, this will not be true even if the transient does not deflect away from radial propagation during its travel because the spacecraft themselves are moving in the inertial frame. If we initially consider that the STEREO spacecraft orbit approximately with the Earth, this means that they rotate about the Sun with a period of 1 year. If a transient has a speed of some 300 km s^{-1}, then during the 6 day travel time of the transient to 1 AU the spacecraft will have moved almost 6° around its orbit. If we consider specifically the situation in the ecliptic plane, the sense of the orbital motion is shown by the arrows in Fig. 4.1 and this orbital motion means that ϕ (the angle of propagation of the transient relative to the Sun – spacecraft line, which, in this case, equates to the ecliptic latitude relative to the Sun-spacecraft line) will change with an angular speed of $\frac{360}{365.25}^{\circ}$ day^{-1} during the outward journey of the transient. This can be combined with the smaller effect from the rate at which the STEREO spacecraft separate from the Sun-Earth line, to turn Eq. 4.1 into 4.2 for the fixed-ϕ geometry,

$$\epsilon(t) = \arctan\left(\frac{V_{\rm r} t \sin\phi}{r_{\rm SC}(t) - V_{\rm r} t \cos\phi}\right), \tag{4.1}$$

$$\epsilon(t) = \arctan\left(\frac{V_{\rm r} t \sin\left(\phi_0 \pm \frac{360 \pm 22.5}{n_{\rm y}} t\right)}{r_{\rm sc}(t) - V_{\rm r} \cos\left(\phi_0 \pm \frac{360 \pm 22.5}{n_{\rm y}} t\right)}\right). \tag{4.2}$$

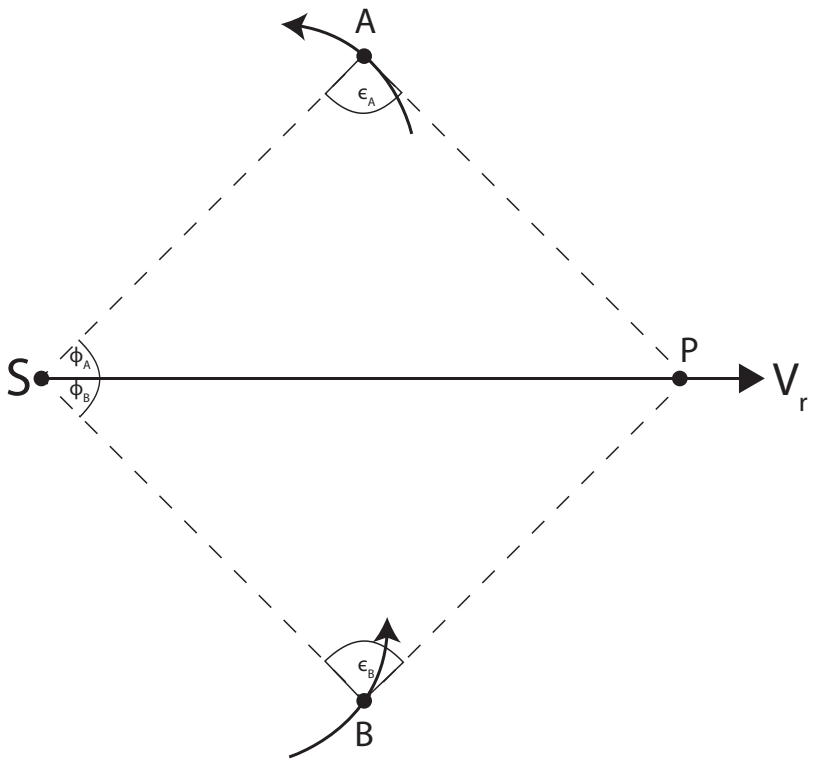

Figure 4.1: The relationship between the locations of STEREO-A and B, the Sun (S) and a plasma blob (P) moving radially with speed V_r. ϕ_A and ϕ_B are the angles between the Spacecraft-Sun line and the direction of propagation of P. ϵ_A and ϵ_B are the elongation angles, the angles at each spacecraft between S and P. The arrows show the sense of motion of STEREO-A and B in their orbit around the Sun.

These expressions are written assuming that t is in seconds, n_y is the number of seconds in a year and ϕ_0 is the ϕ value when $\epsilon = 0$. Where there is a $\pm$, $+$ refers to STEREO-A and $-$ refers to STEREO-B. If we apply the same correction to the harmonic mean model, then we turn Eq. 4.3–4.5 into Eq. 4.6 – 4.8.

$$\epsilon(t) = \arccos\left(\frac{-b + a\sqrt{a^2 + b^2 - 1}}{a^2 + b^2}\right) \tag{4.3}$$

with a and b defined as

$$a = \frac{2r_{sc}(t)}{V_r t} - \cos\phi \tag{4.4}$$

and

$$b = \sin\phi \tag{4.5}$$

$$\epsilon(t) = \arccos\left(\frac{-b + a\sqrt{a^2 + b^2 - 1}}{a^2 + b^2}\right) \tag{4.6}$$

with a and b defined as

$$a = \frac{2r_{\mathrm{sc}}}{V_{\mathrm{r}}t} - \cos\left(\phi_0 \pm \frac{360 \pm 22.5}{n_{\mathrm{y}}}t\right) \tag{4.7}$$

and

$$b = \sin\left(\phi_0 \pm \frac{360 \pm 22.5}{n_{\mathrm{y}}}t\right). \tag{4.8}$$

Similarly for SSE, ϕ is modified in the same way. The correction presented in this section is less easily applied out of the ecliptic, where ϕ is no longer the ecliptic longitude relative to the observer and so Eq. 4.2 and 4.6 – 4.8 are applicable only for transient trajectories in the ecliptic plane, where the spacecraft motion effect is greatest.

The remainder of this chapter assesses the effect of taking spacecraft motion into account when performing fitting, to determine if it makes a significant difference to the values of V_{r} and ϕ retrieved from the fitting. In Fig. 4.2, the top panel shows the effect of taking into account spacecraft motion in simulated ecliptic time-elongation profiles as seen from STEREO-A HI and the bottom panel as seen from STEREO-B HI, for the fixed-ϕ model. The solid lines correspond to a set of simulated profiles computed with ϕ values varying by 10° from one trace to the next with ϕ_{A} running from 90° to 20° in the top panel and ϕ_{B} from 20° to 90° in the bottom panel using Eq. 4.1. The dashed lines correspond to that same trace, but including the orbital motion of the spacecraft (i.e. Eq. 4.2). Fig. 4.3 shows this for the harmonic mean geometry (Eq. 4.3 – 4.5 solid line and Eq. 4.6 – 4.8 dashed line). In each case, the profiles are separated by ≈ 16 hours. These particular traces are for a radial propagation speed of 300 km s^{-1}.

Fig. 4.2 and 4.3 show that including orbital motion of the spacecraft can make an observable difference, up to ≈ 5° of elongation over a transit time of 6 days. It would appear, therefore, that including orbital motion of the spacecraft in the single-spacecraft FPF and HMF techniques could make a significant difference to the

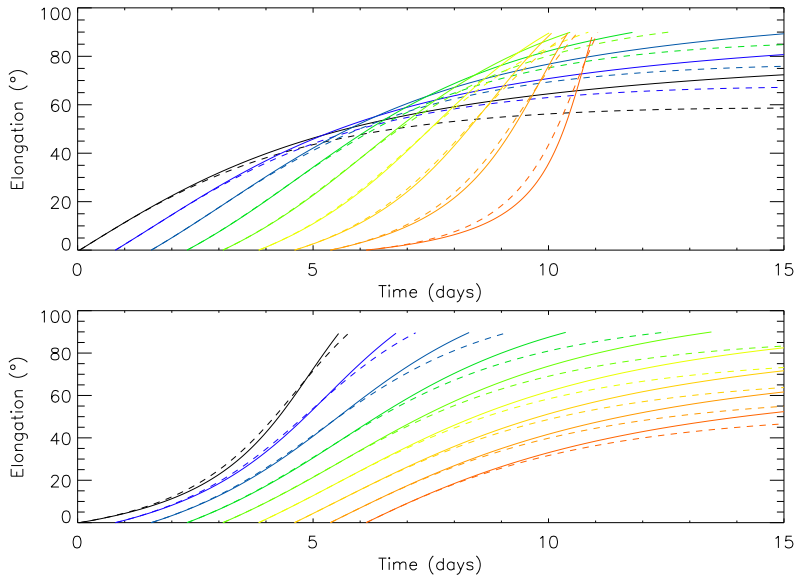

Figure 4.2: Modelled elongation-time profiles for a series of theoretical transients ejected from the Sun at different values of ϕ_0 and assuming FPF. The solid lines assume constant ϕ, dotted traces correct for spacecraft motion. The upper panel is for STEREO-A and the lower panel for STEREO-B. Each successive profile is separated by $\approx$ 16 hours with ϕ varying in the range [20,90] in the top panel and [90,20] in the bottom. In each panel, the plots are made using a radial speed of 300 km s^{-1}. In each case, the colour-coding is simply an aid to separate the different traces and prevent confusion.

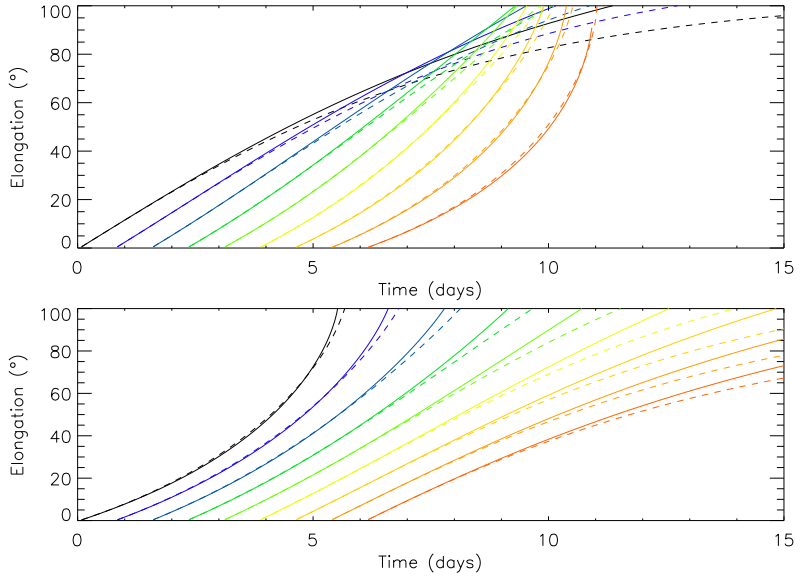

Figure 4.3: Fig. 4.2 but as shown for the harmonic mean fitting technique.

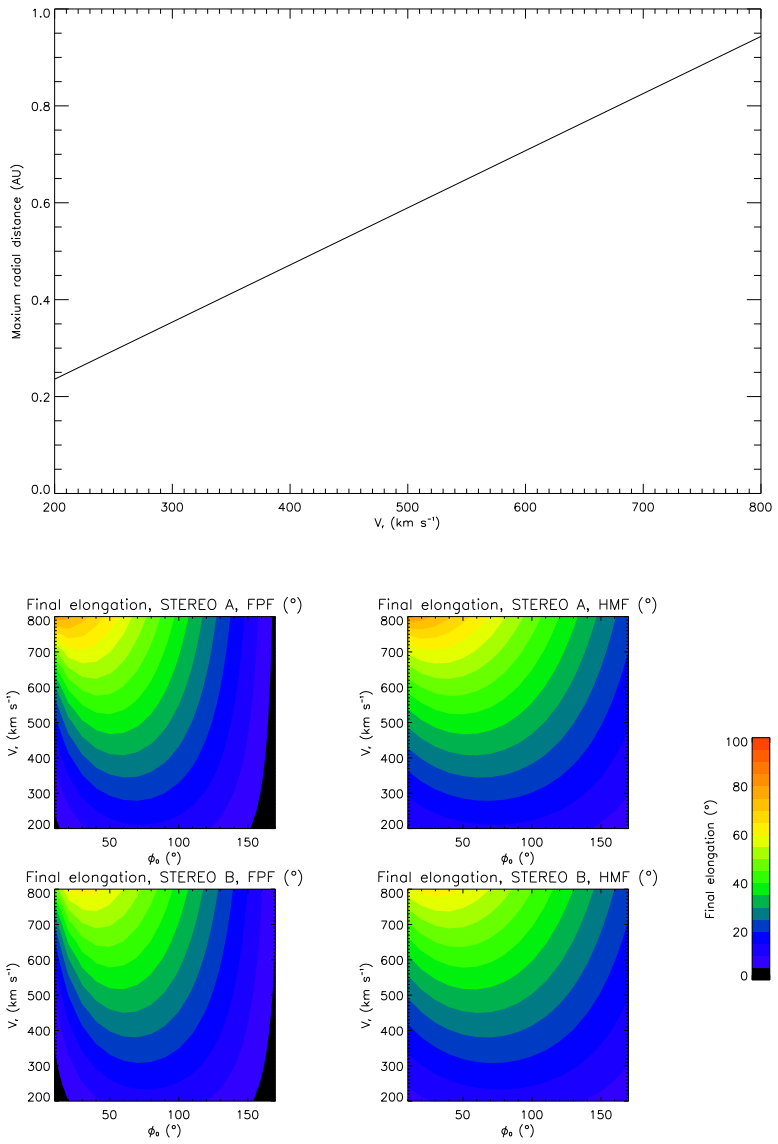

Figure 4.4: The top panel shows the maximum distance reached by simulated traces across the parameter space of the investigation. In the bottom four panels can be seen the final elongation values reached by the traces across the parameter space for STEREO A and FPF (top left), STEREO B and FPF (bottom left), STEREO A and HMF (top right) and STEREO B and HMF (bottom right).

retrieved speed and direction. In the next section the effects on the fitted parameters are evaluated.

4.2 Effect of including spacecraft motion in FPF and HMF

In this section, the difference in the retrieved parameters that is made by including the effects of the orbital motion of the spacecraft is assessed. Time – elongation profiles accounting for spacecraft motion are simulated and then a best-fit to these profiles performed without accounting for spacecraft motion, i.e. using the technique used in previous studies. In this way it should be possible to assess how much difference this effect makes to the fitting. The simulated time-elongation profiles were created using $10^\circ \leq \phi_0 \leq 170^\circ$, 200 km s^{-1} $\leq V_\mathrm{r} \leq$ 800 km s^{-1} in increments of 10° and 50 km s^{-1} respectively and traced out for 50 1 hour time increments. Using a fixed number of time increments ensures that the simulated traces are affected by spacecraft motion for the same length of time and the upper velocity value and the number of time increments were picked to restrict the traces out to radial distances of less than the typical orbital distance of the relevant spacecraft ($\approx$1 AU). Fig. 4.4 shows the final radial distance (top panel) and elongation values (bottom four panels) reached by the simulated traces. In the bottom four panels are the final elongations for STEREO A using FPF (top left panel), STEREO B using FPF (bottom left) STEREO A using HMF (top right) and STEREO B using HMF. For the majority of the parameter space investigated, the final elongation value reached is less than 60°. The fitting method itself is that described by Lugaz (2010), fitting V_r values of 200 – 5000 km s^{-1} in 1 km s^{-1} increments and ϕ of -10 – 190° in 1° increments. The traces were also subsequently fitted to a start time of ± 5 hours of the launch time, i.e. ± 5 hours of the first point of the profile. In Fig. 4.5 are simulated fixed-ϕ (top panel) and HM (bottom panel) time-elongation profiles for STEREO-A assuming that there is 1) no spacecraft motion over the duration of the profile (blue), 2) accounting for spacecraft motion (black) and 3) the best fit based on fitting the uncorrected equation to the corrected trajectory (red). The values noted on each panel ($\phi_0 = 20^\circ$ and $\mathrm{V_r} = 200$ km s^{-1}) are the values used to simulate the curves. An example with a small value of ϕ has been chosen here to show an highlight the possible difference between including and neglecting spacecraft motion. For comparison, the best fitted values are $V_\mathrm{r} = 294$ km s^{-1} and $\phi = 17^\circ$ for fixed-ϕ

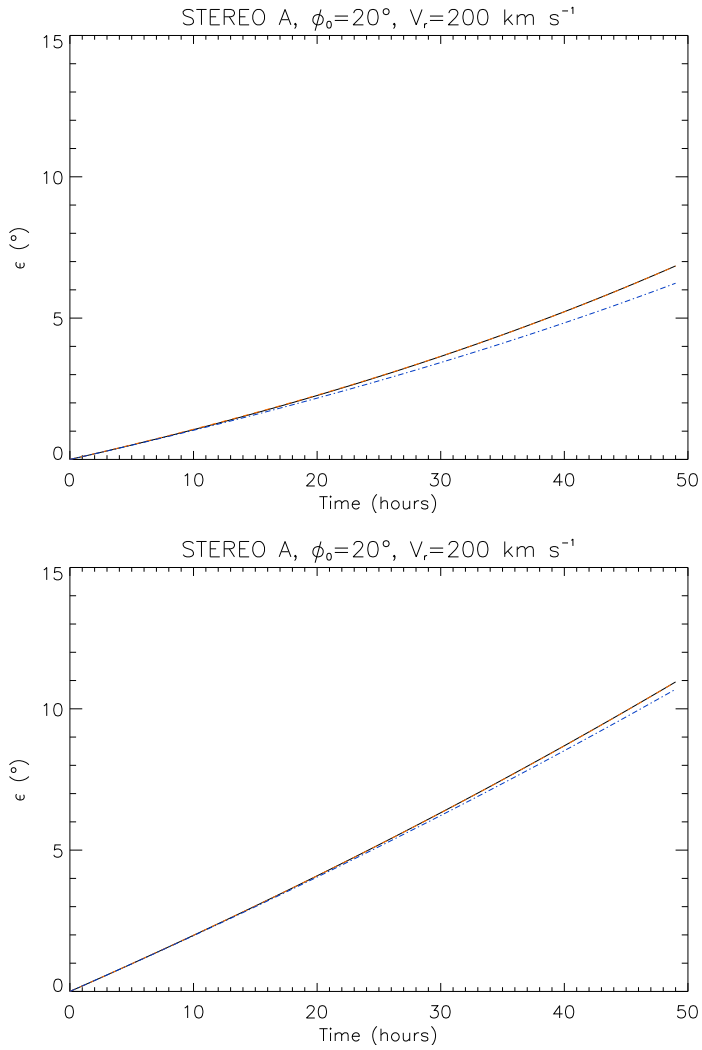

Figure 4.5: Two panels, in each showing a trace created assuming the inclusion of spacecraft motion (black), neglecting spacecraft motion (blue) and the result from a fit that neglects spacecraft motion to data including spacecraft motion (red). This is done for both the fixed-ϕ (top) and harmonic mean (bottom) techniques, and models the traces for 50 1 hour time steps.

fitting and $V_r = 235$ km s^{-1} and $\phi = 8°$ for harmonic mean fitting, $\pm$ 1 km s^{-1} for the V_r and 1° for ϕ. It can be seen in Fig. 4.5 that the fitting process effectively finds a good fit to the corrected profile, even using the uncorrected equation, though the fitted parameters are far from the modelled values.

In Fig. 4.6, there are four contour plots. These show the difference between the input radial speed and the retrieved radial speed, denoted as ΔV_r and the difference between starting modelled ϕ value of a trace (ϕ_0) and the best-fit value (i.e. input ϕ minus retrieved ϕ), using the fixed-ϕ approximation, denoted by $\Delta\phi$. Positive values (red) indicate that the input values are larger and negative values (blue) that the retrieved values are larger.

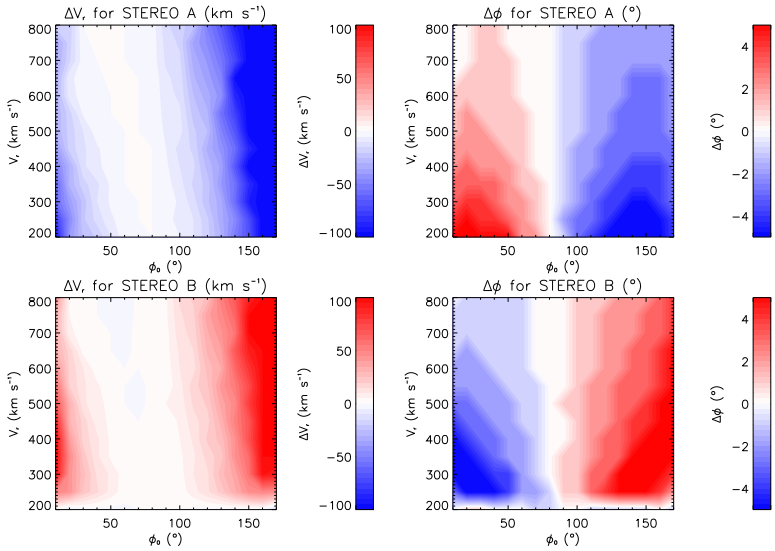

Figure 4.6: Four contour plots showing the difference made by allowing ϕ to vary and then fitting to this using fixed-ϕ fitting. The colour scale saturates at red for larger positive values and blue for larger negative values.

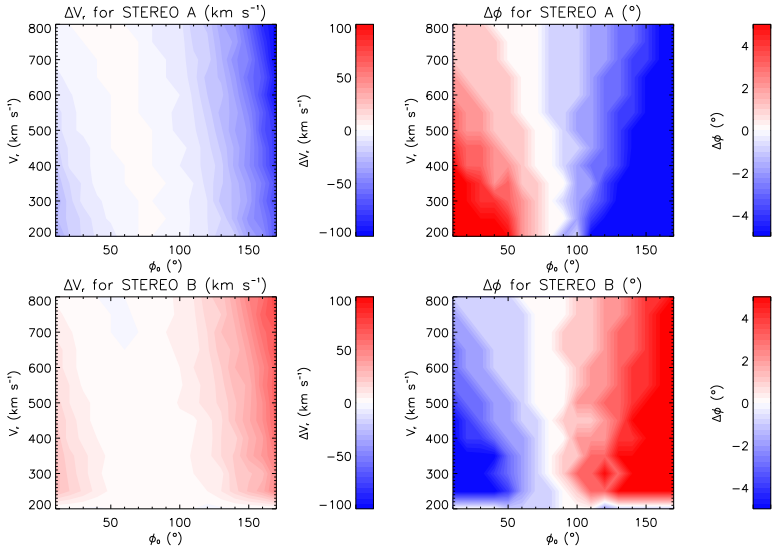

Figure 4.7: Four contour plots showing the difference made by allow ϕ to vary when using harmonic mean fitting. The colour scale saturates at red for larger positive values and blue for larger negative values.

Considering first the speed plot for STEREO-A (the upper-left panel), we can see that the magnitude of $\Delta V_{\rm r}$ has its largest values for extreme values of ϕ_0, being smaller for more moderate values, and indicates that not accounting for spacecraft motion will lead to an overestimation of the radial speed for large and small ϕ. Considering the corresponding plot for STEREO-B, the effect is reversed, with an underestimate in radial speed at small and large angles. So there is similar behaviour seen from each of the STEREO spacecraft, but mirrored, so that when the speed is being underestimated in one spacecraft, it is being overestimated by the other. Typically, $\Delta V_{\rm r}$ is a few tens of km s^{-1}.

Looking now at the right hand two plots, which show the behaviour of $\Delta\phi$ it can be seen that there is an element of symmetry here also. In each case, the magnitude of $\Delta\phi$ is larger for extreme ϕ_0 and smaller radial speeds. Considering the corresponding plot for STEREO B (bottom-right panel) then it can be seen that the sense of $\Delta\phi$ effect is reversed. Overall in most regions of parameter space, $\Delta\phi$ is no larger than a few degrees.

In Fig. 4.7, are similar contour plots for the harmonic mean fitting, with very similar features present as in the previous set of contour plots. Considering each of the plots, however, it can be seen that the size of $\Delta V_{\rm r}$ is larger for fixed-ϕ and that of $\Delta\phi$ is larger for the harmonic mean method.

It is perhaps initially surprising here that $\Delta V_{\rm r}$ keeps the same sense for a given spacecraft and only changes sense between spacecraft. Looking at the top panel of Fig. 4.2 then we can see that by eye we might expect the sense of $\Delta V_{\rm r}$ needed to compensate for the spacecraft motion to be opposite when one considers large vs. small values of ϕ_0 (i.e. positive $\Delta V_{\rm r}$ for one extreme of ϕ_0 and negative for the other). To put forward one possible explanation, let us consider a high ϕ trace seen by STEREO-A, such as that seen in Fig. 4.8. At early times, an overestimate of ϕ leads to an overestimate of $V_{\rm r}$ to compensate and this effect may be enough to offset the effects of spacecraft motion that would otherwise reduce the measured elongation values from what we would expect, an effect that one would expect to lead to an underestimate of $V_{\rm r}$.

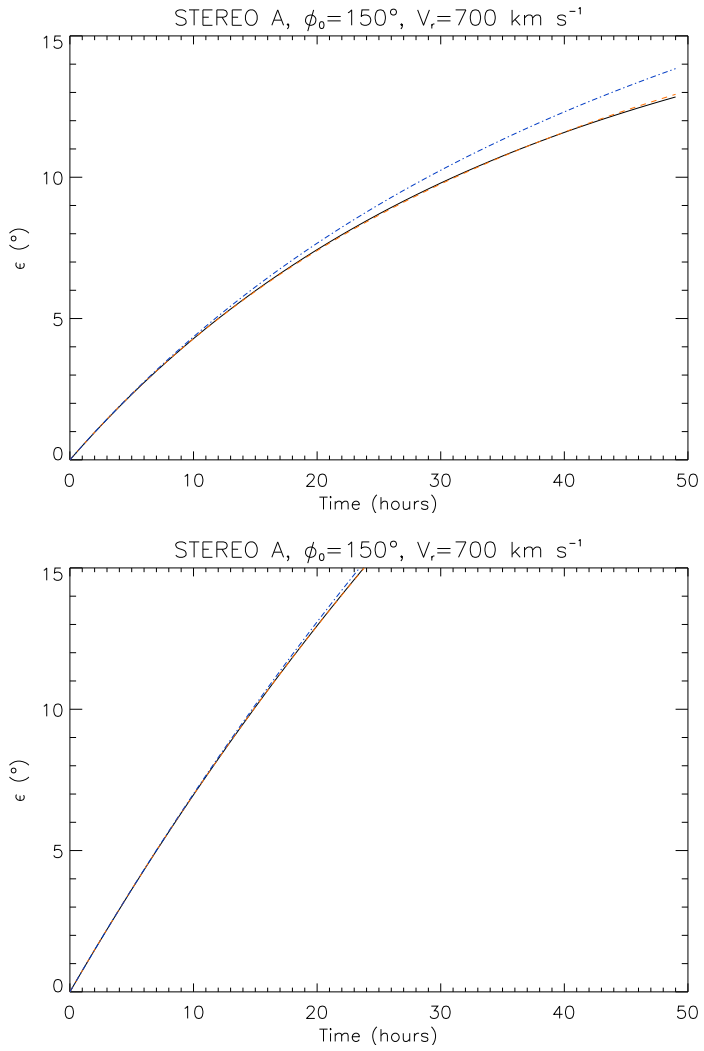

Figure 4.8: Same as Fig. 4.5 but for greater V_r and ϕ.

As previously mentioned, the traces were simulated for 50 1 hour time steps. This ensured that the faster traces did not exceed ≈1 AU in radial distance. This of course also means that the slower traces were only simulated through the inner heliosphere. In some instances, the slower traces were separately simulated out to greater radial distances (though still within 1 AU) but this was not found to alter the results significantly.

4.3 Practical test

I now seek a practical situation in which the above analysis can be tested. Rouillard *et al.* (2010) performed fitting on a series of individual time-elongation profiles associated with CIR-related transients determined from both STEREO-A and STEREO-B HI. They found that the estimated propagation speed varied as a function of ϕ, the two appearing to have an inverse relation, which was unexpected. Table 4.1 (excluding the final column) reproduces Table 1 from their paper (with some of the information slightly restructured for ease of reading), showing this relationship, with data from each of two CIRs that they presented from STEREO-A observations, labelled CIR-D and CIR-E. Fig. 4.9 from their paper shows each of the CIRs in question (subplot a) and the individual modelled time-elongation profiles (subplot b). The final column of table 4.1 shows an estimate for the radial propagation speed using the method in which spacecraft motion is corrected for. I did not reanalysise Rouillard's j-maps but rather took the propagation values they estimated (shown in Table 4.1) and then, using those values as ϕ_0 and V_r (i.e. the inputs for Figures 4.6 and 4.7) estimated what the same values would be, incorporating spacecraft motion. This differs from the analysis presented in the next chapter, as here we are still performing fits to single time-elongation profiles, whereas later we shall present general fits to a whole family of CIR-related traces. Although the variation in ϕ has not been included here, for each trace this was a systematic difference of no more than 2°, in line with Figures 4.6 and 4.7 and thus lies within the authors' error margins. The errors on the new V_r values should be comparable with the original. It can be seen that in most instances, correcting for

spacecraft motion makes little difference to the estimated speed, however for more extreme ϕ values, there is a noticeable difference, in each case acting such that the relationship between ϕ and V_r previously noted is reduced, though not completely removed. That this effect is only noticeable for extreme ϕ values is consistent with the analysis conducted in the previous sections, however the fact that the overall trend remains is perhaps puzzling. It is worth remembering however that in the work here I have only relaxed a single assumption regarding the motion of a transient. Rouillard *et al.* (2010) themselves suggest that the trend observed could be caused assuming a transient has a constant propagation speed. In reality of course, there are a multiple reasons that the speed of a transient might vary, such as acceleration close to the Sun and drag caused by interactions between the transient and ambient solar wind. The overall trend observed by Rouillard *et al.* (2010) could therefore be a combination of the varying speed of the observed transient and a smaller effect from the motion of the observing spacecraft. They suggest that it might be possible to incorporate transient speed as one of the fitted parameters, leading to a three parameter fit. As mentioned previously, Rouillard *et al.* (2010) also performed this analysis on STEREO-B HI observations, however they only have a few tracks from each CIR as seen from STEREO-B and so I have only included the STEREO-A results here.

4.4 Conclusion

The effect of not accounting for the movement of the STEREO spacecraft when predicting the speed and propagation direction of solar wind transient signatures in the STEREO HI observations has been assessed, and shown that this can make a noticeable difference to the results, causing the inferred radial speed to differ by tens of km s^{-1} or more for extreme viewing geometries. Having assessed the effect for both the fixed-ϕ and harmonic mean fitting techniques it was found that both are affected by not accounting for this movement, with the radial speed affected more for fixed-ϕ and propagation direction affected more for harmonic mean. For either technique however, it is concluded that the effects of spacecraft motion should be

Table 4.1: Trajectories of transients determined from HI-A observations. The quoted time is that at which the transient passed the $\epsilon = 5°$ point. The estimated propagation characteristics obtained by (Rouillard *et al.*, 2010) are shown in columns labelled ϕ and V_r. The final column, labelled New V_r shows an estimate of the radial propagation speed assuming the spacecraft are allowed to move. The uncertainty on the New V_r values are comparable with those from Rouillard's original work, as we have not re-analysed the data.

Track	Date	Time (UT)	ϕ (°)	V_r (km s^{-1})	New V_r (km s^{-1})
CIR-D					
a	09 Sep	0107	84 ± 04	268 ± 14	268
b	09 Sep	1945	82 ± 09	288 ± 24	288
c	10 Sep	0657	78 ± 10	285 ± 16	285
d	10 Sep	2139	63 ± 11	299 ± 11	298
e	11 Sep	0752	61 ± 11	311 ± 18	309
f	11 Sep	2019	37 ± 07	335 ± 07	324
CIR-E					
g	17 Sep	0531	80 ± 08	307 ± 21	307
h	17 Sep	1412	80 ± 11	306 ± 34	306
i	18 Sep	0138	59 ± 10	321 ± 07	319
j	18 Sep	0720	52 ± 09	319 ± 07	316
k	18 Sep	1719	55 ± 12	340 ± 09	337
l	19 Sep	0612	40 ± 06	324 ± 07	314

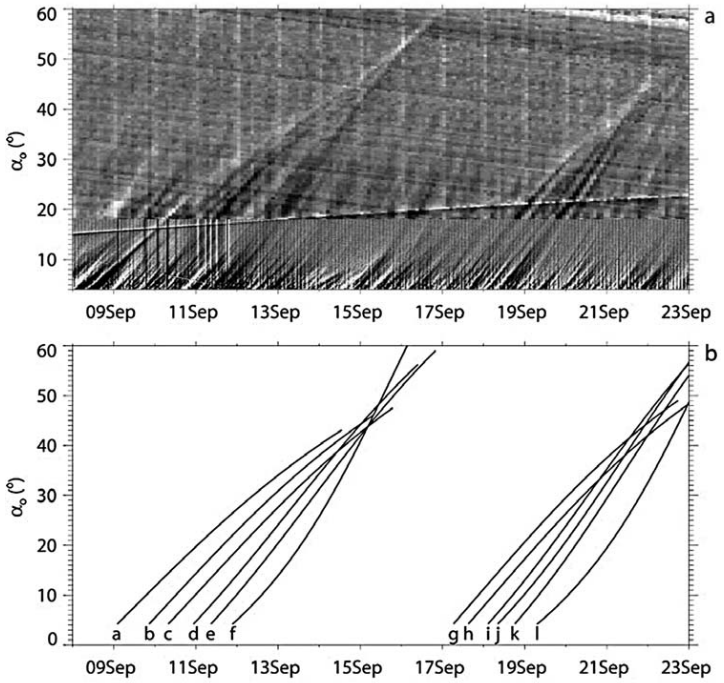

Figure 4.9: a) shows the two CIRs outlined in table 4.1, with the individual time-elongation profiles shown labelled in panel b).

taken into account. These results were applied to data taken from Rouillard *et al.* (2010) and we found that effects from spacecraft motion can be seen in observational data. There are other sources of error associated with HI observations and some of these could well be larger than the effects from spacecraft motion discussed here (for example inaccuracies due to the assumed geometry of features). This does not however change the fact that spacecraft motion does have a part to play and accounting for this source of error will have direct implications for the predicted arrival times of solar wind transients at Earth and hence for space weather studies.

The effects discussed in this chapter will potentially become especially important for planned heliospheric imagers on upcoming heliospheric missions. For example, Gopalswamy *et al.* proposed an "Earth-Affecting Solar Causes Observatory" (EASCO), which would ideally include heliospheric imagers and sit at the L5 lagrange point. Choosing this location offers a fixed (relative to the Sun-Earth system) location from which to make observations of the solar wind. The two lagrange points, L4 and L5 each equally suitable to make observations of CMEs, however the authors state that L5 is preferable for making observations of CIRs as this position will allow insitu observations to be made of CIR-related features before they impact the Earth, whereas the a spacecraft at L4 would only be able to measure the CIR after it had already impacted the Earth. For remote observations however one reaches a different conclusion. If a spacecraft were to mount a heliospheric imager with the Sun and Earth lying at the edges of its field of view, imaging the region of space between the Sun and Earth, in a similar manner to the STEREO spacecraft, then a spacecraft at L5 is already limited as it cannot remotely observe a CIR until after the feature has passed the spacecraft's location. The field of view of a spacecraft at L4 would allow it to observe the CIR earlier. If we include the effects discussed in this chapter, the case for heliospheric imager at L4 rather than L5 becomes even stronger. If one wished to make most observations when the effects of spacecraft motion were negligable, then ideally one would wish to observe features when $40^\circ < \phi < 140^\circ$. Including this restriction would mean that a heliospheric imager at L5 would only observe features 20° (1–2 days) before it impacted with the Earth. A heliospheric imager on the other hand could observe 20°, or 1–2 days before it arrived at the L5 point, or 5–7 days before it arrives at the Earth.

Whether one incorporates spacecraft motion into one's analysis of solar wind transients, or restricts oneself to observing geometries for which it makes little difference, it is preferable to have a heliospheric imager placed at L4 as opposed to L5. This is in opposition to the optimal position for in situ observations, and indicates that if a heliospheric imager were to be incorporated into such a mission, it would be preferable to have a two spacecraft mission, a main spacecraft at the L5 point, and then a secondary spacecraft mounting heliospheric imagers at the L4 point. This would allow each type of observations to have their optimal position and also allow similtaneous insitu and remote observations of the same CIR feature as it corotated with the Sun.

Chapter 5

Assessing the Effect of Spacecraft Motion on Single-spacecraft Tracking of Solar Wind Transients Associated with Corotating Interaction Regions

5.1 Introduction

In this chapter I consider the effects of spacecraft motion on solar wind transients associated with CIRs. In order to do this, I perform fitting to CIR-related solar wind transients using Eq. 4.1, then perform fitting incorporating the modification to account for spacecraft motion outlined in the previous chapter. Having considered these implications I then look at a selection of identified CIR-related events and perform a survey of these, looking at typical features and trends.

Typically, fitting to CIR-related solar wind transients is conducted on each of a series of individual time-elongation profiles (e.g. Rouillard *et al.* (2008) and Rouil-

lard *et al.* (2010)). Each of these profiles will of course correspond to a single blob entrained at the stream interface. In contrast with this, Sheeley and Rouillard (2010) use the general structure of a CIR to perform their fitting and I follow their example. Fixed-ϕ fits were performed to some of the individual tmie-elongation profiles within a CIR and these then used as a starting point to obtain a fit by eye by varying V_r and the location of the source. One of the clearest features than can be fitted to is the 'leading edge' of a CIR, made up of the overlapping traces of multiple individual transients. Figure 5.1 shows an example of this, with traces fitted to three different families of traces. The second CIR presented in Figure 5.1 was shown by Rouillard *et al.* (2008) to be likely caused by a coronal hole that extended from the solar north pole down to the equatorial regions. By trying a variety of different fits with different speeds, I estimated that the uncertainly on the radial propagation speed was about 30 km s^{-1}.

As seen in STEREO HI, transients related with CIRs can be seen to converge at higher elongation values (30–50°) as seen by STEREO-A (as can be seen in Fig. 5.1) and diverge as seen by STEREO-B. This converging/diverging nature of the CIRs can be used to identify the events as seen in STEREO HI.

5.2 CIR propagation speed

40 clear CIR-related transient features were identified in STEREO-A HI from 01/2007–06/2010, and fits were performed to the whole family of traces in each instance to derive estimated radial propagation speeds, using the fixed-ϕ approximation. The fitting was performed firstly ignoring spacecraft motion and subsequently incorporating the correction for spacecraft motion outlined in the previous chapter. For each CIR identified this way, I thus had a pair of estimated radial propagation speeds (as opposed to a single speed per time-elongation profile). These radial propagation characteristics were used to identify CIRs as seen in-situ at ACE and comparisons were made between the HI derived parameters and those measured in-situ. The details of these CIRs can be seen in Table 5.1. Details of the fitting

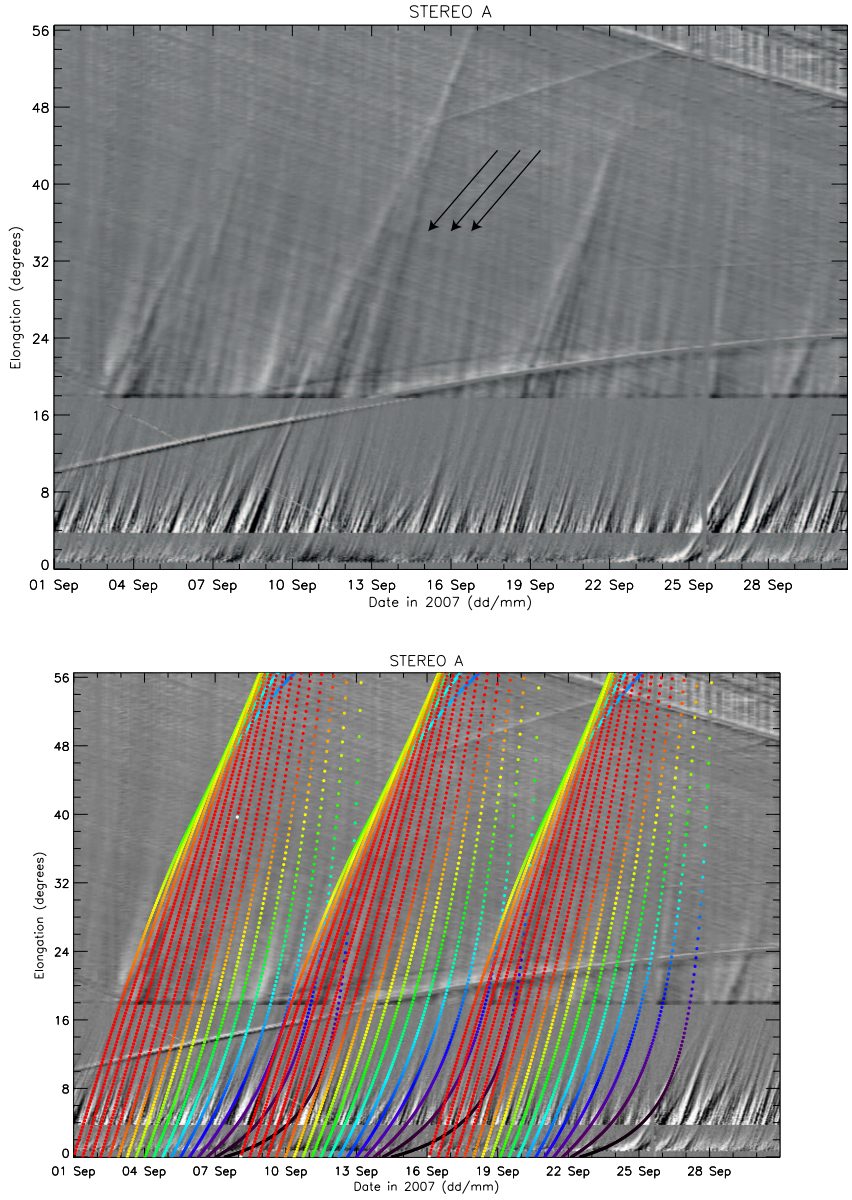

Figure 5.1: The top panel (2a) shows an example J-map extending over September 2007 showing the structure of three CIRs as seen from STEREO-A. The bottom panel (2b) shows the same J-map, but with superimposed traces of ϵ as a function of time, each trace corresponding to a single transient with a constant ϕ. The traces are colour-coded according to the scattering angle such that those regions in red should appear brighter than those that are blue/purple.

procedure are described below.

Figures 5.2 and 5.3 show the imaging and in-situ signatures, respectively, of one of the CIRs considered in this study, being the third event in Figure 5.1. The top panel of Figure 5.2 reproduces the J-map over an 11 day period - extending from 16/09/2007–27/09/2007. The middle panel shows the same J-map but overplotting the envelopes of traces associated with the old fit and the bottom panel shows the same J-map again, with the envelope of traces associated with the new fit overplotted. The curves start at ϕ of 180° and decrease in 5° steps. In this example, each set of overplotted envelopes make for a convincing fit to the underlying CIR structure (with the proviso that the fit is poorer at lower elongation values) and the old fit yields a radial speed 280 km s^{-1} and the new fit a speed of 450 km s^{-1}. Figure 5.3 shows in-situ data for the event in question. In the top panel is the bulk speed (black) and proton number density (blue). The next three panels show each of the x, y and z components of the IMF, with $\pm|\mathbf{B}|$ overplotted in grey. In the bottom two panels are the flow pressure and ion temperature. The red line shows the start of the CIR signature. It can be seen that the in-situ measured speed of the transient (i.e. the speed of the base of the velocity trough) is around 380 km s^{-1}. It could perhaps be argued that a better identification would involve considering the peak of the density enhancement and associated speed as this would be more representative of the movement of the density feature that HI would observe, however it was not possible to identify this value for each of the 40 features observed. For the sake of consistency, the base of the speed ramp was used, i.e. the time just preceding the speed enhancement.

Figure 5.4 considers each of these 40 events identified in STEREO-A HI J-maps and compares the average CIR radial propagation speeds as determined by fitting to families of tracks in the HI J-maps plotted against the slow solar wind speed as measured in-situ at ACE. It can be seen that while there is a lot of scatter, the old HI-derived radial speeds appear to fall below the line of unity between the two and the newly derived speeds appear to be distributed around the line. This indicates that by ignoring spacecraft motion, unphysical low speeds are arrived at, but that when spacecraft motion is incorporated, one sees that the features being observed

Table 5.1: Timing and propagation speed of the 40 events used in this study. The old start time is that of the time-elongation profile that corresponds to $\phi = 90$ and the new start time that of the time-elongation profile that starts at $\phi = 180°$ to the nearest hour, each written in the format dd/mm/yyyy hh:mm. By trying a variety of different speeds in the fits, the uncertainly in propagation speed was estimated to be about 30 km s^{-1}.

Old start time	Old V_r (km s^{-1})	New start time	New V_r
11/05/2007 12:00	260	04/05/2007 09:00	290
08/06/2007 12:00	220	04/06/2007 12:00	400
16/06/2007 00:00	250	10/06/2007 18:00	390
14/07/2007 06:00	310	11/07/2007 02:00	360
24/07/2007 00:00	230	18/07/2007 00:00	320
04/08/2007 00:00	270	28/07/2007 06:00	350
14/08/2007 00:00	300	08/08/2007 16:00	440
01/09/2007 00:00	250	25/08/2007 00:00	280
08/09/2007 04:00	250	01/09/2007 00:00	280
16/09/2007 06:00	280	10/09/2007 18:00	450
06/10/2007 00:00	255	28/09/2007 10:00	280
10/11/2007 12:00	270	04/11/2007 00:00	360
20/01/2008 00:00	250	13/01/2008 00:00	300
01/02/2008 00:00	340	24/01/2008 18:00	400
17/02/2008 06:00	310	10/02/2008 06:00	350
27/02/2008 00:00	300	18/02/2008 06:00	320
18/03/2008 00:00	390	09/03/2008 12:00	380
17/05/2008 12:00	290	11/05/2008 08:00	390
11/07/2008 00:00	260	04/07/2008 04:00	320
15/07/2008 00:00	400	10/07/2008 06:00	340
14/11/2008 18:00	260	06/11/2008 22:00	270
02/12/2008 00:00	260	25/11/2008 16:00	360
21/12/2008 06:00	290	14/12/2008 14:00	350
30/12/2008 00:00	240	25/12/2008 04:00	250
17/01/2009 00:00	270	10/01/2009 07:00	330
25/01/2009 18:00	260	18/01/2009 19:00	310
05/02/2009 06:00	330	29/01/2009 00:00	340
13/02/2009 00:00	310	05/02/2009 18:00	350
22/02/2009 18:00	300	15/02/2009 15:00	300
02/03/2009 00:00	230	28/02/2009 15:00	330
10/03/2009 12:00	270	04/03/2009 00:00	330
07/04/2009 00:00	260	31/03/2009 00:00	310
30/05/2009 00:00	240	24/05/2009 12:00	370
01/10/2009 00:00	220	27/09/2009 00:00	240
30/10/2009 06:00	230	22/10/2009 08:00	260
20/02/2010 18:00	230	14/02/2010 02:00	280
27/02/2010 06:00	350	20/02/2010 18:00	390
12/05/2010 12:00	320	06/05/2010 02:00	400
19/05/2010 00:00	300	11/05/2010 12:00	330
08/06/2010 06:00	290	01/06/2010 20:00	380

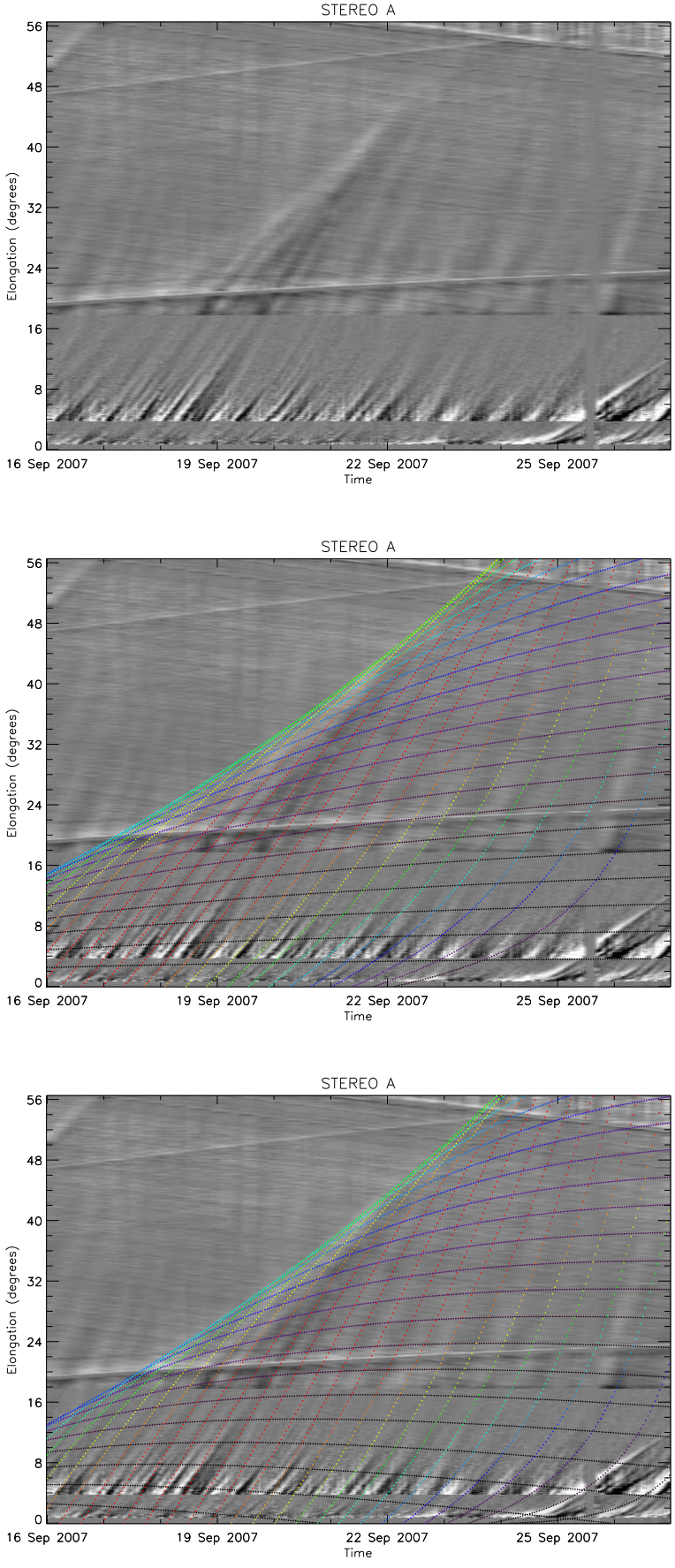

Figure 5.2: An event taken from September 2007, showing a J-map for an 11 day period in the top panel in which can be seen a CIR. The middle panel shows an overplot of the previous model fits, neglecting spacecraft motion and the bottom panel shows the fitted envelope of profiles, incorporating spacecraft motion, overplotted and again colour-coded according to scattering angle, such that red redions would be expected to be brigher than the blue/purple.

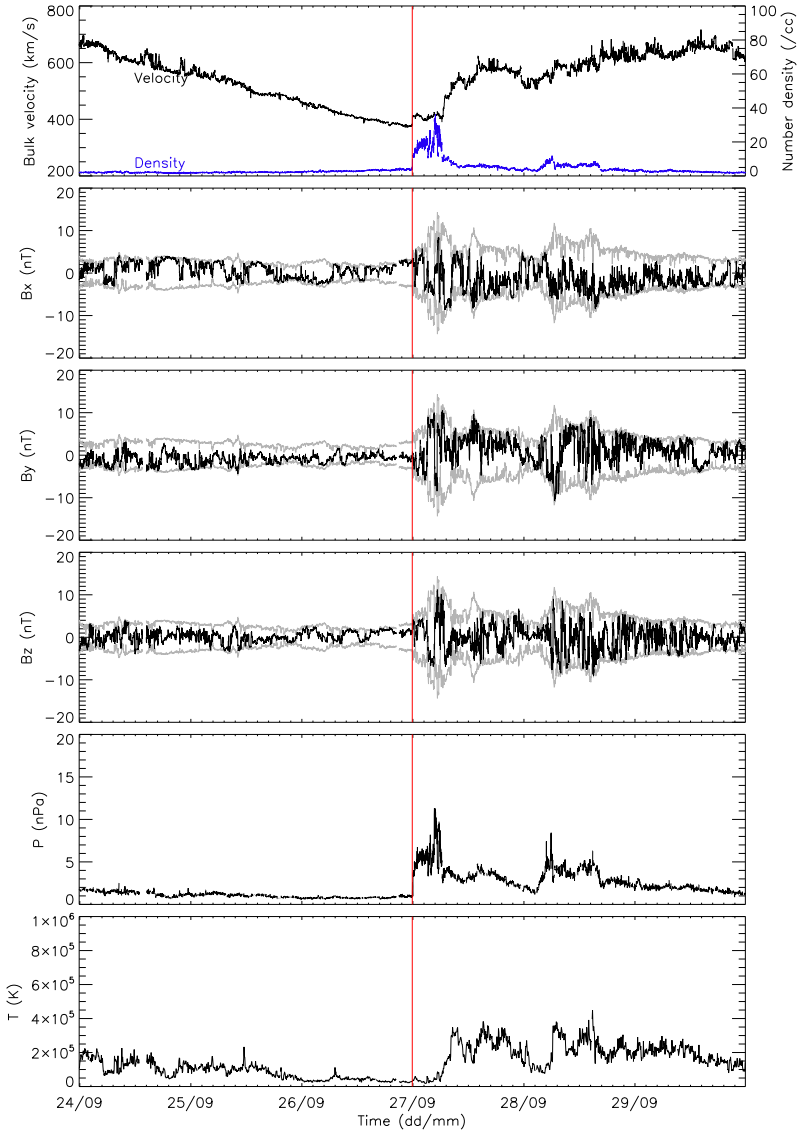

Figure 5.3: In-situ data from a particular event in this study and used as an example in the text. The top panel shows the bulk speed and number density data, next three panels the IMF and the bottom two panels pressure and temperature. The red line shows the moment before the speed increase. The speed of the slow solar wind preceding the CIR is ≈ 380 km s^{-1}.

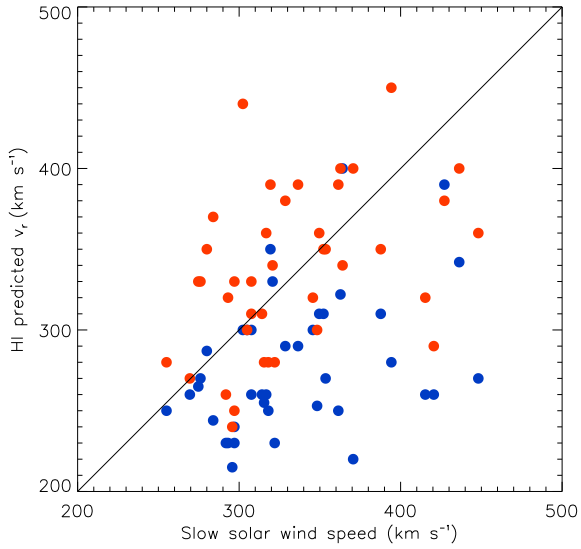

Figure 5.4: A plot showing the speed as measured by HI vs the slow solar wind speed as measured in-situ at by ACE. The straight line corresponds to a 1:1 relationship and the speeds from the old fit are shown by blue circles and those from the new fit in red circles.

are travelling at (or very close to) the slow solar wind speed, which is much more physically realistic. This is not an obvious result however. It might be expected that the stream blobs might travel at some intermediate speed between the fast and slow solar wind speeds, but this does not appear to be consistent with Figure 5.4. This does agree however with the findings of Sheeley *et al.* (1997), who use observations from the Large Angle and Spectrometric COronagraph (LASCO) on-board the SOlar and Heliospheric Observatory (SOHO) to track stream blobs close to the Sun. They noted that the blobs appeared to passively trace the outflow of the slow solar wind.

Some caution should be used here however. If one performs a linear fit to each of the sets of data in Figure 5.4, one arrives at relationships of $y = 0.343(\pm 0.144)x + 161(\pm 49.8)$ for the blue points and $y = 0.374(\pm 0.171) + 209(\pm 59.0)$, where the values in brackets show a single standard deviation. It can be seen from this that the results from the newer model appear to indeed have an increased propagation speed in general, but that comparing these estimated speeds with those measured at ACE is perhaps not very reliable. Thus using this to compare the two sets of data originally presented in Table 5.1 , it can be seen that the two sets of data do seem to be significantly different from each other, though only just.

5.2.1 CIR periodicity

If the same long-lived source region on the Sun is causing a repeating sequence of events at the vantage of a single fixed observer, then it should have a constant Carrington longitude, just separated by one solar rotation period (assuming the source region remains fixed on the solar surface). Calculating the Carrington longitude should also give an indication of the longevity of a given source region. If a source region is persistent for at least a solar rotation period, then it should appear again a solar rotation later at the same longitude. Knowing the rotation rate of the Sun and the approximate radial propagation speed and direction of the CIR allows one to predict its arrival at any point in the heliosphere, including tracing it back to a source at the Sun.

The top panels of Figures 5.5 and 5.6 show a year-long time series plots of the Carrington longitude for 2008. Each point on the plot corresponds to the location of a particular CIR source region on the Sun as it crosses the sub-solar point as estimated from the J-maps by tracing a particular CIR back to the solar surface and the vertical purple lines show Carrington rotations. The bottom three panels of Fig. 5.5 and 5.6 show the in-situ solar wind speed and proton number density, respectively, as measured at each of STEREO-B, ACE and STEREO-A. Fig. 5.7 is the same as Fig. 5.5 but for 2009 and Fig. 5.8 the same as Fig. 5.6 but for 2009. The in-situ speed and density data is taken from the IMPACT suite of instruments (Acuña *et al.*, 2008) on the STEREO spacecraft and from NASA's CDAWeb. The vertical red lines in the in-situ panels correspond to predicted arrival times of each of the CIRs considered in this study at each of these spacecraft. Plots such as this were generated for each of the years used in this study (2007, 2008, 2009, 2010). The Carrington longitude is defined to be 349.03° at 00:00 UT on 01/01/1995. Thus, the Carrington longitude (l), as presented in the upper panels of Figures 5.5, 5.6 and 5.7, is given by

$$l = \left(329.03 - \frac{360x}{P}\right) \bmod 360 \tag{5.1}$$

where x is the number of days that have passed since 00:00 UT 01/01/1995 and P is the synodic rotation period. Coincident with the first three Carrington rotations

(vertical lines) in Fig. 5.5 and 5.6, a source region is seen at a Carrington longitude close to 0°, which I interpret as the same region persisting for about 3 months. At the same time, a second source region coexists at a Carrington longitude of about 150°. The clearest example of a recurring feature can be seen in Fig. 5.7. Here, a series of points labelled 'C' can be seen to reoccur at approximately the same Carrington longitude with a periodicity of about one Carrington rotation (other source regions coexist with this). It can be seen however that the longitude of the source region appears to drift slowly. This would suggest either a source region that does not perfectly corotate with the Sun, or else that the rotation rate I use for the Sun is not appropriate. The Sun experiences differential rotation, with the equatorial region rotating faster than the poles, and so the rotation rate varies as a function of latitude. I have assumed the Carrington rotation period (≈ 27.28 days), which will not necessarily be representative. This is of course complicated as the J-maps used in this study were formed from data taken from the ecliptic plane, and the solar equator is at an angle to this of about 7.5°.

5.2.2 Predicted arrival times

As mentioned previously, knowing the radial propagation speed of the CIRs observed and the rotation rate of the Sun, it was possible to calculate predicted arrival times at various places in the heliosphere, at the same time taking into account the correction for spacecraft motion outlined in chapter 4. The bottom three panels of Figures 5.5 and 5.7 show the in-situ bulk solar wind speed as measured at each of STEREO-B, ACE and STEREO-A in turn. The data is taken from the IMPACT and PLASTIC suites of instruments (Acuña *et al.* (2008); Galvin *et al.* (2008)) on the STEREO spacecraft. The vertical red lines correspond to predicted arrival times of each CIR identified in HI at each of these spacecraft. Figure 5.6 shows the in-situ data in the same format for 2008. In this plot, the predicted arrival times make for a convincing match with density enhancements, indicating that the technique is at least identifying CIRs and attributing them a realistic propagation speed. Looking into this is more detail, I find that at ACE, for 20 (50%) of the events, the predicted arrival time falls within 24 hours of an in-situ signature. This number is 15 (37.5%)

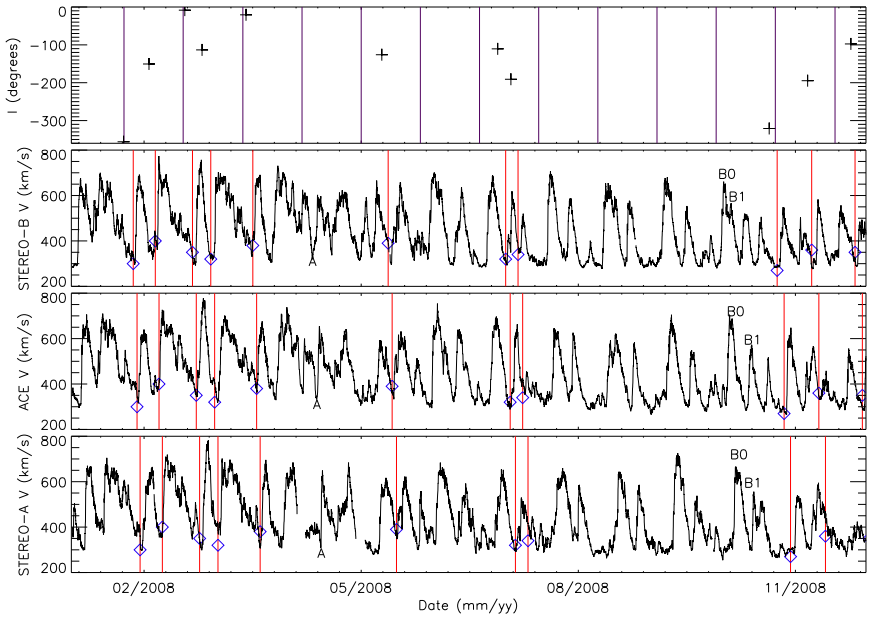

Figure 5.5: The Carrington longitude of CIR source regions as they cross the sub solar point (top). Carrington rotations are shown in purple. The next three panels show the in-situ speed data taken from the STEREO and ACE spacecraft, with predicted arrival times of CIR related features overplotted as red lines and the speeds as estimated from STEREO-HI blue diamonds. A couple of features in the data are pick out with letters and discussed in detail in the main text. This plot covers the year of 2008.

for STEREO-B and 16 (40%) for STEREO-A. This number might seem rather low, but in some cases, especially later in the mission, the stream interface has changed sufficiently as it corotates with the Sun so that there is no longer an obvious in-situ signature in one of the spacecraft, and in such cases the event is attributed an arrival time over 24 hours. It was also noticed that during towards the beginning of the STEREO mission, when the spacecraft were closer together, the discrepancy between the predicted arrival time and in-situ signature was smaller than it was later in the mission. It can also be seen that there can be multiple CIRs during a single rotation period of the Sun presumably associated with multiple source regions.

The analysis I conducted in order to estimate the propagation speed of the transients in this study assumed that the material had constant properties while it was being observed, i.e. it assumed that as the Sun rotated, the material it ejected would have a constant speed. Looking however at the in-situ data in Figures 5.5 and 5.6 it can be seen that there is actually a great deal of variability. Looking at the speed data at (for example) STEREO-B in the second half of 2008, there

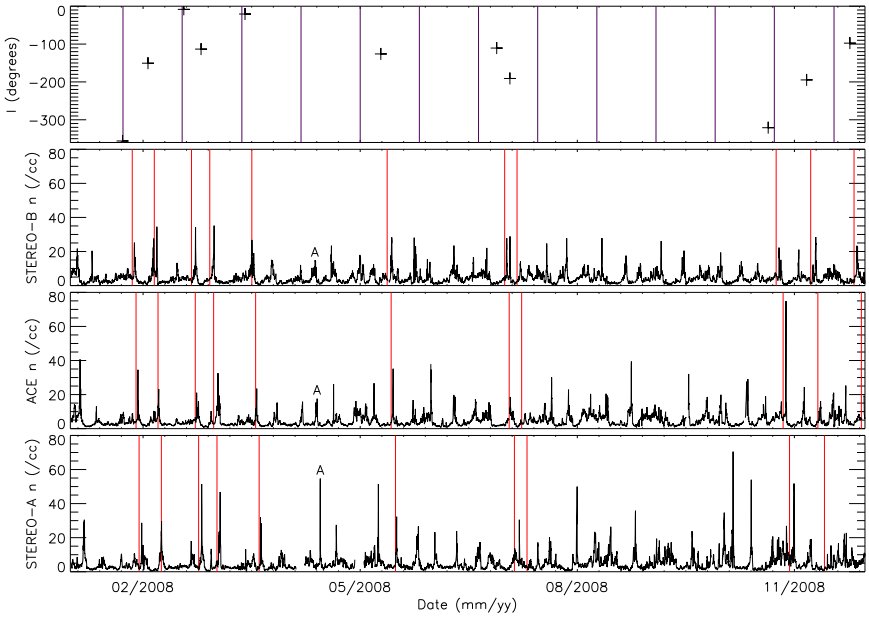

Figure 5.6: As Figure 5.5 but showing proton number density.

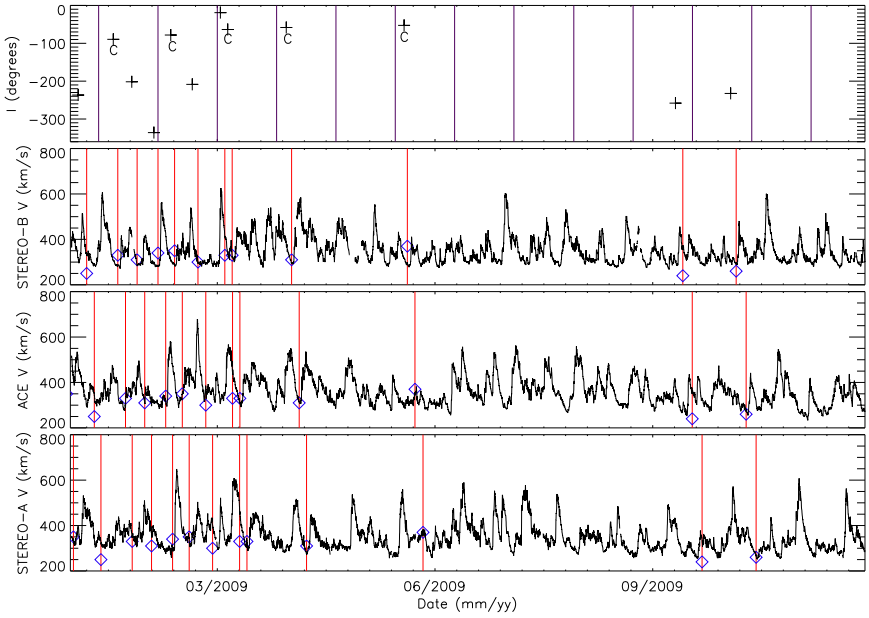

Figure 5.7: As Figure 5.5 but showing data taken from 2009.

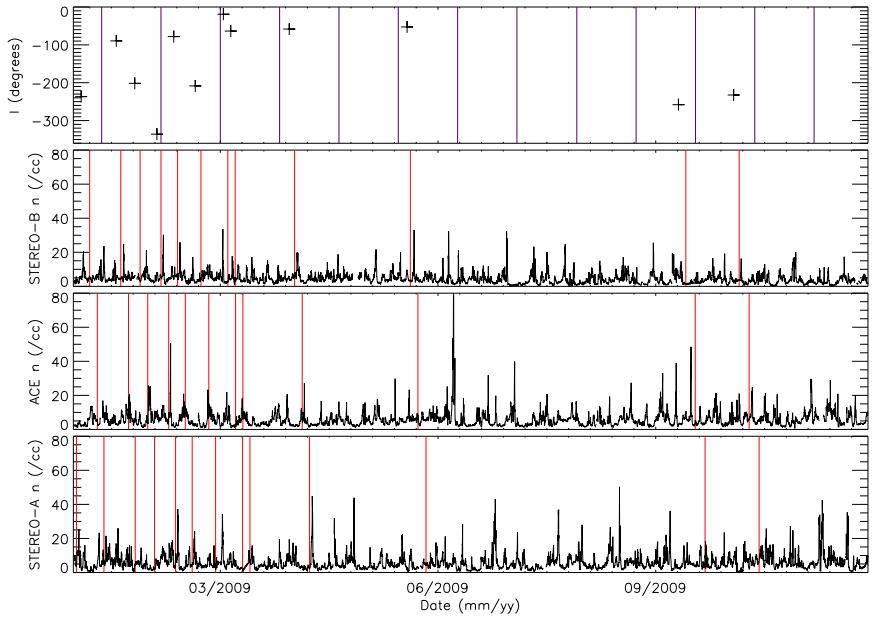

Figure 5.8: As Figure 5.6 but showing data from 2009.

are a pair of peaks that appear to reoccur with a period of a Carrington rotation, however the smaller scale structure of those peaks changes over this time. Thus, there is variability on the time scale of a Carrington rotation, i.e. approximately 27 days. During this period a pair of features of note have been labelled as 'B0' and 'B1'. As seen by STEREO-B, B0 is a speed enhancement with a smaller shoulder-like structure at a lower speed labelled B1. If STEREO-B in-situ data were being considered solely, the two would likely not be interpreted as different features, but having data from multiple spacecraft indicates otherwise. Considering now the same features as observed at ACE, the 'shoulder' on B0 has become less pronounced, and instead the speed of the fast solar wind stream that arrived behind it can be seen to appear with an enhanced speed, being now equal to the speed of the feature previously labelled as B1. Thus, it appears that there are two streams moving at differing speeds, and separating out as time progresses. Looking now at the feature seen by STEREO-A, we appear to be observing B1 merging with another fast solar wind stream. It can be seen that there is therefore significant variability between observations from each of the spacecraft. Looking now at another feature, labelled 'A' in each of the plots, we can see in the speed data that there is a fast solar wind stream, the leading edge of which over time appears to sharpen

dramatically, looking increasing like shocked solar wind. Comparing this with the density data, we see a density enhancement narrow with time, slowly increasing in maximum density, and then dramatically sharpening and increasing in density when seen at STEREO-A, once again looking more like a shocked structure. Both of these examples serve to illustrate that there is significant variability comparing data from one spacecraft to the next. Considering the rotation rate of the Sun and spacing between the spacecraft, this means that there is variability on the time scale of 1.5 - 2 days. Comparisons of CIR observations between spacecraft have been investigated by Mason *et al.* (2009) and more specifically in reference to STEREO observations (Leske *et al.*, 2008) and Wind observations (Sanderson *et al.*, 1998). These authors also noted that features present in in-situ data from one spacecraft are not always observed when one would expect in another spacecraft at the same orbital distance, as noticed here. They point out that one major factor that causes this is that the ecliptic plane, in which these observations are made, does not lie along the plane containing the solar equator. As a result, for data observed at STEREO-B for example, the source region might be above the ecliptic plane, which at STEREO-A it might be below the ecliptic and so the two spacecraft do not actually observe material from the same source region. All of this indicates that one should be quite careful when making approximations about constant solar wind conditions. However, as already mentioned, the predicted arrival times established from HI observations using such approximations appear to form a good match to the in-situ data.

5.3 Superposed epoch analysis

Taking the 40 CIR events identified in HI previously discussed, a superposed epoch analysis was conducted using the HI-predicted arrival times as the zero time, using hourly ACE and STEREO data. Figure 5.9 shows the superposed epoch analysis using in-situ data from the ACE spacecraft at L1 and Figures 5.10 and 5.11 show the same but using in-situ data from the STEREO-A and -B spacecraft respectively. In each case, the epoch zero time is shown by a red vertical line, the bulk proton

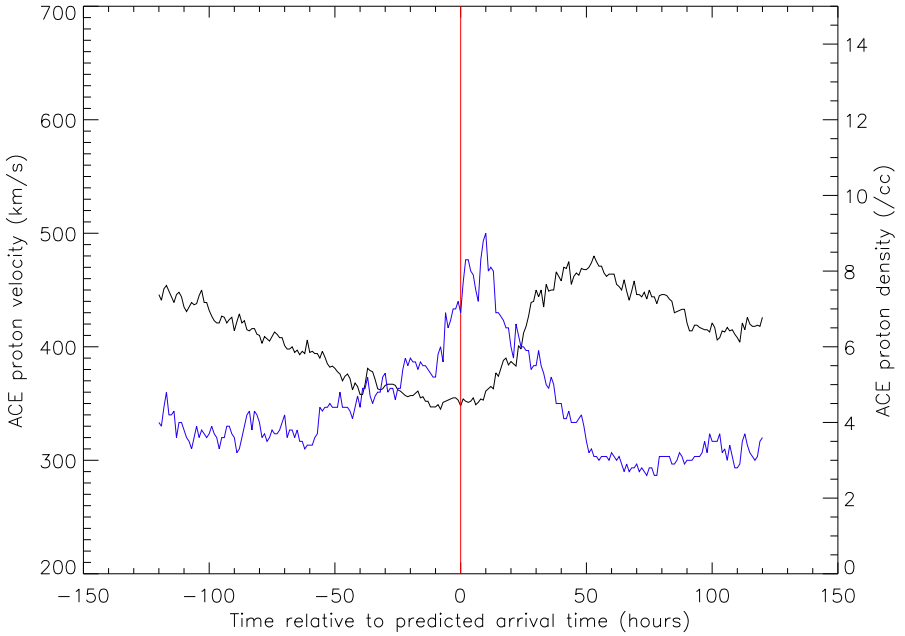

Figure 5.9: Shows the superposed epoch analysis using the ACE in-situ data. Speed is in black and density in blue.

speed by a black line and the proton number density in blue. Each of the plots is very similar, so in general we shall discuss them together. Each plot illustrates the speed and density enhancement typical of a CIR. At approximately the zero epoch time is an enhancement in the proton number density. At the same time, there is a low point in the proton speed, once again indicating that the material that is being observed by HI (the denser material) is travelling at the slow solar wind speed. In a similar superposed epoch analysis conducted by Davis *et al.* (2012), it appears that the denser material that should correspond to that observed by STEREO HI is not quite associated with the slow solar wind, but rather material travelling at a speed slightly higher than that. Comparing this with my results, the case is rather less obvious. There is perhaps the indication that the denser material might correspond to an intermediate speed in the STEREO-B plot (5.11), but this is not clear at all in the STEREO-A plot (Figure 5.10) and there is no real sign of this as seen at ACE (Figure 5.9). As the plots that Davis *et al.* (2012) present are created from OMNI data, one might expect their results to agree most closely with the plots presented here from the ACE spacecraft, though their analysis differs from mine. On balance, it appears that these CIR-associated transients appear to be travelling at, or perhaps very close to, the slow solar wind speed, in general agreement with

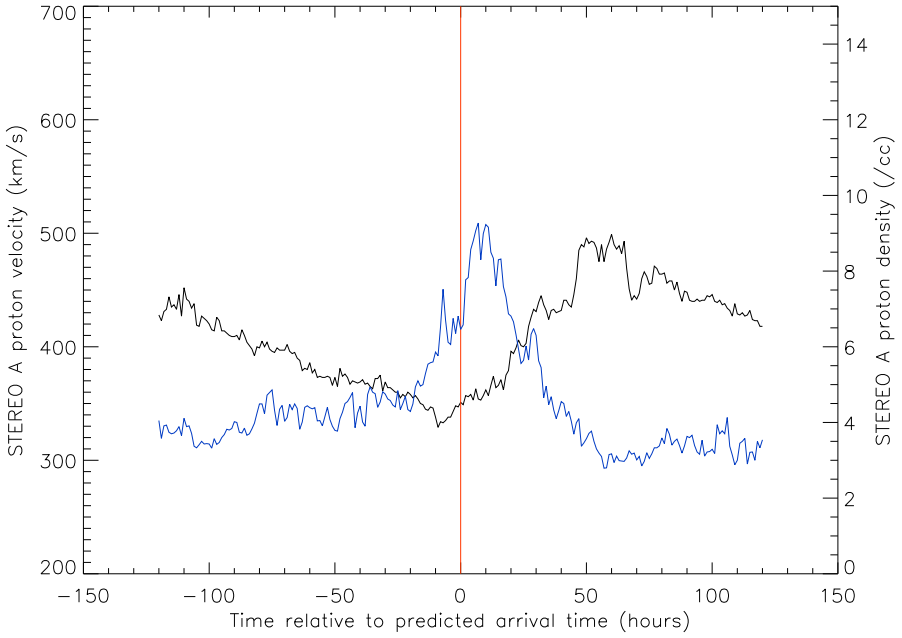

Figure 5.10: Shows the superposed epoch analysis using the STEREO-A in-situ data.

Sheeley *et al.* (1997).

Finally, the predicted arrival times shown in Figures 5.9 – 5.11 as red lines appear to consistently appear ahead of the density peak, by 15 ± 18 hours, indicating that we are perhaps systematically slightly overestimating the transient propagation speed.

5.4 Discussion

Taking a look at the in-situ data and predicted arrival times more closely, it is apparent that during the period of study, solar wind source regions on the solar surface can last for multiple solar rotation periods, however a given source does not eject material with constant properties on time scales of even a few days, in agreement with Mason *et al.* (2009). This suggests possible sources of error in HI solar wind that fitting techniques assume constant propagation speed. Perhaps by relaxing some of these assumptions, it might be possible to improve the reliability with which transient arrival times at 1 AU can be ascertained, thereby improving space weather predictive capabilities. Work has been conducted by Lugaz and Kintner

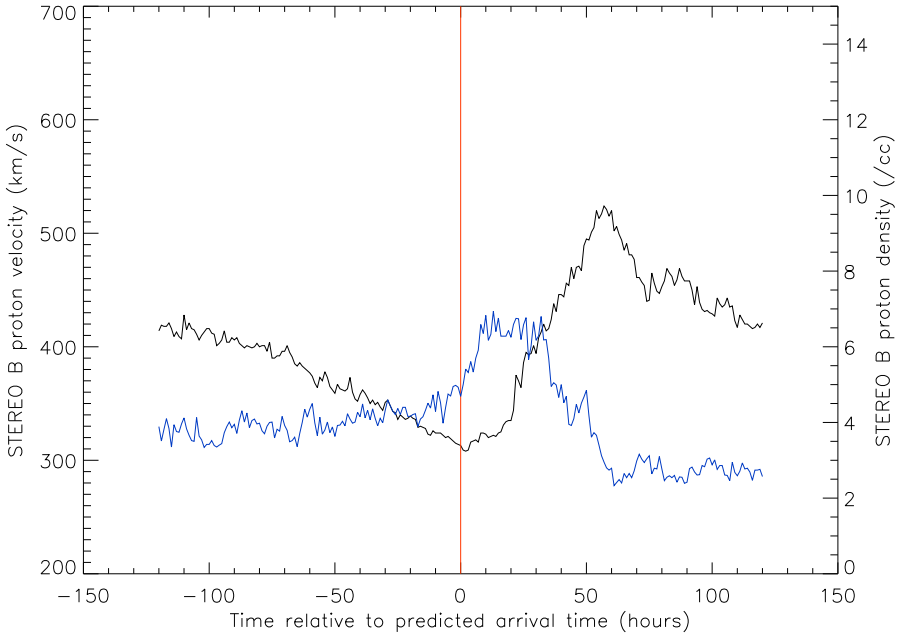

Figure 5.11: Shows the superposed eoch analysis using the STEREO-B insitu data.

(2013) investigating the effects of drag on solar wind transients, and Sheeley *et al.* (1997) have considered acceleration through a coronagraph field of view, and if this effect could be folded into estimates of solar wind transients seen in STEREO HI, the fitting might be improved. This shall be attempted in the next chapter

It has been seen that rotation after rotation, a given source region appears to drift across the surface of the Sun. This could be a real effect, however it is more likely that the rotation rate being used to represent these source regions is incorrect. Assuming that the only factor affecting rotation rate is the latitude of the source region, then it should be possible to ascribe each source region its own individual rotation rate. It does not appear however that using an average solar rotation period of 27.2753 days (as I have done) is reliable when considering timescales of a solar rotation period. To establish a more exact rotation rate, images of the solar disc taken from e.g. STEREO, the SOlar and Heliospheric Observatory (SOHO) and the Solar Dynamics Observatory (SDO) could be used to find the position (and hence latitude) of the source region.

5.5 Conclusion

Having analysed CIR-related solar wind transients from 2007 – mid 2010, we found that the modification suggested in the previous chapter to account for spacecraft motion can improve the estimated radial propagation speeds of CIR associated transients when performing fits to the general structure of a CIR. It was possible to predict their arrival times at three different locations in the heliosphere at a distance of about 1 AU and these predictions formed a good match with in-situ data signatures. It was found that fast solar wind source regions can persist for multiple solar rotations, however the properties of the material ejected from them is not a constant over these timescales and can vary noticeably over a matter of days. For future missions therefore, care should be taken when comparing results from spacecraft at different locations. This would be important if one were to compare for example insitu measurements from a spacecraft at the L4 or L5 points and a spacecraft at L1, such ACE. It was thus suggested that a more thorough examination of the transient acceleration profiles might allow for better fitting. It was noted that it is difficult to find a characteristic solar rotation rate for these source regions and the assumption that some standard rotation rate can be used for multiple source regions is not necessarily valid, but this could be improved by using images of the solar disc to find a location of a source region on the Sun and use this to estimate its latitude and thus its particular rotation rate. This underlines the importance of having imagers capable of imaging the source regions of a CIR. It was finally found that solar wind transients associated with CIRs seem to travel at or very close to the slow solar wind speed, a result that was not expected.

Chapter 6

Probing the CIR acceleration region

6.1 Introduction

The work in this chapter focusses on the behaviour of solar wind transients associated with CIRs close to the Sun. When using any of the fitting techniques outlined in previous chapters to establish propagation characteristics of solar wind transients from J-maps, it is generally assumed that the ϕ angle and radial propagation speed are both constants, at least out to 1 AU. In previous sections I have discussed the implications of allowing the ϕ angle to vary and showed that this can improve the estimated radial propagation speed. It is possible that relaxing the constant propagation speed assumption might also lead to improved fitting.

There has been previous work investigating the acceleration of solar wind transients. In Joshi and Srivastava (2011) they consider the behaviour of CMEs in the inner heliosphere using COR1 and COR2 on the STEREO mission. They consider 6 separate events and find that most of the acceleration of a CME occurs within 4 $R_{\odot}$ of the Sun centre. As a result of this, assuming that an observed feature has a constant radial propagation speed when using the previous techniques to analyse CMEs is perhaps valid. For most of the observing time of the CME, the radial

propagation speed would be approximately constant. Temmer *et al.* (2011) and Lugaz and Kintner (2013) investigate the acceleration of CMEs further out into the heliosphere, where viscous interactions with the solar wind slows them down.

Moving away from the specific behaviour of CMEs, Sheeley *et al.* (1997) and Srivastava *et al.* (1999a,b) tracked a number of moving coronal features seen by the Large Angle Spectrometric COronograph (LASCO) aboard the SOlar and Heliospheric Observatory (SOHO). They found that the features observed appeared to originate from the cusps (pointed ends) of helmet streamers, at a distance of about 3–4 $R_\odot$ from Sun centre and move with the slow solar wind, following a nearly parabolic path when their distance from the Sun was plotted against time, characterised by a constant acceleration of about 4 m s^{-2} through their field of view, which extended out to 30 $R_\odot$. Fig. 6.1 shows one of the events considered by Sheeley *et al.* (1997). In the top panel is distance from the Sun centre plotted as a function of time, showing the parabolic trajectory clearly. This panel is annotated with the results of a second order polynomial fit, generating estimates for the starting height of the feature (r_0) and acceleration of the feature (5.3 m s^{-2}). The second panel shows the propagation angle of the feature, which they note is approximately constant, and so corresponds to a radial ejection. The bottom panel plots speed as a function of distance and makes the acceleration of the feature very apparent.

When performing fits to time-elongation profiles seen in STEREO HI J-maps, the fitting is restricted to higher elongation values, as fits at lower elongation values are known to be poor (Williams *et al.* (2009), who found that from a theoretical assessment, a maximum error of 25° when the fit was performed over only small ($< 24°$ elongation values), compared with a few degrees when performed over the whole elongation range), with the modelled curves differing significantly from those that are observed. This can be seen in Fig. 5.2. As a plasma element would be expected to accelerate close to the Sun, it is possible that this is the cause of this discrepancy. With this in mind, the aim of this chapter is to establish whether allowing the speed of a solar wind transient associated with a CIR to vary (i.e. allowing the transient to accelerate close to the Sun) will improve the fitting of CIRs as seen in STEREO HI. We will also consider the extent of this 'acceleration

region' and whether it extends to a constant distance from the Sun, which would simplify any attempt to account for this effect, or changes its size with time, making it difficult to accommodate.

6.2 Polynomial fits to speed profiles

When considering the motion of solar wind transients associated with CIRs as seen in J-maps from STEREO HI and COR instruments, as discussed in previous chapters, one can use the fixed-ϕ technique to extract propagation characteristics from time-elongation profiles. It is possible however to re-write the fixed-ϕ expression (Eq. 2.7) as

$$r = \frac{r_{\mathrm{SC}} \tan \epsilon}{\sin \phi + \cos \phi \tan \epsilon} \tag{6.1}$$

where r is the radial distance of the transient. In previous chapters I have analysed a number of families of traces associated with CIRs. This means that for a given time-elongation profile that is a member of one of these families, we can estimate its ϕ value. In contrast to the previous section, I am interested in traces at low elongation values, as this is where much of the acceleration of transients is likely to occur and so it is more valid to assume constant ϕ, which I do to simplify the analysis. Thus, following on from the fitting performed in the previous chapter, each trace within a family will have a single ϕ value that represents its direction of motion and by considering where within a family of traces the one of interest lies, it is possible to attribute it with a ϕ value, as the phi values of traces within a family vary in a predictable manner, as stated in chapters 3, 4 and 5. Knowing this, it is possible by taking time-elongation values from a trace by selecting points on the trace to establish its radial distance as a function of time. I then perform polynomial fits of second, third and forth order to determine the plasma element acceleration properties. Having established typical acceleration behaviour, it might then be possible to apply this to profiles fitted to J-maps and consider any changes to the fitting that result.

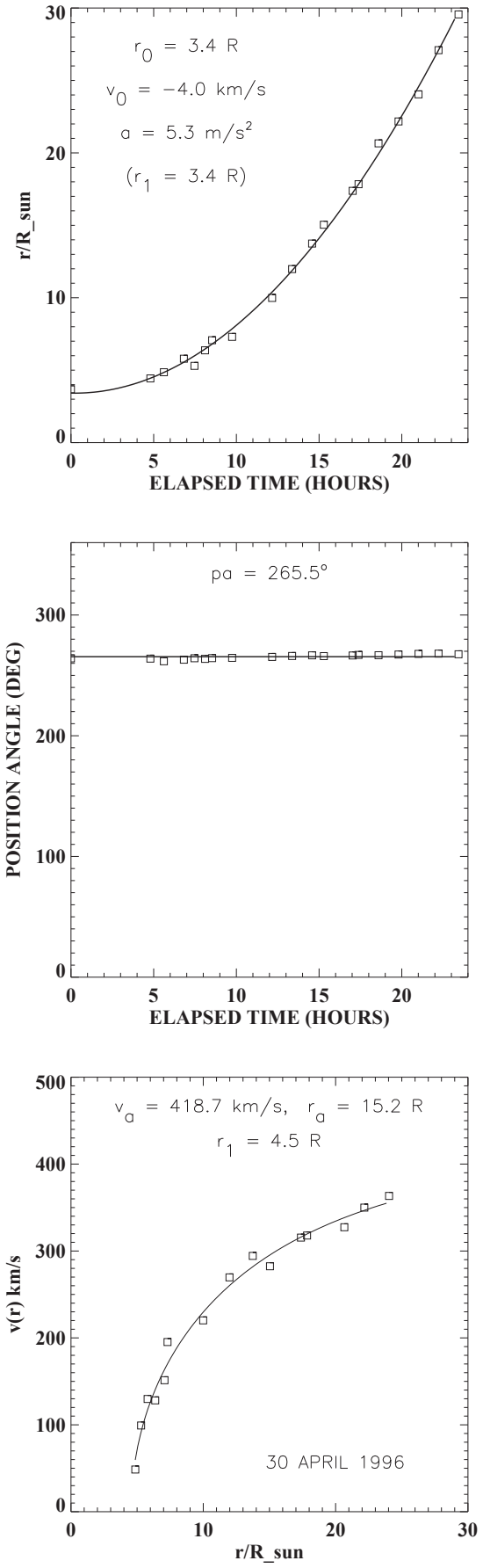

Figure 6.1: A reproduction of Figure 5 from Sheeley *et al.* (1997), showing the distance profile (top panel) position angle profile (middle panel) and speed profile (bottom panel) for one of their observed transients, making the acceleration experienced by the feature they are observing apparent.

In order to find the events to analyse, I used the list of CIR events in the STEREO HI-A data between 2007 and mid 2010 that I also used in chapters 4 and 5 and then looked for individual time-elongation profiles within this set that had a clear and well defined profile at small elongation values. In some cases, this resulted in selecting profiles that did not have a very clear time-elongation profile at larger elongations. The result was a set of 79 time-elongation profiles to use in this study. This number of events was smaller than first expected as the necessity for clear time-elongation profiles at low elongation values cut into the number of events. The two main constraints on this were firstly the necessity to have events that could be unambiguously identified in the lowest elongation region of the J-map, taken from COR observations and secondly to be able to follow this same trace into the field of view of HI1. It was not always easy to be confident of observing the same event crossing through the two fields of view. These were generally taken from different CIR events, though there were some instances in which multiple profiles were taken from a single CIR. In each case, from work presented in the previous chapters, I had a ϕ value that should correspond to each of the time-elongation profiles (assuming fixed-ϕ) and by feeding this, along with the time and elongation information into Eq. 6.1, it was possible to calculate the distance of the plasma element from the Sun. The fitting was then performed on the r(t) data.

In Fig. 6.2, I show three examples demonstrating the typical behaviour seen in the data. In each panel, the x-axis is time since the first point was measured and the y-axis shows radial distance from the Sun. The black crosses are the data points taken from the J-maps, the solid black line shows a second order polynomial fit, the dashed black line shows a third order polynomial fit and the red dashed line shows a 4th order polynomial fit. Sheeley *et al.* (1997) found in their main analysis that their data were consistent with a second order polynomial fit. Each of the top two panels in the figure represents one of the common situations seen in the data. In the top panel we can see that there is no discernible distinction between each of the fits, i.e. the solid and dashed black lines are essentially superimposed, so a second order polynomial appears sufficient to fit to the data. If we consider the middle panel however, this shows an example where there is a noticeable difference between the second and third order fits, with the latter a better fit to the data as the black

crosses follow the dashed line more closely than the solid line, i.e. it is apparent that the acceleration is not a constant. By looking at each fit by eye, it was found that of the 79 events investigated in this study, 53 (67%) showed a noticeable difference between these two fits. There was a much smaller group of cases (13, 16%) for which there was a noticeable difference between third and forth order polynomial fits. In no instance was the lower order fit clearly superior to the higher order fit, being at best comparable with the higher order polynomial. An example showing a difference between 3rd and 4th order fits can be seen in the bottom panel of Fig. 6.2, where the black crosses follow the red dashed line more closely than the black dashed line. To be more rigourous, Pearson correlation coefficients were found for each of the fits. In each instance, the correlation coefficient between the data (black crosses) and the fit was very high, never going below 0.99 for any fit of any order. The correlation coefficient variations were only seen from the third significant figure. This is no surprise, as simply by investigating the fits by eye it can be seen that often multiple fits fall within the error bars of the data points. In every instance however, the 4th order polynomial fit resulted in a higher correlation coefficient. These values have a very high level of significance, in every case having a p-value less than 10^{-8}.To distinguish between quality of fit provided by each order polynomial, a chi-squared test was performed on all of the fits. At the 0.05 significance level, in none of the cases was the second order polynomial judged by the chi-squared test to be the most appropriate. In 11 cases (14%) the third order polynomial was the most appropriate and in the remaining 68 (86%) of cases the 4th order fit was most appropriate. From performing the polynomial fit, one can extract the values of the coefficients (A–M) in Eq. 6.2 – 6.4 that correspond to that particular time-elongation profile. With these coefficients, it is possible to reconstruct the varying speed of the profile.

$$r = At^2 + Bt + C \tag{6.2}$$

$$r = Dt^3 + Et^2 + Ft + G \tag{6.3}$$

$$r = Ht^4 + Jt^3 + Kt^2 + Lt + M \tag{6.4}$$

Joshi and Srivastava (2011) found that most of the acceleration from a CME associated transient was conducted within the first few solar radii of its journey and Sheeley *et al.* (1997) found that for CIRs this distance was closer to 30 $R_\odot$, however I have been able to observe acceleration out to greater distances. While relaxing the assumption of radial propagation speed might not make much difference to CMEs therefore, it might make a noticeable difference to the low elongation fitting to CIR-related transients.

6.3 Application to CIR J-map fits

Our overall motivation for the analysis previously discussed is to investigate whether relaxing the assumption of constant propagation speed of CIR related transients as seen in STEREO HI can improve the fitting, especially at low elongation values. An additional motivation is to further attempt to distinguish between different order polynomial fits performed in the previous section and ascertain which is the more appropriate. With these objectives in mind, I consider the CIR event from which a time-elongation profile is taken and use each of the polynomial fits to vary the speed of the CIR. I then compare this with the fitting to the CIR with constant propagation speed to ascertain if the fitting is an improvement at lower elongation values. By varying the distance out to which the plasma element is allowed to accelerate, it should be possible to estimate the size of the acceleration region around the Sun and compare this with the findings of Sheeley *et al.* (1997). It should be possible to establish if different plasma elements associated with the same CIR experience the same acceleration, and by comparing the size of the acceleration region state which of the polynomial fits is the best to use.

In the top panel of Fig. 6.3 can be seen an example CIR J-map with a family of time-elongation profiles overplotted with a constant propagation speed, but variable

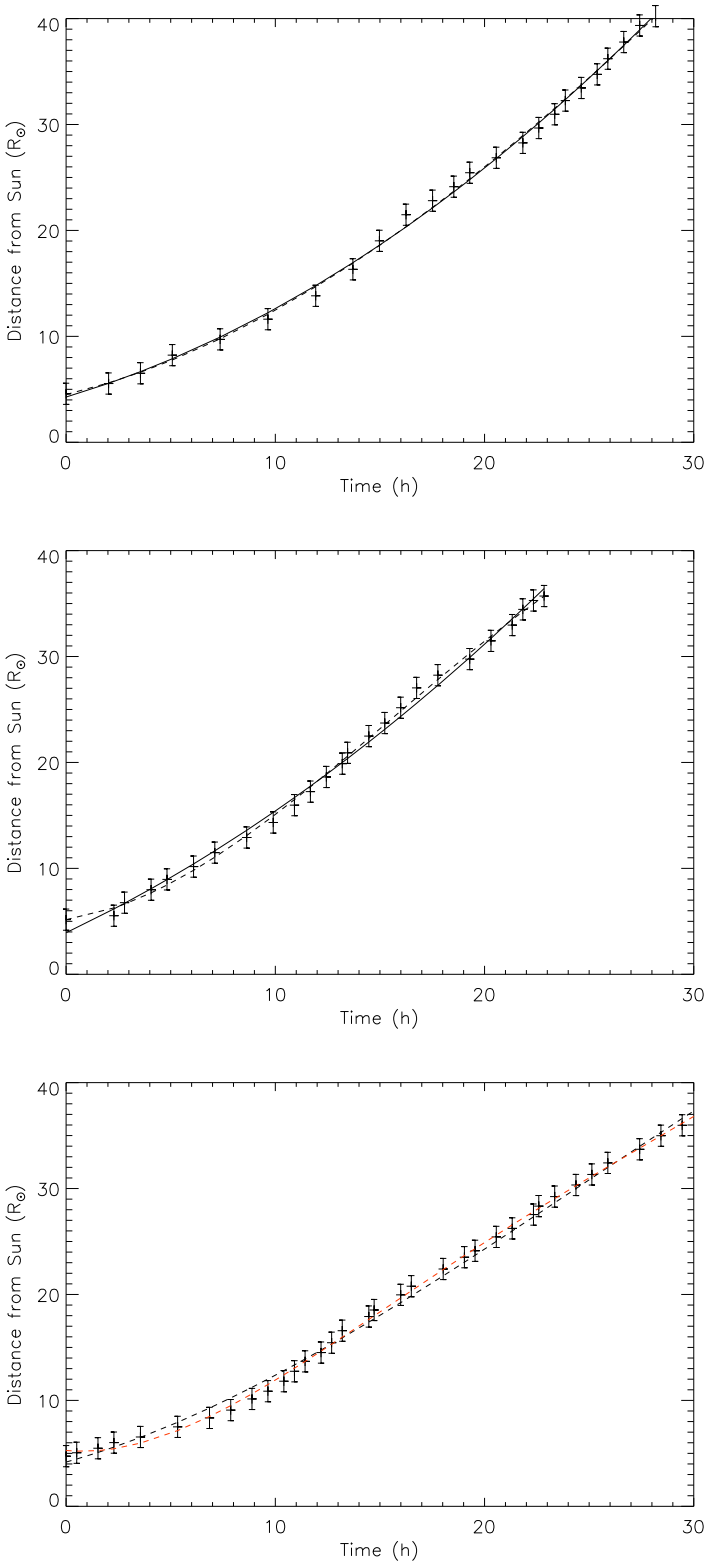

Figure 6.2: Showing examples of data extracted from low elongation time-elongation profiles traces, with the data extracted from a J-map (crosses), a second order polynomial fit (solid line), a third order polynomial fit (black dashed line) and a 4th order polynomial fit (red dashed line). The top panel shows an example where there is no discernible difference between the 2nd and 3rd order fits, the middle panel shows an example where there is an observable difference between the two and the bottom panel shows a noticeable difference between 3rd and 4th order fits.

ϕ, as done in chapters 5 and 6. In the middle panel is the same J-map, but with the propagation speed no longer constant. To allow the speed to vary, the coefficients of a forth order polynomial have been extracted from a fit to a time-elongation profile that is within the family of traces and then these coefficients used to recreate the changing speed of the family of transients. This acceleration has been applied to the whole of the J-map, and it can be seen that this results in material moving much faster than previously estimated, resulting in a poorer fit out to larger elongation values than previously observed, but a better fit at smaller elongations. This poor fit can be mitigated by only allowing acceleration out to a particular distance from the Sun. The results of fixing the speed after 12 $R_{\odot}$ can be seen in the bottom panel of Fig. 6.3 as an example. This distance can be varied to obtain an optimal fit. This is the same event as that plotted previously. We can see that this improves the fit compared with the middle panel of Fig. 6.3. In addition to a family of time-elongation profiles associated with a CIR in this figure, it is also possible to see a CME (possibly two) that starts on the 16th of May. The traces I have plotted will clearly not fit to these features.

By looking at the lower elongation regime of the panels of Fig. 6.3, it can be seen that when a constant propagation speed is used the fit is poor in this region, as the overplotted profiles do not match the curvature seen in the data as previously noted. By introducing acceleration close to the Sun, the curvature of the overplotted time-elongation profiles matches that of the observed profiles much more closely, indicating that this poor fitting at low elongation is indeed caused by acceleration of the transient close to the Sun.

By adjusting the distance out to which acceleration was incorporated, it was possible to once again fit overplotted families of time-elongation profiles to the observed traces. In each instance, there will be a particular distance radius that results in the best fit between modelled time-elongation profiles and those observed by HI. This distance was then taken to be the size (radius) of the acceleration region. This was done for each of the orders of polynomial used to represent the acceleration. For each polynomial, there were some events for which it was not possible to arrive at a satisfactory fit (2 for the second order polynomial, 9 for the 3rd order and 5

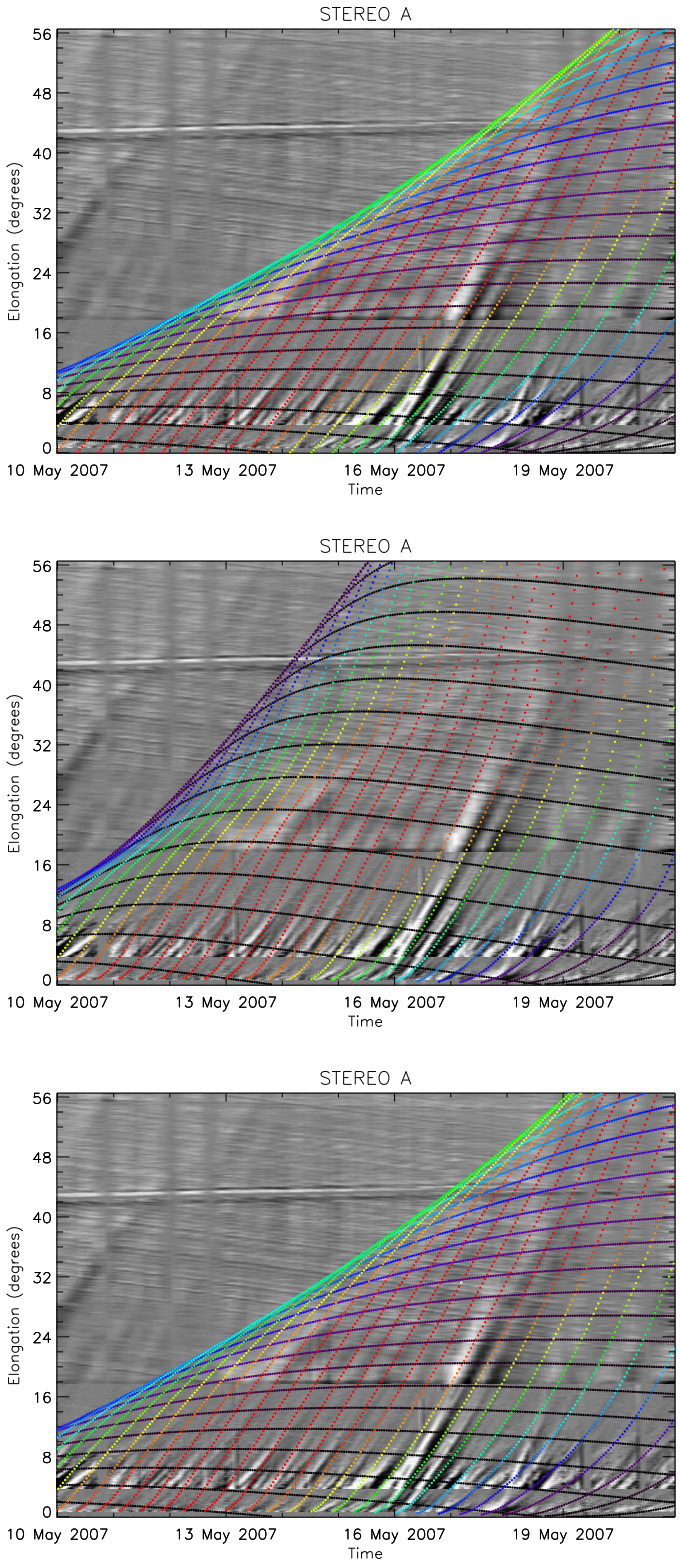

Figure 6.3: In each panel can be seen an example J-map, with overplotted time-elongation profiles assuming constant propagation speed (top) and variable propagation speed (middle). The bottom panel shows the J-map again, with overplotted time-elongation profiles, this time assuming a variable propagation speed from the Sun to 12 $R_{\odot}$ and then a constant speed from that point onwards. The lines are colour-coded according to scattering angle such that the red regions would be expected to be brighter than the blue.

for the 4th order). This could be due to a variety of reasons. In some instances the polynomial caused the propagation speed to reach a maximum and then start decelerating before a good fit with the observations was reached. In other instances it might be simply that the time-elongation profile identification could have been slightly ambiguous (despite efforts to avoid this). This could be particularly problematic when crossing between the fields of view of the different instruments. If two traces were quite close together on the J-map then it was possible that they were misidentified as a single trace, though as previously mentioned efforts were made to exclude events without clear and well defined traces so the impact of this should be minimal. Fig. 6.4 shows how many events (expressed as a percentage) experienced an acceleration region of a variety of sizes that have been put into 10 $R_\odot$ bins. It can be immediately seen from these plots that the acceleration region around the Sun is not a fixed size, but can vary.

From the previous analysis, the 2nd order polynomial appeared to give the poorest fit. This would appear to be echoed in the top panel of Fig. 6.4, where most of the events experienced acceleration beyond $40R_\odot$. This was not initially expected, as most of the acceleration should occur close to the Sun and it is not consistent with the findings of Sheeley *et al.* (1997). It is also not consistent with the middle or bottom panels of the same figure. Consider also that it was the least successful of the fits when analysied with a chi-squared test, it appears that a second order polynomial does not adequately describe the acceleration experienced by CIR-related solar wind transients close to the Sun. With this in mind, a 3rd order polynomial would appear to be easier to incorporate into modelling of time-elongation profiles seen in J-maps as it would be possible to reliably reproduce many of the fits by assuming an acceleration region at a fixed distance between 20 and 30 $R_\odot$ from the Sun, as opposed to having a greater range of possible acceleration region sizes.

Considering the middle panel of Fig. 6.4, which pertains to the 3rd order polynomial acceleration profiles it can be seen that the range of acceleration region sizes is considerably more limited. There is still variation in its size, but the acceleration region is much closer to the Sun and is broadly consistent with Sheeley *et al.* (1997) (i.e. < 30 $R_\odot$). The final panel, representing the 4th order polynomial fit, shows

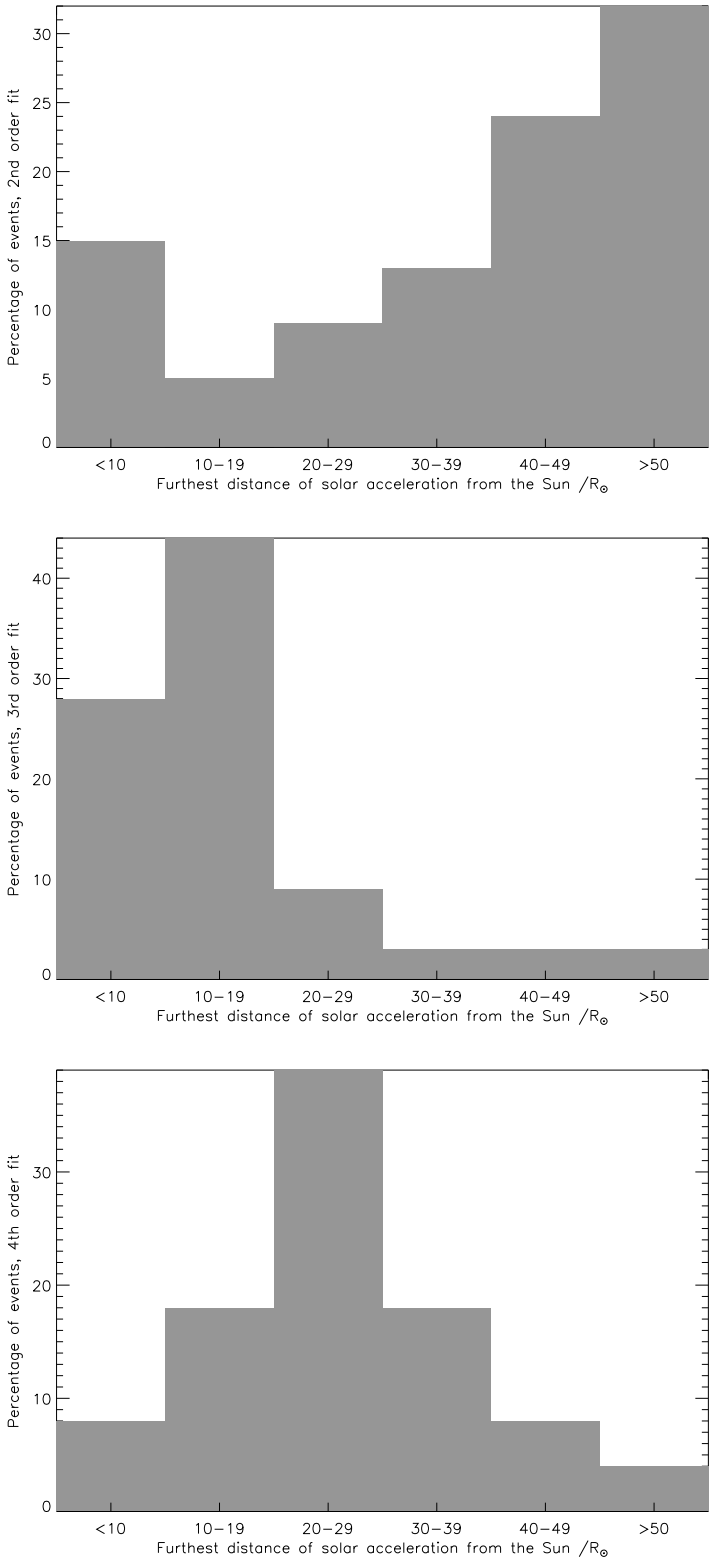

Figure 6.4: This figure shows the size (radius) of the acceleration region surrounding the Sun for each of the CIR-related solar wind transients considered in this study, representing the acceleration with 2nd (top), 3rd (middle) and 4th (bottom) order polynomials. These plots show the percentage of events that experience an acceleration region with a radius that has been put into 10 $R_{\odot}$ bins.

the data relating to the polynomial that, according to the previous analysis, should give the best results. These results also partially agree with Sheeley *et al.* (1997), with the majority of events showing an acceleration region that is within 30 $R_{\odot}$ of the Sun, also showing however a significant number of cases where the acceleration region extends beyond this. Despite the previously noted similarities between the 3rd and 4th order polynomial fits, it is apparent that the two yield very different results when applied to observations. From the analysis conducted here, it would seem that a 4th order polynomial best represents the acceleration of solar wind transients associated with CIRs close to the Sun. In every case investigated, the 4th order fit produced a the highest correlation coefficient, however caution must be used here. All of the different polynomial fits were able to achieve very high (0.99) correlation coefficients with the observed time-distance data. It would also likely be possible to increase the correlation coefficient by simply moving to higher and higher order polynomial fits. These would not necessarily however be physically meaningful. In many instances, multiple order fits all lie within the error bars of the data points, so it can be difficult to distinguish between the different fits, though it should again be noted that the chi-squared test repeatedly indicated that the 4th order polynomial was the most appropriate.

It was seen that when comparing multiple transients from the same CIR, they generally experienced acceleration out to a similar distance from the Sun, though this was not the case for every event investigated. It was also apparent that for multiple transients from the same CIR, third and forth order fits were more likely to reveal that they experienced acceleration out to a similar distance than the second order fit.

6.4 Discussion and Conclusions

I have used a simple polynomial fit to time-distance profiles at low elongation values that are a part of a corotating interaction region in order to estimate the acceleration of CIR-related solar wind transients. I was able to extract acceleration information

about such transients and then use this to modify the fitting of CIRs observed by STEREO HI. It was found that using a polynomial expression to introduce acceleration close to the Sun and then fixing the speed further from the Sun was able to provide a good fit at both high and low elongation values. The acceleration region appears to be at times larger than previously expected. Comparing the fits obtained using different order polynomial fits to represent the acceleration of material close to the Sun, it is apparent that a second order fit is not appropriate, and that a fourth order fit should be used. The inclusion of a variable propagation speed does improve our understanding of the behaviour of CIR-related solar wind transients seen in STEREO HI by confirming that the poor fit a low elongation values is due to acceleration close to the Sun, however the significantly increased complexity of the fitting required to extract the near-Sun acceleration makes this currently of limited use to the practical problem of predicting the arrival of solar wind transients at Earth in real-time. The size of the CIR acceleration region, although variable, seems (using a 4th order polynomial) to be typically around 30 $R_{\odot}$.

Chapter 7

Conclusions and discussion of future direction

This thesis has investigated some of the assumptions typically made when performing fits to solar wind transients as observed by the heliospheric imagers on board the STEREO spacecraft. I have considered the effects of relaxing some of these assumptions when considering both CMEs and CIRs and when using a variety of different fitting techniques. Below I shall briefly summarise the findings of each of the research chapters in this thesis.

In order to extract propagation information about solar wind transients seen in the STEREO HI, a variety of fitting techniques have been developed, with different assumptions regarding the underlying geometry of the problem, each more applicable to a different type of transient. One of the common assumptions made is that the observing spacecraft be stationary with respect to the Sun and Earth when they make their observations. In order to investigate the effects of relaxing this assumption, I simulated data in which the motion of the spacecraft was incorporated and then performed fitting to that data assuming the spacecraft are stationary and then compared the propagation characteristics of the simulated data and that output from the fitting routine used. This was performed for two different geometrical assumptions, one more relevant to transients related to CMEs and the other to

CIRs. It was found that throughout most of parameter space, the difference between the two propagation speeds was small, such that spacecraft motion is probably negligible compared with some of the other errors inherent to the fitting of solar wind transients. In some regions of parameter space (namely for extreme values of *phi*) however, the difference between the two is very considerable indeed, being of the order of 10s–100s km s^{-1}. Each of the different geometries considered were affected in a similar manner and to a similar degree. Analysis was then performed on some real data to demonstrate the effect of relaxing the constant propagation direction assumption. This work was outlined in chapter 4.

The work in chapter 4 was performed assuming single propagating solar wind transients. This is appropriate for CMEs, but CIRs consist of families of such traces. As such, in chapter 5 I attempted to use a technique appropriate to that. I used a fitting technique that fits to the whole observed CIR structure rather than individual transients. I performed fitting on these transients first assuming that spacecraft motion is neglected and subsequently incorporating a correction to account for spacecraft motion. In this way it was possible to investigate how this effect impacted the fitting of CIRs. It was found that estimated propagation speeds increased when spacecraft motion was accounted for, being consistent with the slow solar wind speed. I attempted to predict the arrival times of features associated with these CIRs at three different points in the heliosphere, each at about 1 AU from the Sun, STEREO-A, STEREO-B and ACE. I then compared these arrival times with in-situ data from each of these spacecraft. The predicted arrival times formed a good match with the in-situ measured density and speed enhancements (about 40% of the events arrive within 24 hours of an in-situ signature). Looking in more detail at the in-situ data revealed that there is a great deal of variability when considering density and speed information relating to stream interfaces, being noticeably variable on time scales of a day of two. This potentially indicates that some of the assumption used to perform the fitting are not necessarily valid, however does not change the good match that our predicted arrival times form with the in-situ data. I also performed a superposed epoch analysis, using the predicted arrival times as the zero epoch. This reinforced the idea that CIR related transients appear to propagate at or close to the slow solar wind speed.

In chapter 6, I considered relaxing the assumption that the transients travel at a constant propagation speed. Clearly a transient must accelerate up to its propagation speed. Thus, this is the likely cause of the observed poor fit to elongation profiles close to the Sun. It has been proposed that there is a 'solar acceleration region', in which a transient performs all of its observable acceleration and beyond this, it has a constant speed. I performed polynomial fits to solar wind transients close to the Sun in order to account for the acceleration of these transients. I found that by performing this fit and then incorporating this variable speed into previous fitting of the same transients it was possible to improve the fits close to the Sun, indicating that the poor fitting in this region is indeed due to the variable speed here. The results are consistent with a solar acceleration region close to the Sun, but I found that this region does not extend to fixed distance from the Sun, instead vary in size on a case by case basis, though I was not able to find an underlying cause for this variation. It appears to generally extend out to a maximum of 20–40 $R_{\odot}$. While therefore it seems that I was able to confirm the reason for the poorer fits closer to the Sun, how much use this is for transient fitting remains to be seen. Actually incorporating the acceleration of transients close to the Sun into fitting techniques is not a trivial task, not least because the size of the acceleration region is not a constant. Some success might be possible by simplifying the problem and assuming that the acceleration region is a fixed size, extending out to 30 $R_{\odot}$ and then introducing the acceleration of the transient as another fitted variable. This should lead to an improvement in extracted transient propagation information from J-maps.

The work in this thesis has considered observations made by each of the two STEREO spacecraft individually, it has not used the potential of the mission to make stereoscopic observations of solar wind transients. Using simultaneous observations in this manner could reduce the errors associated with the fitting techniques, but requires data from each spacecraft, which raises the possibility that there are events for which this could not be done due to data gaps or the particular trajectory of a transient.

All of the observations and analysis conducted take observations from the ecliptic

plane. It is not a necessity of these techniques that this be the case, but as much of the interest lies in predicting transient arrival times at Earth, this is where much of the work has been directed. By taking data from different solar radials above and below the Sun-Earth line, it should be possible to perform the same analysis and investigate the propagation of transients out of the ecliptic plane and away from the solar equator. As the correction introduced in chapter 4 applies only to observations made within the ecliptic plane, it is not valid for observations out of this, so a different expression would have to be used. Performing this analysis would be more complex than considering observations in the ecliptic plane.

While conducting this work, it became apparent that the solar rotation period used to track features on the solar surface might not be representative. The Sun undergoes differential rotation, and so its rotation is dependent on latitude. It should be possible to use images of the solar disk to locate features of interest, thereby ascertaining their latitude and hence particular rotation period. This has implications for the prediction of a transients' arrival time, especially as the STEREO spacecraft separate with time.

Overall in this thesis, I have investigated the effects of relaxing various assumptions inherent with many of the techniques generally used to extract propagation information of solar wind transients from STEREO HI data. It was found that when the propagation direction of the observed feature is close to the line of sight, i.e. is directed away from or towards the observer, this can make a significant difference to the estimated propagation characteristics of transients, introducing errors in the estimated propagation speed of potentially hundreds of kilometres per second, though despite the potential for some of these assumptions to have large impacts on derived parameters, estimated arrival times out to 1 AU appear to be fairly robust on average.

References

Acuña, M. H., Curtis, D., Scheifele, J. L., Russell, C. T., Schroeder, P., Szabo, A., and Luhmann, J. G.: The STEREO/IMPACT Magnetic Field Experiment, *Space Sci. Rev.*, **136**, 203–226, 2008.

Andrews, M. D. and Howard, R. A.: A two-type classification of lasco coronal mass ejection, *Spac. Sci. Rev.*, **95**, 147–163, 2001.

Bravo, S., Blanco-Cano, X., and Nikiforova, E.: Different Types of Coronal Mass Ejections at Minimum and Maximum of Solar Activity and their Relation to Magnetic Field Evolution, *Sol. Phys.*, **180**, 461–471, 1998.

Brueckner, G. E., Howard, R. A., Koomen, M. J., Korendyke, C. M., Michels, D. J., Moses, J. D., Socker, D. G., and Linker, J.: The Large Angle Spectroscopic Coronagraph (LASCO), *Sol. Phys.*, **162**, 357–402, 1995.

Chapman, S.: Corpuscular Influences and Atmospheric Electricity, *J. Geophys. Res.*, **55**, 361–372, 1950.

Chen, F. F.: Introduction to Plasma Physics and Controlled Fusion, Volume 1: Plasma Physics, Springer, second edn., 2006.

Chiu, M. C., Von-Mahlem, U. I., Willey, C. E., Betenbaugh, T. M., Maynard, J. J., Krien, J. A., Conde, R. F., Gray, W. T., Hunt Jr., J. W., Mosher, J. E., McCullough, M. G., Panneton, P. E., Staiger, J. P., and Rodberg, E. H.: ACE Spacecraft, *Space Science Reviews*, **86**, 257–284, 1998.

Conlon, T. M., Milan, S. E., Williams, A. O., and Davies, J. A.: Assessing the Effect if Spacecraft Motion on Single-Spacecraft Solar Wind Tracking Techniques, *Sol. Phys.*, **289**, 3935–3947, 2014.

Cremades, H. and Bothmer, V.: On the three-dimensional configuration of coronal mass ejections, *Astronomy and Astrophys.*, **422**, 307–322, 2004.

Davies, J. A., Harrison, R. A., Rouillard, A. P., Sheeley, N. R., Perry, C. H., Bewsher, D., Davis, C. J., Eyles, C. J., Crothers, S. R., and Brown, D. S.: A Synoptic View of Solar Transient Evolution in the Inner Heliosphere Using the Heliospheric Imagers on STEREO, *Geophys. Res. Lett.*, **36**, 2009.

Davies, J. A., Harrison, R. A., Perry, C. H., Möstl, C., Lugaz, N., Rollett, T., and al., E.: A self-similar expansion model for use in solar wind transient propagation studies, *Astrophys. J.*, **750**, 2012.

Davies, J. A., Perry, C. H., Trines, R. M. G. M., Harrison, R. A., Lugaz, N., Möstl, C., Liu, Y. D., and Steed, K.: Establishing a stereoscopic technique for determining the kinematic properties of solar wind transients based on a generalized self-similarly expanding circular geometry, *Astrophys. J.*, **777**, 167, 2013.

Davis, C. J., Davies, J. a., Owens, M. J., and Lockwood, M.: Predicting the arrival of high-speed solar wind streams at Earth using the STEREO Heliospheric Imagers, *Space Weather*, **10**, 2012.

Driesman, A., Hynes, S., and Cancro, G.: The STEREO Observatory, *Space Science Reviews*, **136**, 17–44, 2007.

Eyles, C. J., Harrison, R. A., Davis, C. J., Waltham, N. R., Shaughnessy, B. M., Mapson-Menard, H. C. A., Bewsher, D., Crothers, S. R., Davies, J. A., Simnett, G. M., Howard, R. A., Moses, J. D., Newmark, J. S., Socker, D. G., Halain, J.-P., Defise, J.-M., Mazy, E., and Rochus, P.: The Heliospheric Imagers Onboard the STEREO Mission, *Sol. Phys.*, **254**, 387–445, 2008.

Forbes, T. G.: A review on the genesis of coronal mass ejections, *J. Geophys. Res.*, **105**, 23 153–23 165, 2000.

Galvin, A. B., Kistler, L. M., Popecki, M. A., Farrugia, C. J., Simunac, K. D. C., Ellis, L., Möbius, E., Lee, M. a., Boehm, M., Carroll, J., Crawshaw, A., Conti, M., Demaine, P., Ellis, S., Gaidos, J. A., Googins, J., Granoff, M., Gustafson, A., Heirtzler, D., King, B., Knauss, U., Levasseur, J., Longworth, S., Singer,

K., Turco, S., Vachon, P., Vosbury, M., Widholm, M., Blush, L. M., Karrer, R., Bochsler, P., Daoudi, H., Etter, A., Fischer, J., Jost, J., Opitz, A., Sigrist, M., Wurz, P., Klecker, B., Ertl, M., Seidenschwang, E., Wimmer-Schweingruber, R. F., Koeten, M., Thompson, B., and Steinfeld, D.: The Plasma and Suprathermal Ion Composition (PLASTIC) Investigation on the STEREO Observatories, *Space Sci. Rev.*, **136**, 437–486, 2008.

Gopalswamy, N., Davila, J. M., St. Cyr, O. C., Sittler, E. C., Aucheère, F., Duvall Jr., T. L., Hoeksema, J. T., Maksimovic, M., MacDowall, R. J., Szabo, A., and R., C. M.: .

Gosling, J. T.: Coronal Mass Ejections: An Overview, in Coronal Mass Ejections, edited by N. Crooker, A. Joselyn, and J. Feynman, AGU, Washington, 1997.

Gosling, J. T. and Pizzo, V. J.: Formation and Evolution of Corotating Interaction Regions and their Three Dimensional Structure, *Space Sci. Rev.*, **89**, 21–52, 1999.

Gosling, J. T., Asbridge, J. R., Bame, S. J., and Feldman, W. C.: Solar wind stream interfaces, *J. Geophys. Res.*, **83**, 1401–1412, 1978.

Greaves, W. M. H. and Newton, H. W.: Large geomagnetic storms and large sunspots, *Monthly Notices Roy. Astron. Soc.*, **88**, 556–567, 1928.

Harrison, R. A., Davies, J. A., Möstl, C., Liu, Y., Temmer, M., Bisi, M. M., Eastwood, J. P., de Koning, C. A., Nitta, N., Rollett, T., Farrugia, C. J., Forsyth, R. J., Jackson, B. V., Jensen, E. A., Kilpua, E. K. J., Odstrcil, D., and Webb, D. F.: An Analysis of the Origin and Propagation of the Multiple Coronal Mass Ejections of 2010 August 1, *Astrophys. J.*, **750**, 45, 2012.

Howard, R. A., Brueckner, G. E., Cyr, O. C. S., Biesecker, D. A., Dere, K. P., Koomen, M. J., Korendyke, C. M., Lamy, P. L., Llebaria, A., Bout, M. V., Michels, D. J., Moses, J. D., Paswaters, S. E., Plunkett, S. P., Schwenn, R., Simnett, G. M., Socker, D. G., Tappin, S. J., and Wang, D.: Observations of CMEs from SOHO/LASCO, *Geophys. Monograph Series*, **99**, 17–26, 1997.

Howard, T. A. and DeForest, C. E.: The Thomson Surface. I. Reality and Myth, *Astrophys. J.*, **752**, 130–143, 2012.

Howard, T. A. and Tappin, S. J.: Interplanetary Coronal Mass Ejections Observed in the Heliosphere: 1. Review of Theory, *Space Sci. Rev.*, **147**, 31–54, 2009.

Howard, T. A., Webb, D. F., Tappin, S. J., Mizuno, D. R., and Johnston, J. C.: Tracking Halo Coronal Mass Ejections from 01 AU and Dpace Weather Forecasting using the Solar Mass Ejection Imager (SMEI), *J. Geophys. Res.*, **111**, A04 105, 2006.

Hundhausen, A. J.: Physics and Chemistry in Space Volume 5: Coronal Expansion and Solar Wind, Springer, New York, 1972.

Hundhausen, A. J.: Sizes and Locations of Coronal Mass Ejections, *J. Geophys. Res.*, **98**, 177–200, 1993.

Hundhausen, A. J.: The Solar Wind, in Introduction to Space Physics, edited by M. G. Kivelson and C. T. Russell, chap. 4, Cambridge University Press, 1995.

Joshi, A. D. and Srivastava, N.: Acceleration of Coronal Mass Ejections From Three-Dimensional Reconstruction of Stereo Images, *Astrophys. J.*, **739**, 8, 2011.

Kahler, S. W. and Webb, D. F.: V Arc Interplanetary Coronal Mass Ejections Observed with the Solar Mass Ejection Imager, *J. Geophys. Res.*, **112**, 2007.

Kaiser, M. L., Kucera, T. A., Davila, J. M., Cyr, O. C., Guhathakurta, M., and Christian, E.: The STEREO Mission: An Introduction, *Space Sci. Rev.*, **136**, 5–16, 2007.

Koomen, M. J., Detwiler, C. R., Brueckner, G. E., Cooper, H. W., and Tousey, R.: White Light Coronagraph in OSO-7., *Applied Optics*, **14**, 743–51, 1975.

Koutchmy, S. and Lamy, P.: Properties and Interactions of the Interplanetary Dust, in IAU Colloq., vol. 85, 1985.

Lang, K. R.: The Cambridge Encyclopedia of the Sun, CUP, 2001.

Lee, M. A.: An analytical theory of the morphology, flows, and shock compressions at corotating interaction regions in the solar wind, *J. Geophys. Res.*, **105**, 10 491–10 500, 2000.

Leske, R. A., Mewaldt, R. A., Mason, G. M., Cohen, C. M. S., Cummings, A. C., Davis, A. J., Labrador, A. W., Miyasaka, H., Stone, E. C., and Wiedenbeck, M. E.: Particle acceleration and transport in the heliosphere and beyond: 7th internation astrophysics conf., *AIP Conf. Proc.*, 2008.

Lin, J., Forbes, T. G., Isenberg, P. A., and Demoulin, P.: The effect of curvature on flux-rope models of coronal mass ejections, *Astrophys. J.*, **504**, 1006–1019, 1998.

Liu, Y., Davies, J. A., Luhmann, J. G., Vourlidas, A., Bale, S. D., and Lin, R. P.: Geometric Triangulation of Imaging Observations To Track Coronal Mass Ejections Continuously Out To 1 Au, *Astrophys. J. Lett.*, **710**, L82–L87, 2010.

Liu, Y. D., Luhmann, J. G., Lugaz, N., Möstl, C., Davies, J. A., Bale, S. D., and Lin, R. P.: On Sun-to-Earth Propagation of Coronal Mass Ejections, *Astrophys. J.*, **769**, 2013.

Low, B. C.: Coronal mass ejections, flares and prominences, in Solar Wind Nine, edited by S. R. Habbal, pp. 109–114, AIP, New York, 1999.

Low, B. C. and Smith, D. F.: The free energies of partially open coronal magnetic fields, *Astrophys. J.*, **410**, 412–425, 1993.

Lugaz, N.: Accuracy and Limitations of Fitting and Stereoscopic Methods to Determine the Direction of Coronal Mass Ejections from Heliospheric Imagers Observations, *Sol. Phys.*, **267**, 411–429, 2010.

Lugaz, N. and Kintner, P.: Effect of Solar Wind Drag on the Determination of the Properties of Coronal Mass Ejections from Heliospheric Images, *Sol. Phys.*, **285**, 281–294, 2013.

Lugaz, N., Vourlidas, A., and Roussev, I. I.: Deriving the Radial Distances of Wide Coronal Mass Ejections from Elongation Measurements in the Heliosphere Application to CME-CME Interaction, *Ann. Geophys.*, **27**, 3479–3488, 2009.

Mason, G. M., Desai, M. I., Mall, U., Korth, A., Bucik, R., Rosenvinge, T. T., and Simunac, K. D.: In Situ Observations of CIRs on STEREO, Wind, and ACE During 2007 2008, *Sol. Phys.*, **256**, 393–408, 2009.

Mikic, Z. and Linker, J. A.: Disruption of coronal magnetic field arcades, *Astrophys. J.*, **430**, 898–912, 1994.

Milan, S. E.: Space Plasmas, 2011.

Möstl, C., Rollett, T., Lugaz, N., Farrugia, C. J., Davies, J. A., Temmer, M., Veronig, A. M., Harrison, R. A., Crothers, S., Luhmann, J. G., Galvin, A. B., Zhang, T. L., Baumjohann, W., and Biernat, H. K.: Arrival Time Calculation for Interplanetary Coronal Mass Ejections with Circular Fronts and Application To STEREO Observations of the 2009 February 13 Eruption, *Astrophys. J.*, **741**, 2011.

Neugebauer, M. and Goldstein, R.: Particle and Field Signatures of Coronal Mass Ejections in the Solar Wind, in Coronal Mass Ejections, edited by N. Crooker, J. A. Joselyn, and J. Feynman, pp. 245–251, AGU, Washington, 1997.

Parker, E. N.: Dynamics of the Interplanetary Gas and Magnetic Fields, *Astrophys. J.*, **128**, 664–676, 1958.

Parker, E. N.: Interplanetary Dynamical Processes, Interscience Publishers, New York, illustrate edn., 1963.

Priest, E. R.: The Sun and its Magnetohydronamics, in Introduction to Space Physics, edited by M. G. Kivelson and C. T. Russell, chap. 3, pp. 58–89, Cambridge University Press, 1995.

Richardson, I. G.: The Formation of CIRs at Stream-Stream Interfaces and Resultant Geomagnetic Activity, *Geophys. Monograph Series*, **167**, 45–58, 2006.

Rouillard, A. P., Davies, J. A., Forsyth, R. J., Rees, A., Davis, C. J., Harrison, R. A., Lockwood, M., Bewsher, D., Crothers, S. R., Eyles, C. J., Hapgood, M., and Perry, C. H.: First Imaging of Corotating Interaction Regions Using the STEREO Spacecraft, *Geophys. Res. Lett.*, **35**, 2008.

Rouillard, A. P., Davies, J. A., Lavraud, B., Forsyth, R. J., Savani, N. P., Bewsher, D., Brown, D. S., Sheeley, N. R., Davis, C. J., Harrison, R. A., Howard, R. A., Vourlidas, A., Lockwood, M., Crothers, S. R., and Eyles, C. J.: Intermittent

Release of Transients in the Slow Solar Wind: 1. Remote Sensing Observations, *J. Geophys. Res.*, **115**, 2010.

Russell, C. T.: A brief history of solar-terrestrial physics, in Introduction to Space Physics, chap. 1, 1995.

Sanderson, T. R., Lin, R. P., Larson, D. E., Mccarthy, M. P., Parks, G. K., Lormant, N., Lepping, K. O. R. P., Steinberg, J. T., and Hoeksema, J. T.: Wind observations of the influence of the Sun's magnetic field on the interplanetary medium at 1 AU, *J. Geophys. Res.*, **103**, 17 235–17 247, 1998.

Savani, N. P., Rouillard, a. P., Davies, J. a., Owens, M. J., Forsyth, R. J., Davis, C. J., and Harrison, R. a.: The radial width of a Coronal Mass Ejection between 0.1 and 0.4 AU estimated from the Heliospheric Imager on STEREO, *Ann. Geophys.*, **27**, 4349–4358, 2009.

Sheeley, N. R. and Rouillard, A. P.: Tracking Streamer Blobs Into the Heliosphere, *Astrophys. J.*, **715**, 300–309, 2010.

Sheeley, N. R., Wang, Y. M., Hawley, S. H., Brueckner, G. E., Dere, K. P., Howard, R. A., Koomen, M. J., Korendyke, C. M., Michels, D. J., Paswaters, S. E., Socker, D. G., Lamy, P. L., and Llebaria, A.: Measurements of flow speeds in the corona between 2 and 30 R, *Astrophys. J.*, **484**, 472–478, 1997.

Sheeley, N. R., Walters, J. H., Wang, Y. M., and Howard, R. A.: Continuous Tracking of Coronal Outflows: Two Kinds of Coronal Mass Ejections, *J. Geophys. Res.*, **104**, 24 739–24 768, 1999.

Sheeley, N. R., Herbst, A. D., Palatchi, C. A., Wang, Y., Howard, R. A., Moses, J. D., Vourlidas, A., Newmark, J. S., Socker, D. G., Plunkett, S. P., Korendyke, C. M., Burlaga, L. F., Davila, J. M., Thompson, W. T., St Cyr, O. C., Harrison, R. A., Davis, C. J., Eyles, C. J., Halain, J. P., Wang, D., Rich, N. B., Battams, K., Esfandiari, E., and Stenborg, G.: Heliospheric Images of the Solar Wind at Earth, *Astrophys. J.*, **675**, 853–862, 2008.

Socker, D. G., Howard, R. A., Korendyke, C. M., Simnett, G. M., and Webb, D. F.:

NASA Solar Terrestrial Relations Observatory (STEREO) Mission Heliospheric Imager, *SPIE*, **4139**, 2000.

Srivastava, N., Schwenn, R., Inhester, B., Stenborg, G., and Podlipnik, B.: Acceleration Profile of the Slow Solar Wind as Inferred from Gradual Mass Ejections Observed by LASCO, *Space Sci. Rev.*, **87**, 303–306, 1999a.

Srivastava, N., Schwenn, R., Inhester, B., Stenborg, G., and Podlipnik, B.: Measurements of flow speeds and acceleration in gradually evolving solar mass ejections as observed by LASCO, in AIP, vol. 115, pp. 115–118, AIP, 1999b.

Stone, E. C., Frandsen, A. M., and Mewaldt, R. A.: The Advanced Composition Explorer, *Space Sci. Rev.*, **86**, 1–22, 1998.

Temmer, M., Rollett, T., Möstl, C., Veronig, A. M., Vršnak, B., and Odstrčil, D.: Influence of the Ambient Solar Wind Flow on the Propagation Behavior of Interplanetary Coronal Mass Ejections, *Astrophys. J.*, **743**, 2011.

Tsurutani, B. T., Gonzalez, W. D., Gonzalez, A. L. C., Guarnieri, F. L., Gopalswamy, N., Grande, M., Kamide, Y., Kasahara, Y., Lu, G., Mann, I., McPherron, R., Soraas, F., and Vasyliunas, V.: Corotating solar wind streams and recurrent geomagnetic activity: A review, *J. Geophys. Res.*, **111**, 2006a.

Tsurutani, B. T., Mcpherron, R. L., Gonzalez, W. D., Lu, G., Gopalswamy, N., and Guarnieri, F. L.: Magnetic Storms Caused by Corotating Solar Wind Streams, *Geophys. Monograph Series*, **167**, 1–17, 2006b.

Vourlidas, A. and Howard, R. A.: The Proper Treatment of Coronal Mass Ejection Brightness : A New Methodology and Implications for Observations, *Astrophys. J.*, **642**, 1216–1221, 2006.

Williams, A. O., Davies, J. A., Milan, S. E., Rouillard, A. P., Davis, C. J., Perry, C. H., and Harrison, R. A.: Deriving Solar Transient Characteristics from Single Spacecraft STEREO/HI Elongation Variations: a Theoretical Assessment of the Technique, *Annales Geophysicae*, **27**, 4359–4368, 2009.

Williams, A. O., Edberg, N. J. T., Milan, S. E., Lester, M., Fränz, M., and Davies, J. A.: Tracking corotating interaction regions from the Sun through to the orbit of Mars using ACE, MEX, VEX, and STEREO, *J. Geophys. Res.*, **116**, 2011.

Wolfson, R.: Energy requirements for opening the solar corona, *Astrophys. J.*, **419**, 382–387, 1993.

Wolfson, R. and Dlamini, B.: Cross-field currents: An energy source for coronal mass ejections?, *Astrophys. J.*, **483**, 961–971, 1997.

Wolfson, R. and Saran, S.: Energetics of coronal mass ejections: Role of the streamer cavity, *Astrophys. J.*, **499**, 496–503, 1998.

Wood, B. E., Howard, R. A., and Socker, D. G.: Reconstructing the Morphology of an Evolving Coronal Mass Ejection, *Astrophys. J.*, **715**, 1524–1532, 2010.